Toroidal Flow Velocity Measurement in the STOR-M Tokamak by Ion Doppler Spectroscopy

A Thesis Submitted to the College of
Graduate Studies and Research
in Partial Fulfillment of the Requirements
for the Degree of Master of Science
in the Department of Physics and Engineering Physics
University of Saskatchewan
Saskatoon

By
Yelu Liu

Permission to Use

In presenting this thesis in partial fulfillment of the requirements for a Postgraduate degree from the University of Saskatchewan, I agree that the Libraries of this University may make it freely available for inspection. I further agree that permission for copying of this thesis in any manner, in whole or in part, for scholarly purposes may be granted by the professor or professors who supervised my thesis work or, in their absence, by the Head of the Department or the Dean of the College in which my thesis work was done. It is understood that any copying or publication or use of this thesis or parts thereof for financial gain shall not be allowed without my written permission. It is also understood that due recognition shall be given to me and to the University of Saskatchewan in any scholarly use which may be made of any material in my thesis.

Requests for permission to copy or to make other use of material in this thesis in whole or part should be addressed to:

Head of the Department of Physics and Engineering Physics
University of Saskatchewan
116 Science Place
Saskatoon, Saskatchewan
Canada S7N 5E2

Abstract

An Ion Doppler Spectrometer (IDS) was built for the purpose of toroidal ion flow velocity measurement in the STOR-M tokamak. Emission lines from carbon and oxygen ions $\mathrm{C_{III}}$, $\mathrm{O_V}$ and $\mathrm{C_{VI}}$ were used for spectral profiles measurement. Based on the Doppler effect, the ion flow velocities were calculated from the spectral line shift.

The IDS system was built based on a Czery-Turner spectrometer. A cylindrical rod lens was used to magnify the grating dispersion. The spectrum was recorded by a photomultiplier tube (PMT) detector, whose output current was converted to voltage through a current preamplifier.

The IDS achieved a time resolution of 0.1 ms defined by the RC time, and the ion flow velocity resolution is $\pm 1 \sim 2\ \mathrm{km \cdot s^{-1}}$. Profile measurement shows the impurity emission lines at different ionization stage populated at different radial positions in the chamber. The flow velocities were measured with various operation modes. A flow velocity shear was discovered for different ion species. The ions in the edge region are flowing in the same direction as plasma current, while the ions in the plasma center are flowing in the anti-current direction. The impurity flow directions are inversed with inversed plasma current configuration. It was found that the impurity flow velocities can be changed by compact torus (CT) injection, resonant magnetic perturbation (RMP) field, as well as rapid hydrogen puffing.

Acknowledgments

I would like to thank Prof. Akira Hirose for serving as supervisor and chief motivator during this project. His demand for excellence has fostered in me a drive and motivation. It has truly been a privilege to work with Prof. Hirose. Prof. Chijin Xiao is owed a debt of gratitude for his guidance, and feel I have gained tremendously from his wisdom and experience. I would like to thank Dr. Takumi Onchi who has been an excellent colleague and a good friend, as well as Dr. Dazhi Liu and Dr. Mykola Dreval for assistance on machine operation and instrumentation. Thank my fellow graduate students Yue Ding, Kyaw Minn Hthu, Michael Hubeny, Sayf Elgriw, and Kurt Krueger for sharing the time and friendship. The technical support from Mr. Dave McColl and the Physics Machine Shop are important for my thesis work. At last, I would like to thank the Natural Sciences and Engineering Research Council (NSERC), the University of Saskatchewan, and the Canada Research Chair (CRC) program for providing the financial support to this research project, as well as the encouragement and support from my parents.

This work is dedicated to my parents.

Table of Contents

Permission to Use i

Abstract ii

Acknowledgments iii

Dedication iv

Table of Contents v

List of Tables viii

List of Figures ix

List of Abbreviations and Symbols xiv

1 Introduction 1

1.1 Introduction to tokamak research 1

1.2 Motivation of ion flow velocity measurement using ion Doppler spectroscopy . . . 4

1.3 Recent development of IDS systems 5

1.4 Thesis goals and objectives 6

1.5 Thesis outline 7

2 The STOR-M tokamak 8

2.1 Toroidal vessel and magnetic coils 8

2.2 Major diagnostics of the STOR-M tokamak 13
2.2.1 Rogowski coils 13
2.2.2 Loop voltage 14
2.2.3 Position sensing coils 14
2.2.4 Microwave interferometer 15
2.2.5 Optical spectrometers 16
2.3 Previous plasma flow velocity measurements in the STOR-M tokamak. 17

3 Ion flow velocity measurement theories 21
3.1 Impurities Emission 21
3.2 Plasma flow mechanism 23
3.3 Doppler shift and broadening 25
3.4 Spectral line broadening 28
3.4.1 Line broadening effects 28
3.4.2 Superposition of broadening effects 29
3.4.3 The estimated Doppler broadening 30

4 Ion Doppler spectrometer structure and calibration 32
4.1 Introduction 32
4.2 The Czyner-Turner spectrometer 32
4.3 The entrance optics 36
4.4 The exit optics 37
4.5 System alignment 43
4.6 System calibration 43
4.7 Data analysis methodology 44
4.8 Error analysis 47

5 Pre-measurement processes 49
5.1 Introduction 49

5.2 Emission line identification 49
5.2.1 Previous spectroscopic measurement in the STOR-M and other fusion devices 50
5.2.2 Impurity gas injection system and identified emission lines 51
5.3 Radial profile measurement 55
5.4 Definition of plasma flow direction 57

6 Toroidal flow measurement in various operation modes 60
6.1 Normal Ohmic discharges 60
6.2 Reversed current operation 62
6.3 Compact torus injection experiment 64
6.4 Resonant magnetic perturbation experiment 67
6.5 Ohmic H-mode like transition experiment 72

7 Conclusions and future work 75
7.1 Conclusions 75
7.2 Future work 76
7.2.1 Ion temperature measurement 76
7.2.2 Simultaneous measurement of the normal and tangential ports in the tokamak. 76
7.2.3 Relationship between the impurity ion flow velocity and bulk plasma flow velocity 76

Bibliography 78

Appendix A - Optical components 83

Appendix B - Linear dispersion measurement. 86

Appendix C - Nonlinear Gaussian fitting code 87

List of Tables

2.1 Primary parameters of the STOR-M tokamak [18]. 10

3.1 Estimated broadening of various emission lines from a ion temperature range from 10 to 100 eV. 30

5.1 Incomplete list of emission lines used in fusion devices. 50

5.2 Major emission lines observed in the STOR-M tokamak. 54

List of Figures

1.1 A typical magnetic coil system of Tokamak. Transformer coils induce toroidal electric field and plasma current, as well as poloidal magnetic filed, which in combination with the toroidal magnetic filed forms helical magnetic field in the tokamak plasma. 2

1.2 Schematic diagram of a fusion power plant. The heat produced in the D-T reaction can sustain plasma's high temperature, as well as transfer lithium into tritium. The output heat can drive steam generators for electricity generation [3]. 3

1.3 The IDS system used in the Helicity Injected Torus. The spectrum is magnified by a cylindrical lens and recorded by a 16-channel PMT [14]. 6

2.1 Top view of the STOR-M tokamak. The limiter is shown at the upper right conner. The position of some diagnostics has been changed from this figure. 9

2.2 Side view of the STOR-M tokamak. OH, VE, and FB represent Ohmic heating, vertical equilibrium, and feedback coils, respectively. 10

2.3 Simple toroidal field (no equilibrium). Charge separation and electric filed in a toroidal geometry with only toroidal magnetic filed. 11

2.4 Helical magnetic field combines the toroidal and poloidal magnetic fields. Electric charges are not separated in this configuration. 11

2.5 Capacitor bank circuit for Ohmic Heating and Vertical Equilibrium coils. 12

2.6 Circular Rogowski coil and its rectangular cross section. 13

2.7 Loop Voltage pick-up loop circuit and its voltage dividing circuit [20]. 14

2.8 Plasma position detection coils. The $\mathrm{B}_{\theta *}$ coils measure the poloidal magnetic field, and the $\mathrm{B}_{\mathrm{r}*}$ coils measure the radial magnetic field. 15
2.9 Compensation Circuit with Rogowski coil to measure the unwanted magnetic field. 15
2.10 Schematic diagram of 4mm microwave interferometer for electron density measurement in STOR-M. The microwave is divided into one plasma path and two reference paths. 16
2.11 The Heath EU-700 spectrometer is a Czerny-Turner type. It has a focal length of 0.35m. 17
2.12 Schematic diagram of Ocean Opics USB2000 spectrometer. It is able to measure a full spectrum from 2000 Å to 9600 Å. 18
2.13 Schematic diagram of the SPEX 1702 spectrometer. It has longer focal length and better resolution than other two spectrometers. 18
2.14 Structure of the four-sided Mach probe. Each pairs of the probe collectors measure corresponding flow velocities. 19
2.15 Toroidal flow velocity measured by the four-sided Mach probe. One unit Mach number corresponds to 30 km/s. 19
2.16 The arrangement of the eight collectors of the G-probe. 20
2.17 Parallel and perpendicular flow velocities measured by the G-probe during normal Ohmic heating discharges. 20

3.1 The carbon equilibrium ionization state distribution [29]. The Arabic numbers on top of the curves indicate the ionization stages, starting from number "1" for neutral atoms. 22
3.2 The oxygen equilibrium ionization state distribution [29]. The Arabic numbers on top of the curves indicate the ionization stages, starting from number "1" for neutral atoms. 22
3.3 Charge exchange induced by neutral beam injection. The observed line emission is the combination of active and passive CX reactions [32]. 23

3.4 Two velocity decompose coordinates 24

4.1 The schematic diagram of the IDS system. The light collected from the tokamak ports is conveyed by a optical fiber to the spectrometer input slit. It is collimated by a concave mirror, diffracted by a refraction grating, and focused by another concave mirror to the exit of the spectrometer. A cylindrical rod lens magnifies the spectrum to the PMT surface. 34

4.2 The refraction grating. It has N grooves and the distance between neighboring groove is d. 35

4.3 The side view of the light collection optics. Parallel light from the STOR-M tokamak is focused to the fiber optics and further focused on the entrance slit of the spectrometer. 37

4.4 Picture and dimension parameters of the multi-anode PMT used in the IDS system (Unit: mm) [35]. 40

4.5 The I-V preamplifier consists of an operational amplifier, a pick-up resistor, as well as a coupling capacitor and impedance matching resistors. 41

4.6 Picture of the output optics of the IDS system. The optical components are enclosed in a carefully sealed light-tight aluminum box. A door is made to the left wall for alignment and calibration. The legs of the bench is mechanically isolated by compact air mounts. (One is visible at the left bottom corner.) 42

4.7 Waveform of calibration. Relative sensitivity, dispersion, instrumental width, and DC offset can be found in the waveform. 44

4.8 The instrumental broadening as a function of the input slit width. 45

4.9 The flowchart of the Gaussian fitting algorithm. 46

4.10 Gaussian fitting for $\mathrm{C_{III}}$ during an Ohmic heating discharge. 47

4.11 The $\mathrm{C_{III}}$ velocity measured from two ports. 48

4.12 The β angle for velocity amendment. 48

5.1 The schematic diagram of gas puffing. The V1 to V5 are gas valves, and C1 and C2 are connectors. The parts enclosed in the dashed box is movable. 52
5.2 The spectrum measured from the fiber optical spectrometer (Ocean Optics Spec2000). 53
5.3 The emission lines intensity of C_{III}, O_V and C_{VI} ions during Ohmic heating discharges. 55
5.4 The schematic diagram of radial profile measurement in STOR-M tokamak 56
5.5 Inversion method 57
5.6 Line integrated signals of C_{III}, O_V and C_{VI} emission lines. 58
5.7 Profile of C_{III}, O_V and C_{VI} emission lines. 58
5.8 The directions of the STOR-M tokamak. The plasma current I_p is in the counter-clockwise direction, and the toroidal magnetic field B_T is in the clockwise direction. For the IDS system, the larger channel number records the longer wavelength. 59

6.1 Plasma Parameters (Plasma Current, Loop Voltage, Plasma Position, and H_α emission) of a typical shot $\#244672$. 61
6.2 Ohmic heating discharge flow results. Positive value on the flow indicates counter-clockwise (co-current) direction, while the negative is clockwise (anti-current) direction. 61
6.3 Plasma Parameters (Plasma Current, Loop Voltage, Plasma Position, and H_α emission) of a typical shot $\#245742$ with reversed current experiment. 63
6.4 Reversed current flow results. Positive value on the flow indicates counter-clockwise direction, while the negative is clockwise direction. 64
6.5 Schematic diagram of USCTI [55]. 65
6.6 Diagram of the STOR-M tokamak and the USCTI injector for tangential CT injection experiments [18]. 65
6.7 Plasma parameters of a typical shot $\#244715$. 66
6.8 Toroidal flow velocity change induced by CT injection. 66

6.9 The coloured arrows indicate the direction of I_{RMP}. The two sets of coils are connected in series and the RMP current is supplied by a capacitor bank discharge [56]. 67
6.10 Waveform of single RMP pulse. 68
6.11 O_V and C_{VI} flow velocities measured during RMP experiment. Two sets of RMP current and two sets of plasma current are used. 69
6.12 Waveform of double RMP pulses. 70
6.13 O_V and C_{VI} flow velocities measured with double RMP current pulses. Two sets of plasma current were also used. 71
6.14 Waveforms of GP control pulse and pressure in the tokamak chamber. 72
6.15 Plasma parameters of a typical shot $\#241271$. 73
6.16 Impurity flow measured during the gas puffing induced transition experiment. . . . 73
6.17 Toroidal flow velocity measured by G-probe during Ohmic H-mode like transition experiment. 74

7.1 The drawing of the lens holder. 83
7.2 The picture of the rotational stage (Newport RSP-2T). 84
7.3 The side view of the optical components of the lens stage combination. 84
7.4 The front view of the optical components of the lens stage combination. 85
7.5 Linear dispersion measurement with various wavelength. 86

List of Abbreviations and Symbols

Abbreviation	Definition
AC	Alternating Current
AWG	American Wire Gauge
BNC	Bayonec Nut Connector
CCD	Charge Coupled Device
CT	Compact Torus
CX	Charge eXchange
DAQ	Data AQuisition system
FB	FeedBack
FWHM	Full Width at Half Maximum
GP	Gas Puffing
HIT	Helicity Injected Torus
IDS	Ion Doppler Spectroscopy/Spectrometer
IFRC	Irvine Field Reversed Configuration
ITER	International Thermonuclear Experimental Reactor
LLNL	Lawrence Livermore National Laboratory
(MA)PMT	(Multi-Anode) PhotoMultiplier Tube
MHD	MagnetoHydroDynamics
NBI	Neutral Beam Injection
NI	National Instruments
NIF	National Ignition Facility
NIST	National Institute of Standards and Technology
OH	Ohmic Heating
PPL	Plasma Physics Laboratory
RFEA	Retarding Field Energy Analysier
RFX	Reversed Field eXperiment

Abbreviation	Definition
RFP	Revised Field Pinch
RMP	Resonant Magnetic Perturbation
RP	Rotary Pump
RWM	Resistive Wall Mode
SOL	Scrap-off-Layer
SSPX	Sustained Spheromak Plasma Experiment
SSX	Swarthmore Spheromak Experiment
STOR-M	Saskatchewan TORous-Modified
S/N	Signal Noise ratio
TCABR	Tokamak Chauffage Alfvén Brésilien
TMP	TurboMolecular Pump
UV	Ultra-Violet
USCTI	University of Saskatchewan Compact Torus Injection
VE	Vertical Equilibrium

Symbol	Definition
a	minor radius
$\boldsymbol{B}$	magnetic field
B_θ	poloidal magnetic field
B_ϕ	toroidal magnetic field
B_v	vertical magnetic field
β	beta factor
β_p	poloidal beta factor
c	speed of light
I_p	plasma current
n_e	electron density
P_{TN}	thermonuclear power
P_H	heating power
q	safety factor
Q	power ratio
R	major radius
T_e	electron temperature
T_i	Ion temperature
τ_E	energy confinement time
ω_p	plasma frequency
$\hat{n}$	peak plasma density
$\hat{T}$	peak plasma temperature
I_p	plasma current
μ_0	magnetic permitivity in vacuum
l_i	self inductance
$\mathbf{v}$	plasma flow velocity
$\mathbf{v_e}$	electron flow velocity
$\mathbf{v_i}$	major ion flow velocity
$\mathbf{v_I}$	impurity ion flow velocity
n_i	ion density
n_I	impurity ion density
j	current density
$\mathbf{E}$	electric field
E_r	radial electric field
p	pressure
v_ϕ	toroidal flow velocity
v_θ	poloidal flow velocity
$\mathbf{v}$	velocity
μ_0	original frequency
μ_D	Doppler frequency
$\Delta\mu$	frequency shift
$\mathbf{u}$	total velocity
$\mathbf{v}$	flow velocity
$\hbar$	Planck constant

Symbol	Definition
h	Planck constant
$\Delta\lambda$	wavelength shift
m_l	magnetic number
μ_B	Bohr magnetron
d	grating space
α	incidence angle
β	diffraction angle
m	diffraction order
λ	wavelength
R_T	resolution power
W	width of grating ruling
N	total number of grating grooves
$f/\#$	f-number
M	magnification ratio
R_1	curvature radius of the left surface
R_2	curvature radius of the right surface
d_l	lens thickness
n	index of refraction
s_1	objective distance
s_2	image distance
s_t	total distance

Chapter 1

Introduction

1.1 Introduction to tokamak research

Fossil fuels such as petroleum, natural gas, and coal constitute a large part of global energy consumption. However, because of the depletion of such fuels and accompanying greenhouse gas emission, alternative energy such as hydro-, solar, wind, and nuclear power is needed. Nuclear power has more stable output than others because it does not rely on the weather and climate condition. Nuclear energy can be generated from two types of reactions: fission and fusion. Fission involves the splitting of heavy nucleus, while in fusion reactions light elements merge together to form heavier ones.

At present, commercial nuclear power plants are all based on fission reactions. The fuels and waste are highly radioactive, and waste treatment and storage are becoming public concern especially after a series of incidents at the Three Mile Island, Chernobyl, and Fukushima. Nuclear fusion is inherently much safer because it does not have highly radioactive fuel and waste, as well as its fuel inventory in the reactor is much smaller. In the universe, nuclear fusion powers millions of stars and the Sun. On the earth, fusion energy has been released in the form of H-bomb for military purposes. However, continuous and controllable fusion reaction is still to be realized.

There are two confinement schemes for nuclear fusion: inertial and magnetic confinement. In the inertial confinement, the fusion fuel is ignited by large input power such as laser beams before diffusing. A typical device of this scheme is the National Ignition Facility (NIF) in the Lawrence Livermore National Laboratory (LLNL), USA [1]. In magnetic confinement, charged particles are

confined by magnetic field. Based on the magnetic configuration, magnetic fusion devices can be categorized into stellarator, tokamak, etc.

"Tokamak" is the acronym for the Russian words of "toroidal chamber with magnetic coils". It achieved better plasma confinement, higher plasma density, and higher plasma temperature than any other magnetic confinement configurations, and tokamak continues to be the focus of nuclear fusion research. The largest tokamak under construction is "ITER", standing for the International Thermonuclear Experimental Reactor, located in Cadarache, France. It is a collaborative project of European Union, United States, Japan, South Korea, China, India, and Russia [2].

The typical structure of a tokamak is shown in the Figure 1.1. The toroidal electric field induces the plasma current. Toroidal and vertical field coils generate magnetic field in the tokamak, which confines the charged particles from running out.

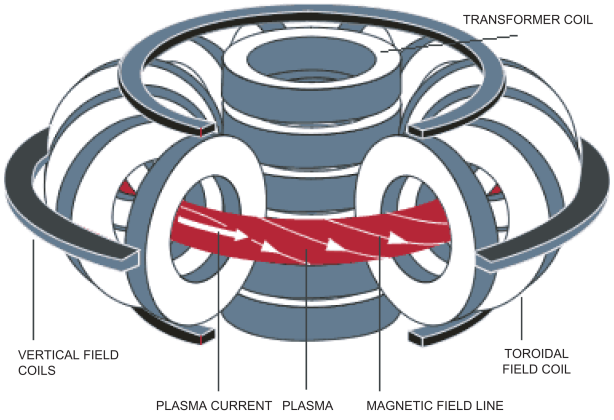

Figure 1.1: A typical magnetic coil system of Tokamak. Transformer coils induce toroidal electric field and plasma current, as well as poloidal magnetic filed, which in combination with the toroidal magnetic filed forms helical magnetic field in the tokamak plasma.

In tokamaks, hydrogen or its isotope gases are heated to high temperature to a state called plasma. The fusion reaction that has the largest cross section is that of D-T (deuterium - tritium) reaction,

$$ {}_1\mathrm{D}^2 + {}_1\mathrm{T}^3 \rightarrow {}_2\mathrm{He}^4\ (3.5\mathrm{MeV}) + {}_0\mathrm{n}^1\ (14.1\mathrm{MeV}) \tag{1.1} $$

Deuterium can be extracted from the seawater, and tritium can be bred in fusion plants from lithium. The α-particle (${}_2\mathrm{He}^4$) transfers its energy back to the plasma to sustain high temperature via collision, and the fast neutrons (${}_0\mathrm{n}^1$) hit the Tokamak wall since they are not subject to the electromagnetic force. The neutrons produce tritium in the lithium blanket. The energy from the heated

wall can be transfered to a steam turbine engine for electricity generation, which is similar to the process in thermal power stations. A schematic diagram of a fusion power plant design is shown in Figure 1.2.

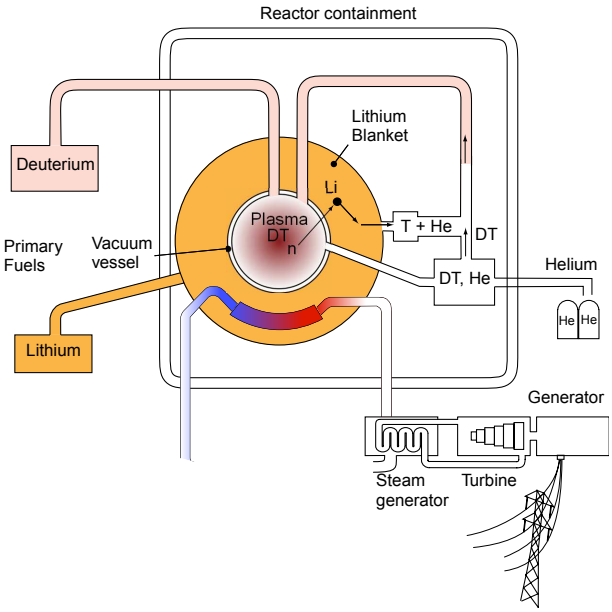

Figure 1.2: Schematic diagram of a fusion power plant. The heat produced in the D-T reaction can sustain plasma's high temperature, as well as transfer lithium into tritium. The output heat can drive steam generators for electricity generation [3].

In tokamak research, there are three important factors: β, safety factor q , and power ratio Q. β is the ratio of the particle pressure over the magnetic field pressure [4].

$$\beta = \frac{\Sigma nkT}{B^2/2\mu_0} = \frac{\text{plasma pressure}}{\text{magnetic pressure}} \tag{1.2}$$

where n is the plasma density, k is the Boltzmann constant, T is the plasma temperature, B is the magnetic field strength, and μ_0 is the permeability of free space. The β factor is limited by plasma stability as $\beta < 1$. The safety factor q is defined as [5]

$$q = \frac{\Delta\phi}{2\pi} \tag{1.3}$$

where $\Delta\phi$ is the toroidal angle the magnetic field line travels when it revolve a full circle in the poloidal plane. For large aspect-ratio ($R \gg a$) tokamaks with circular cross-sections, it is approxi-

mately given by [5]

$$q = \frac{aB_\phi}{R_0 B_\theta} \tag{1.4}$$

where a and R_0 stand for the minor and major radii, and B_ϕ and B_θ are the toroidal and poloidal magnetic field strength. Another important factor is the power ratio Q, which is the ratio between the thermonuclear power P_{TN} and heating power P_H, [5]

$$Q = \frac{P_{TN}}{P_H} \tag{1.5}$$

To have a sustainable fusion reaction, the power ratio Q should be larger than 1. In the JT-60U tokamak, the D-T equivalent Q factor has exceeded 1 [6], while for ITER, the goal is to achieve burning plasma with $Q \geq 10$ [2], in which α particle heating is dominant.

1.2 Motivation of ion flow velocity measurement using ion Doppler spectroscopy

Plasma flow velocity plays important roles in magnetic confinement. For example, during the transition from the low confinement mode to high confinement mode (L-H transition), it is possible that an increase in the flow shear across an unstable region suppresses the instability [5]. The poloidal and toroidal plasma flow is related to radial electric field through force balance equation. The plasma toroidal rotation also plays an important role in controlling resistive wall mode (RWM) [7, 8].

Plasma flow velocity can be measured by various means. Typical diagnostics are Mach probes and Doppler spectroscopy. Mach probes have relatively simpler design and operation, while Ion Doppler spectroscopy (IDS) has two major advantages over Mach probes on plasma flow measurement:

1. IDS is a non-intrusive diagnostic method. The IDS system can be electrically insulated and mechanically isolated from the tokamak. It does not disturb the plasma, neither it will be damaged by the high temperature plasma. Unlike the probes, the IDS system can be adjusted and calibrated at any time without affecting tokamak operation.

2. IDS measures the flow velocity at both the core and edge regions of the tokamak plasma, depending on the specific impurity species, while probes can merely detect the flow velocity at the plasma edge or in the Scrap-off-Layer (SOL) region.

An IDS system is built for the Saskatchewan Torus-Modified (STOR-M). It is the first Doppler spectrometer for ion flow velocity measurement in the Plasma Physics Laboratory (PPL).

1.3 Recent development of IDS systems

Doppler spectroscopy is widely used for measuring velocities of moving light emitting objects based on the Doppler effect, which states the wavelength of light emitted by moving object changes due to motion approaching or receding from the observer [9]. In recent years, this technique was developed for magnetically-confined fusion devices with various optical configuration and components. Some typical IDS systems are reviewed here.

In the Tokamak Chauffage Alfvén Brésilien (TCABR), the toroidal and poloidal ion flow velocities were measured by a single channel photomultiplier tube (PMT), which uses a motorized grating rotating at a constant speed during plasma discharges. The wavelengths shift of $\mathrm{C_{III}}$ and $\mathrm{C_{VI}}$ emission lines are measured refering to xenon calibration lines. Because the wavelength shift is calculated from the time shift of the recorded signals, the flow velocity is not resolved in time [10]. An updated IDS system in this group uses two single channel PMTs. Each PMT measures a section of the spectrum contour. If the wavelength is shifted, the measured signal from PMTs will also change accordingly. Thus the flow velocity can be derived from the ratio between the two PMT signals [11].

Besides signle channel PMTs, compact multi-anode PMTs are also used in IDS systems. They are able to measure time-resolved spectrum line contours. In the Swarthmore Spheromak Experiment (SSX), an echelle grating of 316 grooves/mm operated at the 25th diffraction order providing higher dispersion than regular gratings is used, in combination with a lens system with a magnification of 3.7×, and a 32-channel PMT [12]. Similar configurations are reported in the Irvine Field Reversed Configuration [13], Helicity Injected Torus at the University of Washington [14], and the Sustained Spheromak Plasma Experiment at the Lawrence Livermore National Laboratory [15].

Charge coupled devices (CCD) are used as detectors in IDS systems as well. They have smaller

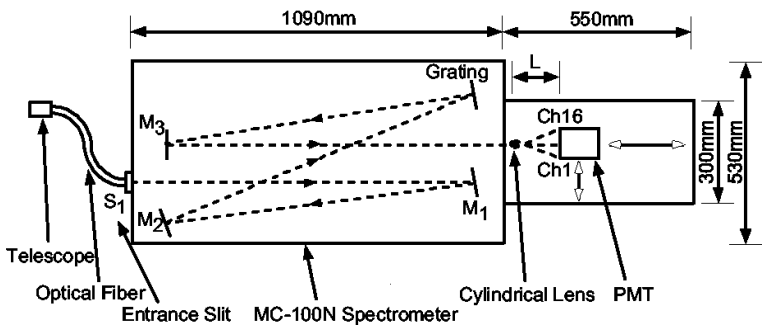

Figure 1.3: The IDS system used in the Helicity Injected Torus. The spectrum is magnified by a cylindrical lens and recorded by a 16-channel PMT [14].

pixel sizes and better resolutions than multi-anode PMTs. Therefore, such systems do not need additional optical component for magnification. But on another hand, CCDs have longer response time, restricting they to only be used on fusion devices with long discharge time. For example, the IDS system equipped with a CCD in RFX-mod reversed field pinch experiment has a time resolution of 2.5 ms [16], which is appropriate for a discharge time of 300ms. Nonetheless, the STOR-M tokamak discharge time is less than 50 ms, and the current flat-top period is only 20 ms. Under this circumstance, a CCD detector can not provide enough time resolution for observing rapid velocity change.

1.4 Thesis goals and objectives

The goal of this thesis is to measure the plasma flow velocities in the STOR-M tokamak. Three major objectives are set to achieve this goal:

1. Design, align, and calibrate the ion Doppler spectrometer. Build periphery components such as the amplifier circuit and impurity gas puffing system.
2. Identify exsiting and useful impurity emission lines from the STOR-M tokamak. Measure the radial profile of those lines.
3. Measure the flow velocities of impurity ions during different operation modes, including Ohmic heating, compact torus injection, resonant magnetic perturbation, and gas puffing experiments.

1.5 Thesis outline

In the first chapter, the concept of nuclear fusion and tokamak was introduced, as well as the motivation of plasma flow velocity measurement. Recent IDS systems for fusion devices were reviewed.

Chapter Two introduces the structure and principle of the STOR-M tokamak, various diagnostic systems, and previous flow measurement results.

The third chapter discusses theories related to IDS measurement, including the mechanism of plasma rotation and Doppler effect.

In Chapter Four, the development of the IDS system is described in detail. Sections 4.2 to 4.4 shows the IDS hardware. The process of system alignment and calibration are described in Sections 4.5 and 4.6. The last two sections describe the data analysis procedures and the error analysis.

Chapter Five shows impurity ion emission lines identified in the STOR-M tokamak, as well as the radial profile measurement of their emissivity. The definition of toroidal flow direction is also determined.

In Chapter Six, the toroidal plasma flow measurement with different operation modes is conducted. They includes Ohmic heating discharges, reversed current experiment, compact torus injection experiment, resonant magnetic perturbation experiment, and Ohmic H-mode like transition experiment.

The last chapter summarizes the research results, and suggests future work including ion temperature measurement, simultaneous measurement of the original and shifted wavelengths, and investigation on the relationship between the impurity ion flow velocities and bulk plasma flow velocities.

Chapter 2

The STOR-M tokamak

STOR-M is a small size tokamak built in 1987 for studies on plasma heating, anomalous transport, and developing novel operation modes and advanced diagnostics. It had its first shot in 1990 and more than 251,000 shots have been logged. Its major achievements include alternating current (AC) operation, as well as Ohmic high confinement mode (H-mode) induced by turbulent heating (TH), electrode biasing, compact torus (CT) injection and resonant magnetic perturbation (RMP). Currently, it is the only device in Canada devoted to magnetic confinement fusion research.

2.1 Toroidal vessel and magnetic coils

The STOR-M tokamak has a toroidal chamber with circular cross section, which resembles the shape of a doughnut. The chamber, with major radius $R = 46\ \mathrm{cm}$ and minor radius $a = 15\ \mathrm{cm}$, is made of 304L type non-magnetic stainless steel and consists of two halves which are electrically insulated by alumina breaks. Inside the chamber, a stainless steel limiter is used to prevent direct contact between the plasma and the chamber wall, which limits the minor radius of plasma to 12 cm vertically and 13 cm horizontally. On the chamber, there are 23 ports (11 vertical, 10 horizontal and 2 tangential, Figure 2.1) available for diagnostics and machine operation. A pumping system consists of a rotary pump (RP) and a $1000\ \mathrm{L/sec}$ turbomolecular pump (TMP) is attached to the vessel to provide a vacuum of $\sim 5 \times 10^{-8}\ \mathrm{Torr}$. During discharges, hydrogen gas is constantly fed to the chamber through a PV-10 piezoelectric valve [17] at a pressure of $\sim 1 \times 10^{-4}\ \mathrm{Torr}$. During each four-minute operation cycle, the capacitor bank is charged in three minutes, and discharged in 50 ms to generate and maintain plasma. There is one minute idle time for capacitor bank cooling

and chamber pumping.

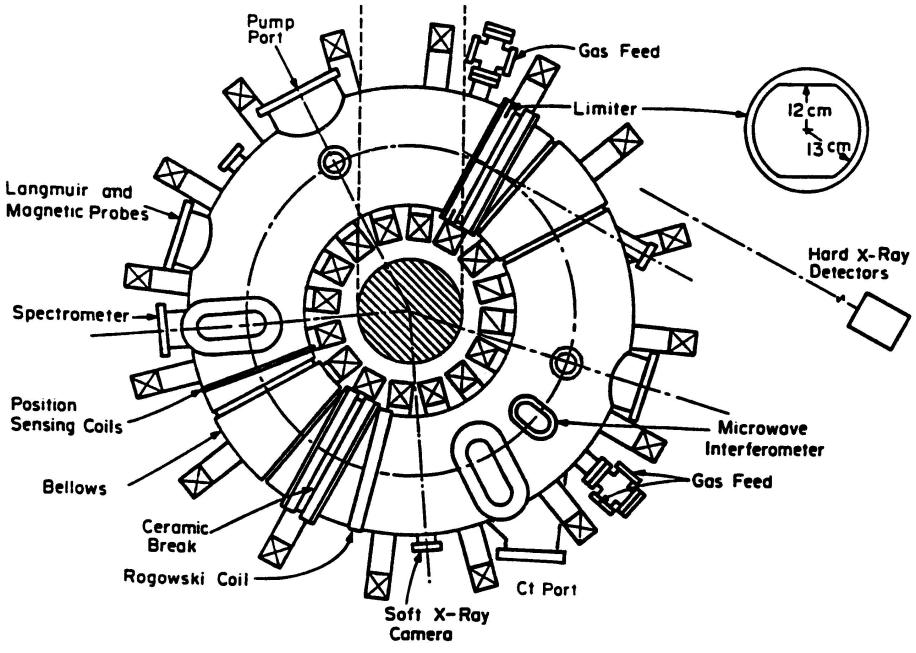

Figure 2.1: Top view of the STOR-M tokamak. The limiter is shown at the upper right conner. The position of some diagnostics has been changed from this figure.

Hydrogen gas in the plasma chamber is ionized and heated by the plasma current (Ohmic heating (OH) current), which is induced by an iron core transformer. The eight turns of OH coils are the primary coils of the transformer while the plasma in the chamber acts as a single-turn secondary coil (see Figure 2.2). The plasma current also generates poloidal magnetic field and consequent rotational transform which is needed for plasma confinement. The magnetic field in the tokamak is described below.

The toroidal magnetic field in the tokamak is produced by 16 uniformly spaced circular coils surrounding the machine chamber. Each coil consists of nine turns of copper conductor with a cross-section of $70 \times 6.4\ \mathrm{mm}^2$. The coils have a total inductance of 2.06 mH and a resistance of 13.5 Ω at room temperature [18]. They are powered by a capacitor bank of 15 mF charged to 4.7 kV (for $B_\phi = 0.7\ \mathrm{T}$) during discharge intervals. The major STOR-M parameters are shown in Table 2.1.

The toroidal magnetic field alone is unable to confine a plasma in toroidal geometry. The

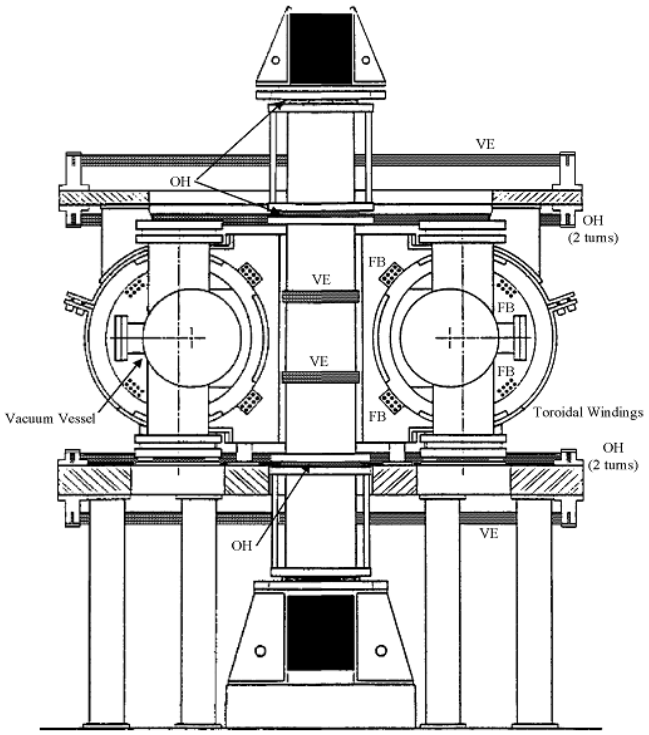

Figure 2.2: Side view of the STOR-M tokamak. OH, VE, and FB represent Ohmic heating, vertical equilibrium, and feedback coils, respectively.

Major Radius	R	46 cm
Minor Radius (Limiter)	a	12 cm
Toroidal Magnetic Field	B_Φ	1 T
Plasma Current	I_p	30 - 50 kA
Average Electron Density	n_e	1 - 3 $\times 10^{13}$ cm^{-3}
Electron Temperature	T_e	220 eV
Ion Temperature	T_i	50 - 100 eV
Discharge Duration	t_D	50 ms
Energy Confinement Time	τ_E	1 - 3 ms

Table 2.1: Primary parameters of the STOR-M tokamak [18].

gradient and curvature of the toroidal magnetic field cause magnetic drifts of electrons and ions in opposite directions, which creates a vertical electric field as shown in Figure 2.3. The field lets the plasma $\mathbf{E} \times \mathbf{B}$ drift radially outward and there is no equilibrium.

To avoid charge separation, a poloidal magnetic filed B_θ must be added. This can be created by a toroidal plasma current and the resultant total magnetic field become helical, which short circuits

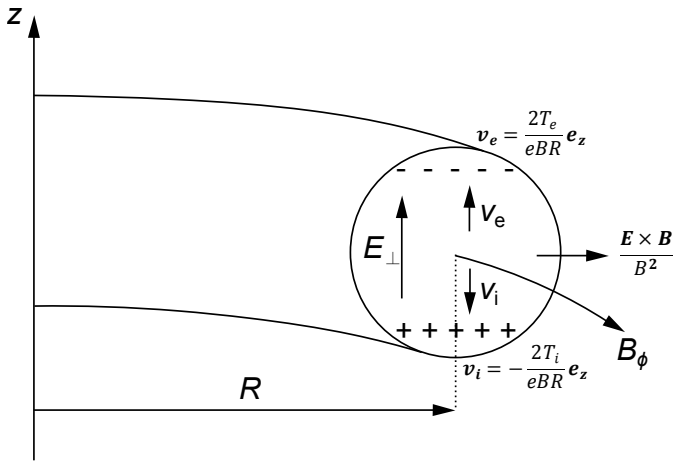

Figure 2.3: Simple toroidal field (no equilibrium). Charge separation and electric filed in a toroidal geometry with only toroidal magnetic filed.

the charge separation.

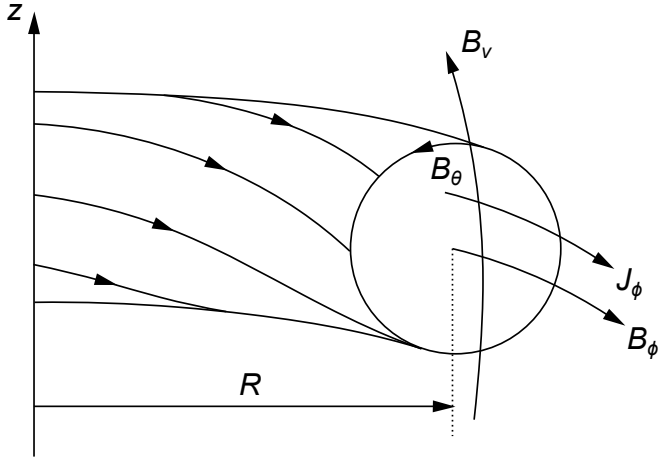

Figure 2.4: Helical magnetic field combines the toroidal and poloidal magnetic fields. Electric charges are not separated in this configuration.

Furthermore, to compensate for the radially (in $\boldsymbol{R}$ direction) outward force acting on the plasma ring, a vertical magnetic field $\boldsymbol{B}_v$ powered by the VE coils must be applied externally, whose magnitude is

$$B_v = \frac{\mu_0 I_p}{4\pi R}\left[\ln\left(\frac{8R}{a}\right) - \frac{3}{2} + \beta_p + \frac{l_i}{2}\right] \tag{2.1}$$

where β_p is the poloidal beta factor,

$$\beta_p = \frac{\bar{p}}{B^2(a)/2\mu_0} \tag{2.2}$$

$\bar{p}$ is the average plasma pressure, and l_i is the self inductance parameter:

$$l_i = \frac{2\pi \int_0^a B_\theta^2(r) r dr}{\pi a^2 B_\theta^2(a)} \tag{2.3}$$

Additionally, 32 turns of feedback coils around the chamber are powered by an active feedback system for real time plasma position control (labeled FB in Figure 2.2) [18]. They are also used for turbulent heating operation.

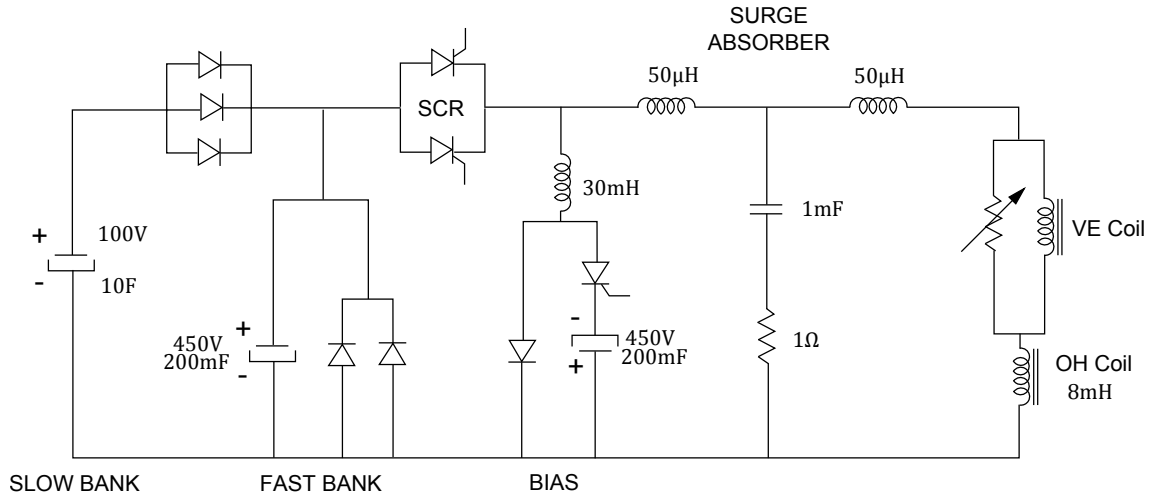

Figure 2.5: Capacitor bank circuit for Ohmic Heating and Vertical Equilibrium coils.

Figure 2.5 shows the capacitor bank circuit for Ohmic Heating and Vertical Equilibrium currents. The current through the VE and OH coils are provided by three capacitor banks - the bias bank (450 V, 200 mF) to negatively bias the transformer, fast bank (450 V, 200 mF) for current ramp-up, and the slow bank (100 V, 10 F) to maintain plasma current.

2.2 Major diagnostics of the STOR-M tokamak

2.2.1 Rogowski coils

In the STOR-M tokamak, the plasma current and the feedback current are measured by Rogowski coils. A Rogowski coil is an N-turn coil wound on a circular non-magnetic frame. It measures the change of magnetic flux Φ as

$$V_{RC} = -N\frac{d\Phi}{dt} \tag{2.4}$$

In the STOR-M tokamak, the Rogowski coil for plasma current measurement is constructed with 18 AWG enameled wires, while other Rogowski coils use 26 AWG wires. Circular frames with rectangular cross-section are used, as shown in Figure 2.6. To avoid coupling to the magnetic flux through the coil, the return wire is wound in the opposite direction in the same frame. The output signals are sent to the control room through 20-meter-long RG-58/U coaxial cables. The voltage signal is integrated by electric circuits and connected to data acquisition system. Therefore the current measured by a Rogowski coil can be derived from Equation (2.4) and Ampere's law [19]:

$$I = -\frac{2\pi R_R}{\mu_0 N a_R b_R}\int V_{RC}dt \tag{2.5}$$

where R_R is the radius of the Rogowski coil, a_R and b_R are the sides of the cross section, and V_{RC} is the measured voltage.

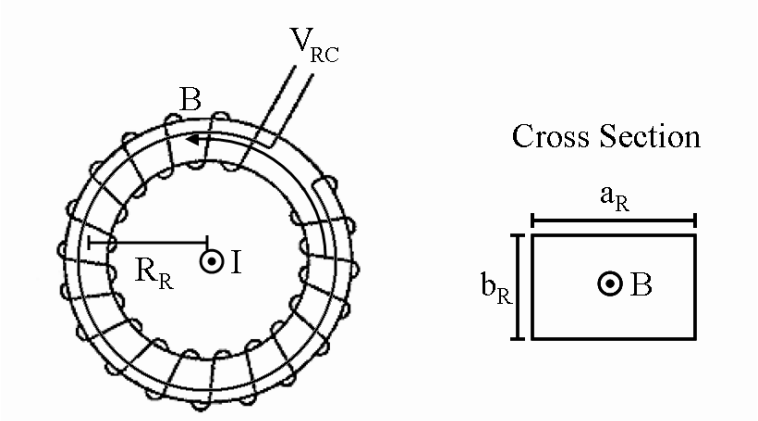

Figure 2.6: Circular Rogowski coil and its rectangular cross section.

2.2.2 Loop voltage

The plasma loop voltage is measured by a single-turn loop placed on top of the tokamak chamber. As shown in Figure 2.7, a voltage divider circuit is used to match the voltage signal to the data acquisition system. The plasma loop voltage consisting resistance and inductance components can be expressed by

$$V_l = R_p I_p + \frac{d}{dt}(L_p I_p) \tag{2.6}$$

where I_p is the plasma current, R_p is the plasma resistance, and L_p is the plasma inductance expressed as

$$L_p = \mu_0 R \left[\ln\left(\frac{8R}{a}\right) - 2 + \frac{l_i}{2} \right] \tag{2.7}$$

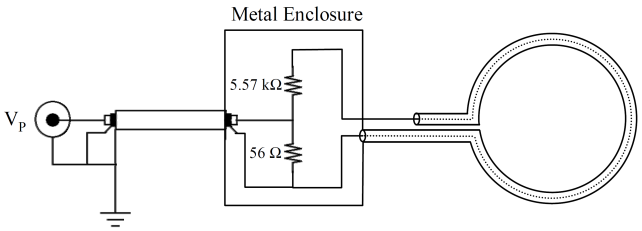

Figure 2.7: Loop Voltage pick-up loop circuit and its voltage dividing circuit [20].

2.2.3 Position sensing coils

Plasma position controlling is crucial for tokamak operation. In the STOR-M tokamak, the plasma position is detected by six magnetic coils shown in Figure 2.8. Four coils located on a circular contour of minor radius $r_m = 17$ cm separated by 90° measure the poloidal magnetic field B_θ, which is generated by the plasma current. Each coil has 460 turns of 0.1 mm diameter (AWG #38) wire wound on a cylindrical Teflon frame, and they have a frequency response of 200 kHz. Other two coils located above and below the chamber measure the radial magnetic field B_r [19].

Besides the position detecting coils, Rogowski coils in compensation circuits (Figure 2.9) are used to measure the unwanted toroidal magnetic fields pick-up due to coil misalignment and imperfection. The compensated signals were integrated with active integrators.

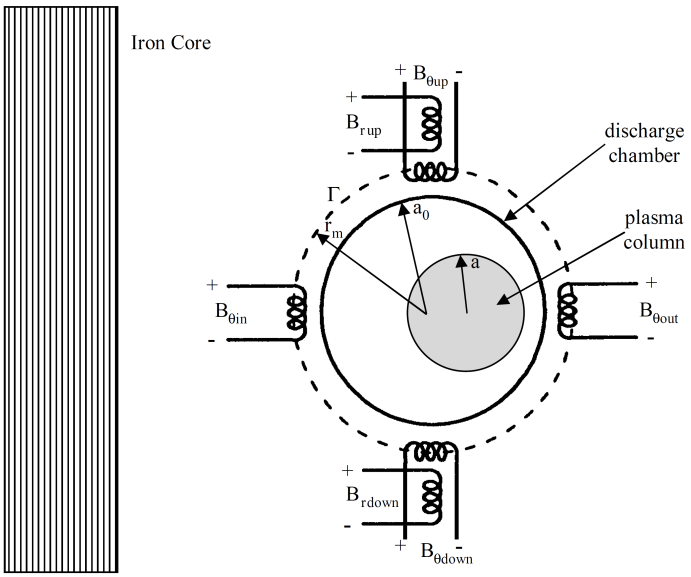

Figure 2.8: Plasma position detection coils. The $B_{\theta *}$ coils measure the poloidal magnetic field, and the B_{r*} coils measure the radial magnetic field.

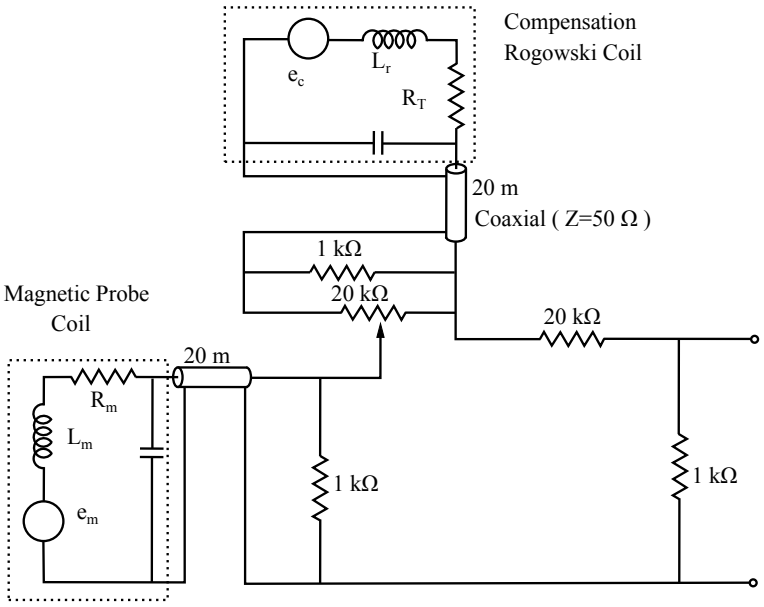

Figure 2.9: Compensation Circuit with Rogowski coil to measure the unwanted magnetic field.

2.2.4 Microwave interferometer

A 4-mm microwave interferometer system is used for electron density measurement in the STOR-M tokamak. The microwaves generated by a Gunn diode operating at 75 GHz are divided to three paths: one plasma path and two reference paths. The portion going through the plasma is phase-

shifted by

$$\Delta\Phi_\mu = \frac{2\pi}{\lambda}\int_{-a}^{a}\left(1-\sqrt{1-\frac{n_e(x)}{n_c}}\right)dx \tag{2.8}$$

where $n_e(x)$ is the local electron density, and n_c is the cutoff electron density for the given microwave frequency ω

$$n_c = \frac{m\epsilon_0\omega^2}{e^2} \tag{2.9}$$

Thus the electron density can be calculated from the microwave phase shift $\Delta\Phi_\mu$.

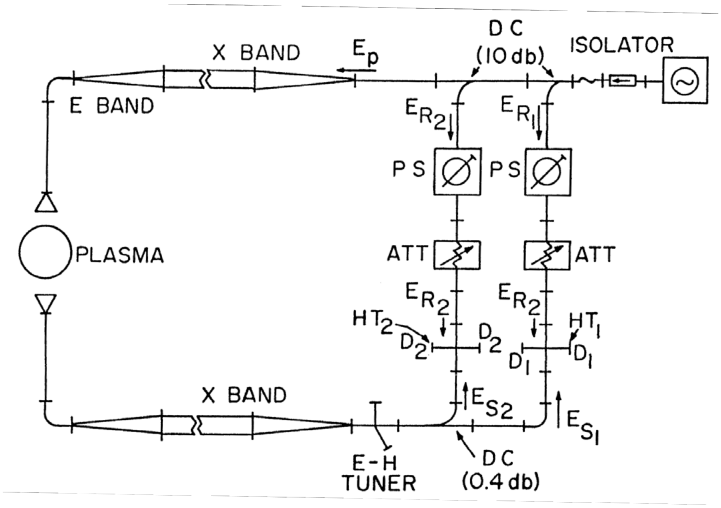

Figure 2.10: Schematic diagram of 4mm microwave interferometer for electron density measurement in STOR-M. The microwave is divided into one plasma path and two reference paths.

2.2.5 Optical spectrometers

Three optical spectrometers are used on the STOR-M tokamak to monitor the light emission by hydrogen atoms and impurity ions. The hydrogen H_α emission line (6562.8 Å) is measured by a 0.35 m focal length single-pass Czerny-Turner grating monochromator (Heath EU-700) with a relative aperture of f/6.8 and resolution of 1 Å [21]. The monochromator uses fiber optical bundle with optical lenses to collect light from a vertical window at the bottom of the STOR-M chamber. A photomultiplier tube (RCA IP-28) shield from the magnetic field with μ-metal and enclosed in a brass and copper housing detects the dispersed light. The H_α radiation indicates the recycling process of the plasma, and lower level is an indication of better confinement.

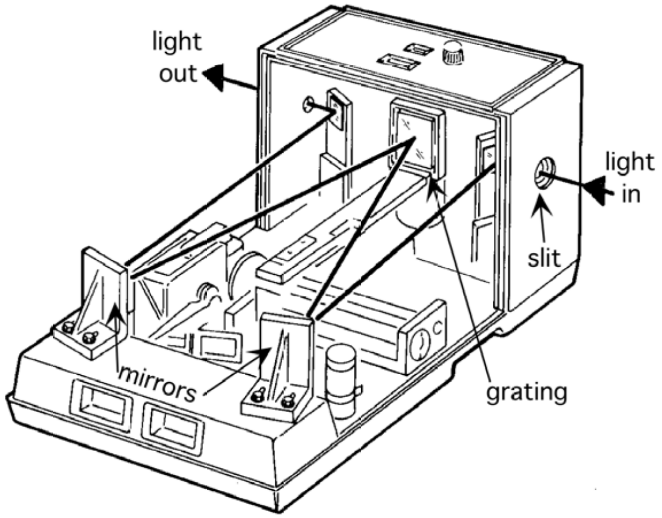

Figure 2.11: The Heath EU-700 spectrometer is a Czerny-Turner type. It has a focal length of 0.35m.

The second spectrometer is a miniature fiber optic spectrometer (Ocean Optics USB2000) controlled and powered by a PC via an USB port [22]. Quartz optical fiber is used and the spectrometer has a broad bandpass from 2000 to 9600 Å. It is equipped with a linear CCD with 2048 pixels thus the minimum resolution is 3.2 Å. This spectrometer is used for emission line identification in the full spectrum when high resolution is not needed.

Another Czerny-Turner spectrometer (SPEX 1702) in the Plasma Physics Laboratory (PPL) is used for the IDS system. It has 0.75 meter focal length and a 1200 grooves/mm refraction grating blazed at 5000 Å [23]. It is equipped with a cylindrical rod lens and a 16-channel multi-anode PMT (Hamamatsu R5900U-07-L16) for magnifying and recording spectra of various impurity lines. Detailed description of the IDS system is shown in Chapter 4.

2.3 Previous plasma flow velocity measurements in the STOR-M tokamak.

The plasma flow velocity in the STOR-M tokamak has been measured with various types of Mach probes, which collect the saturation currents at specific angular directions. Saturation currents are related to the flow velocity parallel to the magnetic field [24, 25].

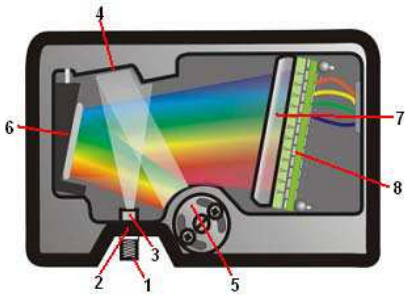

1: SMA Connector
2: Slit
3: Filter
4: Collimating Mirror
5: Grating
6: Focusing Mirror
7: L2 Detector Collection Lens
8: CCD Detector

Figure 2.12: Schematic diagram of Ocean Opics USB2000 spectrometer. It is able to measure a full spectrum from 2000 Å to 9600 Å.

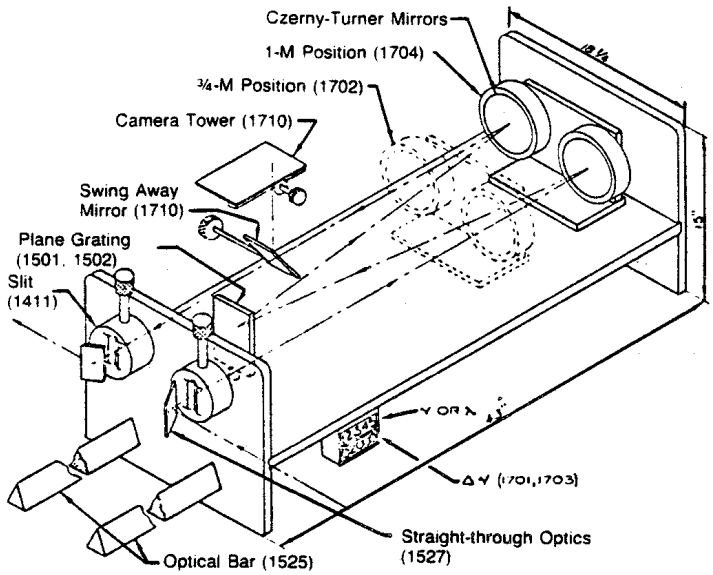

Figure 2.13: Schematic diagram of the SPEX 1702 spectrometer. It has longer focal length and better resolution than other two spectrometers.

C. Xiao *et al.* used an four-sided Mach probe to measure the toroidal and poloidal flow velocities in the STOR-M tokamak with electrode biasing experiments [26]. The velocities were measured from r = 10 cm to r = 14 cm. In normal discharges without electrode biasing, the toroidal Mach number was found to be about 0.5, corresponding to a velocity of 15 km/s along the plasma current direction, and it is insensitive to the radial position. The structure of the probe and the results are shown in Figures 2.14 and 2.15.

Another type of Mach probe - Gundestrup probe (G-probe) - consisting eight collectors was also used for flow measurement [27]. The G-probe measured a toroidal flow velocity about 15 km/s co-currently from r = 10.0 cm to r = 13.5 cm (see Figures 2.16 and 2.17), which is consistent

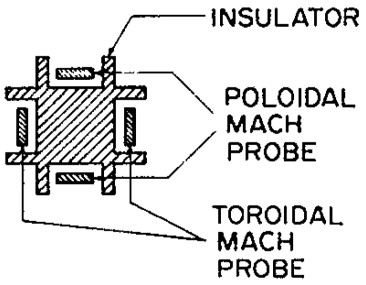

Figure 2.14: Structure of the four-sided Mach probe. Each pairs of the probe collectors measure corresponding flow velocities.

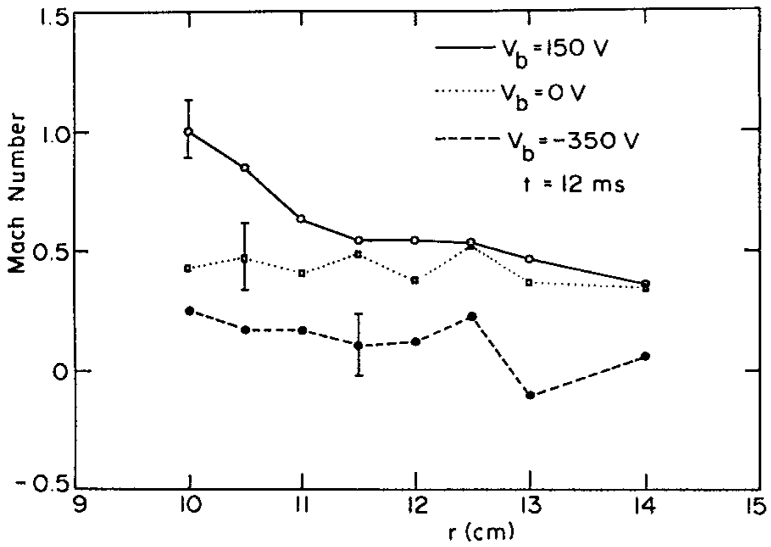

Figure 2.15: Toroidal flow velocity measured by the four-sided Mach probe. One unit Mach number corresponds to 30 km/s.

with the four-sided Mach probe result.

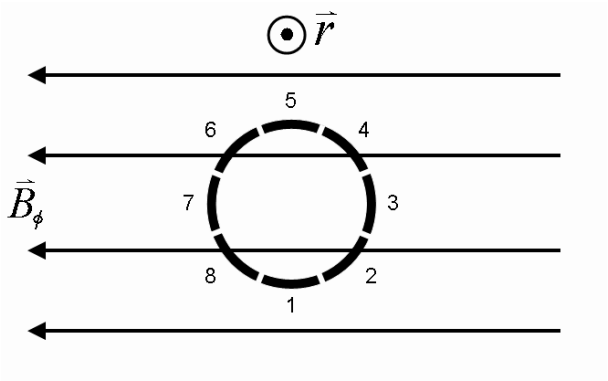

Figure 2.16: The arrangement of the eight collectors of the G-probe.

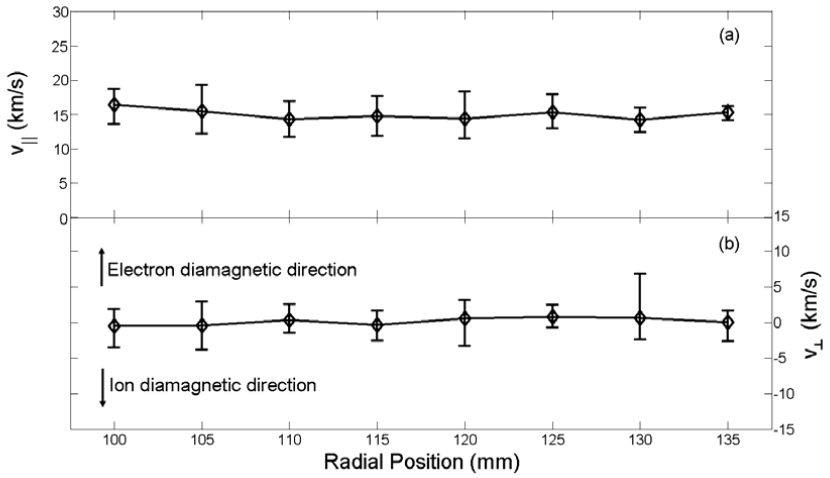

Figure 2.17: Parallel and perpendicular flow velocities measured by the G-probe during normal Ohmic heating discharges.

Chapter 3

Ion flow velocity measurement theories

3.1 Impurities Emission

Electromagnetic radiation occurs omnipresently in plasma. Free electrons radiate electromagnetic waves via acceleration as in cyclotron and bremsstrahlung radiation [28]. Electrons in the atoms and ions falling from higher energy levels to lower ones also emit light, which provides information about drift velocity and temperature of the atoms and ions. In the STOR-M tokamak, H_α line from atoms of the major working gas - hydrogen - is routinely monitored to assess recycling rate qualitatively. Hydrogen ions do not emit light due to the lack of electron. Thus, impurities ions such as carbon and oxygen are commonly used in magnetic fusion devices for plasma flow and ion temperature measurements.

Carbon and oxygen ions have multiple ionization states. Figures 3.1 and 3.2 show the abundance of carbon and oxygen ionization states at different electron temperatures. Obviously, higher ionization states are more abundant at higher electron temperatures because they require higher energy for ionization. In these two figures, the Arabic numbers on top of the curves indicate the ionization stages, starting from number "1" for neutral atoms, while Roman numbers are more commonly used in the literature. In the STOR-M tokamak, the average electron temperature has been estimated to be 220 eV [18]. At this temperature, carbon and oxygen emission lines should be observable from lower ionization states to $\mathrm{C_{VI}}$ and $\mathrm{O_{VIII}}$. In fact, emission lines from $\mathrm{C_{III}}, \mathrm{O_V}, \mathrm{C_{VI}}$ are used for flow velocity measurement.

Carbon and oxygen in fusion devices can originate from various sources, such as the contami-

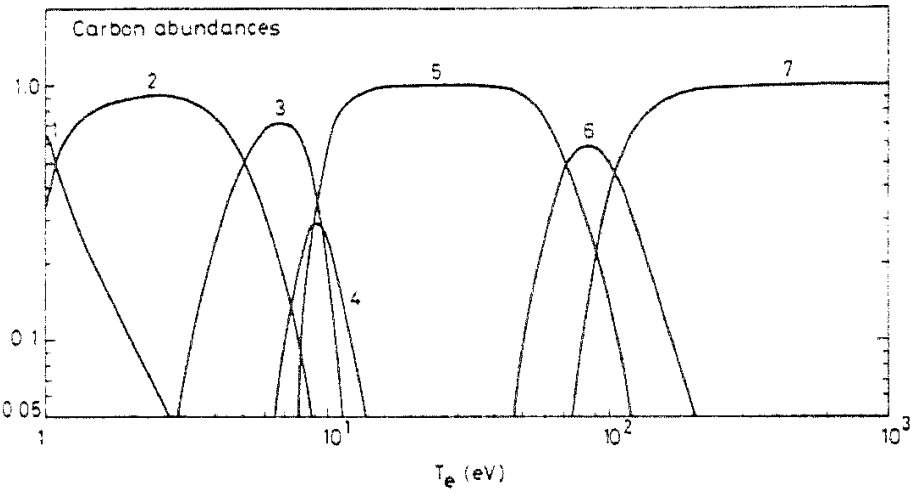

Figure 3.1: The carbon equilibrium ionization state distribution [29]. The Arabic numbers on top of the curves indicate the ionization stages, starting from number "1" for neutral atoms.

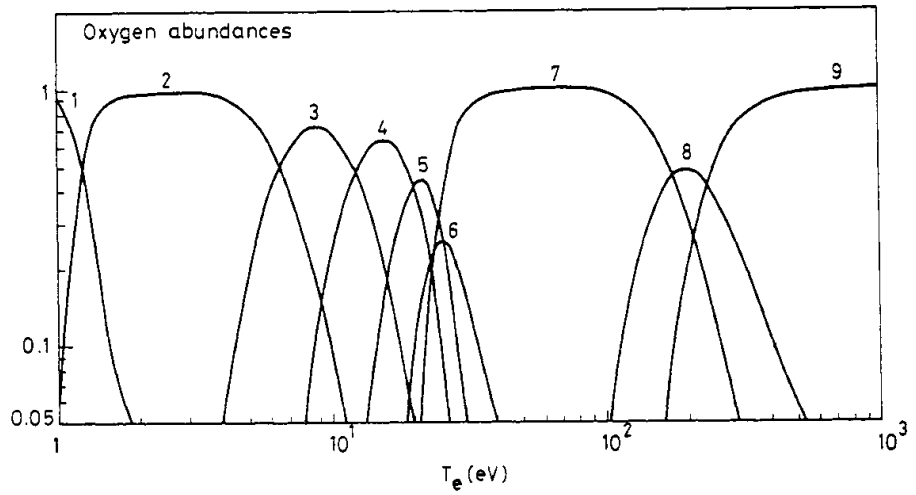

Figure 3.2: The oxygen equilibrium ionization state distribution [29]. The Arabic numbers on top of the curves indicate the ionization stages, starting from number "1" for neutral atoms.

nation by vacuum pump oil, outgassing from the chamber walls, as well as organic materials used for fabricating probes inserted into the chambers. Impurity gas may be puffed to enhance light emission.

However, in large scale tokamaks, electron temperature is much higher than that of smaller devices. The impurity elements are fully ionized and unable to emit light via electron transition. Charge-exchange induced by neutral beam injection (NBI) is commonly used to transfer electrons from hydrogen atoms to fully ionized carbon and oxygen [30, 31, 32]. A typical charge-exchange

process is the interaction between hydrogen atom H and fully ionized carbon ion C^{6+}, as

$$\begin{aligned} H + C^{6+} &\rightarrow H^{+} + C^{5+*} \\ &\rightarrow H^{+} + C^{5+} + h\nu \end{aligned} \tag{3.1}$$

where the C^{5+*} represents the carbon ion with one electron in excitation state, and the C^{5+} is the one in lower energy level. The energy of the emitted photon is represented by $h\nu$, the product of Planck constant h and light frequency ν.

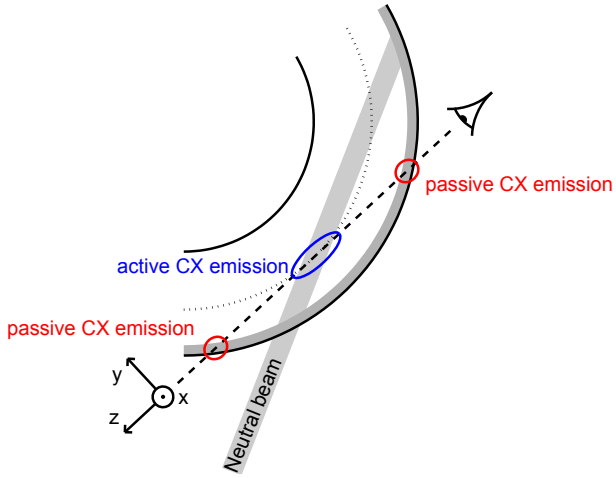

Figure 3.3: Charge exchange induced by neutral beam injection. The observed line emission is the combination of active and passive CX reactions [32].

3.2 Plasma flow mechanism

In plasmas, the flow velocity is essentially equal to the ion velocity, because of the much larger ion mass m_i than electron mass m_e:

$$\boldsymbol{v} = \frac{m_i \boldsymbol{v_i} + m_e \boldsymbol{v_e}}{m_i + m_e} \approx \boldsymbol{v_i} \tag{3.2}$$

where $\boldsymbol{v}$, $\boldsymbol{v}_i$ and $\boldsymbol{v}_e$ are the plasma, ion and electron velocities. In tokamaks, the plasma flow velocity $\boldsymbol{v}$ can be decomposed into the geometric directions (toroidal and poloidal) $\boldsymbol{v}_\phi$ and $\boldsymbol{v}_\theta$, or to the parallel and perpendicular directions $\boldsymbol{v}_\parallel$ and $\boldsymbol{v}_\perp$ with respect to the total magnetic field $\boldsymbol{B}$. These two decompositions are shown in Figure 3.4. Usually, the geometric coordinate is used in optical

measurement; in contrast, the Mach probes usually measure the flow in parallel or perpendicular directions with respect to the magnetic field.

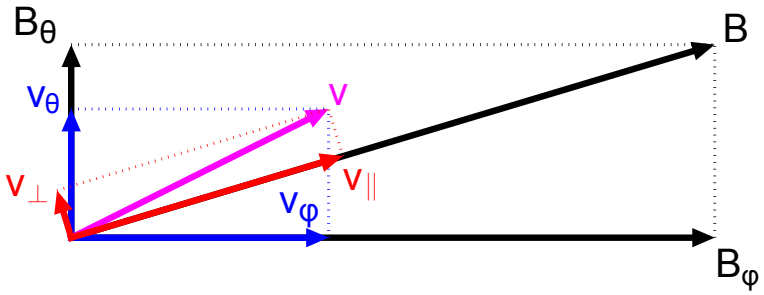

Figure 3.4: Two velocity decompose coordinates

The equation of motion for impurity ions is

$$Mn\left[\frac{\partial}{\partial t}+(\boldsymbol{v}\cdot\boldsymbol{\nabla})\right]\boldsymbol{v}=Zen\left(\boldsymbol{E}+\boldsymbol{v}\times\boldsymbol{B}\right)-\nabla p_i \tag{3.3}$$

where $\boldsymbol{E}$ and $\boldsymbol{B}$ are the electric and magnetic fields, p_i is the ion pressure, and Z is the ion charge. In steady state ($\partial/\partial t=0$) with negligible Reynolds stress, Equation(3.3) reduces to

$$Zen\left(\boldsymbol{E}+\boldsymbol{v}\times\boldsymbol{B}\right)-\nabla p_i=0 \tag{3.4}$$

The perpendicular velocity can be calculated by taking the cross product of magnetic field $\boldsymbol{B}$ to Equation (3.4)

$$\boldsymbol{v}_\perp=\frac{\boldsymbol{E}\times\boldsymbol{B}}{B^2}+\frac{1}{Zne}\frac{\boldsymbol{B}\times\nabla p_i}{B^2} \tag{3.5}$$

here the first term

$$\boldsymbol{v}_{E\times B}=\frac{\boldsymbol{E}\times\boldsymbol{B}}{B^2} \tag{3.6}$$

is the $\boldsymbol{E}\times\boldsymbol{B}$ drift velocity, and the second term

$$\boldsymbol{v}_{dia}=\frac{1}{Zne}\frac{\boldsymbol{B}\times\nabla p_i}{B^2} \tag{3.7}$$

is the diamagnetic drift. It is noted that $\boldsymbol{v}_{E\times B}$ is the guiding center drift while $\boldsymbol{v}_{dia}$ is not.

The effect of toroidal electric field E_ϕ on the flow is fairly small as it mostly drives the electrons rather than the ions. In a tokamak, the magnetic field is inhomogeneous because of the toroidal

shape of the chamber. The toroidal magnetic field is stronger in the inner side and weaker in the outer side. It can be expressed as

$$B_\phi \simeq B_0 \left(1 - \frac{r}{R}\cos\theta\right) \tag{3.8}$$

where r/R is the inverse aspect ratio and θ is the poloidal angle. The plasma flow in θ direction experiences a periodic variation of the magnetic field which called magnetic pumping. Thus the poloidal rotation is damped except for the neoclassial contribution due to the ion temperature gradient. The toroidal rotation velocity based on the radial force balance is

$$v_\phi = \frac{1}{B_\theta}\left(E_r - \frac{T_i}{Zen}\frac{dn}{dr}\right) \tag{3.9}$$

In the core region, v_ϕ is in the same direction of the plasma current but in the periphery region, the flow is reversed. It is also seen from Equation (3.9) that the toroidal velocity v_ϕ is inversely proportion to the poloidal magnetic field B_θ. The inversion relationship between the poloidal magnetic field and the toroidal flow velocity is experimentally confirmed by reversing the plasma current direction. Since the poloidal magnetic field is generated by the plasma current, the reversal of plasma current direction causes a reversal of the poloidal magnetic field, and therefore reverse the toroidal rotation directions of the ions.

3.3 Doppler shift and broadening

Ion Doppler Spectroscopy is based on the effect that the light frequency ν_0 emitted by an object moving at velocity v shifts from ν_0 to ν_D

$$\nu_D = \nu_0 \times \frac{\sqrt{1 - \frac{v^2}{c^2}}}{1 - \frac{v}{c}\cos\beta} \tag{3.10}$$

where c is the speed of light, and β is the angle between the direction of movement and that of observation. Since the flow velocity in a tokamak is much less than the speed of light, the first

order approximation can be applied to Equation (3.10) as

$$\begin{aligned} \nu_D &\simeq \nu_0 \times \left(1 - \frac{1}{2}\frac{v^2}{c^2}\right) \times \left(1 + \frac{v}{c}\cos\beta\right) \\ &\simeq \nu_0 \left(1 + \frac{v}{c}\cos\beta\right) \end{aligned} \tag{3.11}$$

When the light source is approaching the observer collinearly, $\beta \simeq 0$ and $\cos\beta \simeq 1$.

$$\nu_D = \nu_0 \left(1 + \frac{v}{c}\right) \tag{3.12}$$

Therefore, the frequency shift is proportional to the velocity

$$\Delta\nu = \nu_D - \nu_0 = \nu_0 \frac{v}{c} \tag{3.13}$$

In practice, the wavelength λ of a light source is known, which is related to the frequency ν by the equation

$$\nu\lambda = c \tag{3.14}$$

Taking the derivative of Equation (3.14), one has

$$\frac{\Delta\nu}{\nu} = -\frac{\Delta\lambda}{\lambda} \tag{3.15}$$

The combination of Equations (3.13) and (3.15) gives

$$v = c\frac{\Delta\nu}{\nu_0} = -c\frac{\Delta\lambda}{\lambda_0} \tag{3.16}$$

and

$$\Delta\lambda = -\lambda_0 \frac{v}{c} \tag{3.17}$$

where $\Delta\lambda$ is the wavelength shift and λ_0 is the original wavelength.

In tokamaks, ions possess Maxwell velocity distribution as

$$f\left(\boldsymbol{u}, T_i\right) = \left(\frac{m}{2\pi T_i}\right)^{3/2} e^{-\frac{m(\boldsymbol{u}-\boldsymbol{v})^2}{2T_i}} \tag{3.18}$$

where m is the ion mass, T_i is the ion temperature, $\boldsymbol{u} = u_x\boldsymbol{e}_x + u_y\boldsymbol{e}_y + u_z\boldsymbol{e}_z$ is the total velocity, and $\boldsymbol{v} = v_x\boldsymbol{e}_x + v_y\boldsymbol{e}_y + v_z\boldsymbol{e}_z$ is the flow velocity.

In the IDS measurement, since only the parallel ion velocity is effective for the Doppler shift, the one dimension Maxwellian distribution is used, which is

$$f\left(u_x, T_i\right) = \left(\frac{m}{2\pi T_i}\right)^{1/2} e^{-\frac{m(u_x - v_x)^2}{2T_i}} \tag{3.19}$$

Therefore, the averaged Doppler shift is

$$\begin{aligned} \langle \Delta\lambda \rangle &= \int \Delta\lambda f\left(u_x, T_i\right) \mathrm{d}u_x \\ &= -\frac{\lambda_0}{c} \int u_x f\left(u_x, T_i\right) \mathrm{d}u_x \\ &= -\frac{\lambda_0}{c} v_x \end{aligned} \tag{3.20}$$

and the full width at half maximum (FWHM) can be calculated as

$$e^{-\frac{m(\frac{\lambda_{FWHM}}{2}\frac{c}{\lambda_0})^2}{2T_i}} = \frac{1}{2} \tag{3.21}$$

therefore

$$\lambda_{FWHM} = 2\lambda_0 \left(\sqrt{T_i/m}/c\right) \sqrt{2\ln 2} \tag{3.22}$$

From Equations (3.20) and (3.22), the magnitude of ion flow velocity and ion temperature can be interpreted from the Doppler shift and broadening, respectively:

$$v = \frac{\Delta\lambda}{\lambda_0} c \tag{3.23}$$

and

$$T_i = \frac{\lambda_{FWHM}^2 \cdot c^2}{4\lambda_0^2 \cdot 2\ln 2} m \tag{3.24}$$

3.4 Spectral line broadening

3.4.1 Line broadening effects

Besides Doppler broadening, other broadening effects also act on the tokamak emission lines, namely, instrumental broadening, natural broadening, and Zeeman splitting.

The instrumental broadening is caused by the dispersion and the imperfection of the instruments. It varies as the entrance slit changes its width. This broadening can be experimentally measured and adjusted. Ideally, the line profile of instrumental broadening has a triangular or trapezoid shape [33]. However, if the input slit is not too wide, instrumental broadening can be described by a Gaussian function.

The natural broadening is caused by the finite lifetime of the energy levels. According to the principle of uncertainty

$$\Delta E \Delta t \approx \hbar = h/2\pi \tag{3.25}$$

the energy levels also have certain amount of width. Natural broadening is very small compared with other broadening effects.

The magnetic field in the tokamak plasma can split the electron energy levels in atoms and ions, causing splitting in the spectrum lines. This phenomenon is called Zeeman effect. In a simple case, Zeeman effect splits a single spectral line of wavelength λ is into three lines $\lambda - \Delta\lambda$, λ, and $\lambda + \Delta\lambda$. The $\Delta\lambda$ can be calculated from

$$\Delta\lambda = \frac{\lambda^2}{c}\frac{\Delta E}{h} \tag{3.26}$$

where $\Delta E = m_l \nu_B B$, m_l is the magnetic number, $\nu_B = 9.27 \times 10^{-24}$ J/T is the Bohr magneton, and B is the magnetic strength. For the STOR-M tokamak with toroidal magnetic field strength of 1 T, measuring $\mathrm{C_{III}}$ line of 4647.4 Å, the Zeeman broadening can be estimated to $\Delta\lambda = 0.1$ Å.

Another broadening mechanism is the Stark effect due to split of electron energy levels by electric field. The final effect of the broadening mechanism is the superposition of all broadenings effects. The amount of broadening directly affects the ion temperature determination. However in our experiments, since only the centroid of the line emission profile is used for shift determination, the broadening width is not crucial for flow measurement.

3.4.2 Superposition of broadening effects

As introduced before, there are many effects causing spectrum line broadening. Analytically, the superposition of these broadening effects are the convolution of the line profile functions. The typical superposition of two Gaussian functions is introduced here.

In the Gaussian-Gaussian superposition type, the two functions $g_i(x)(i = 1, 2)$ can be denoted as

$$g_i(x) = A_i \mathrm{e}^{-\frac{(x-b_i)^2}{2\sigma_i^2}} \tag{3.27}$$

where A_i is a normalization factor, b_i is the shift, and $\sigma_i = FWHM/2\sqrt{ln2}$ is the standard deviation. The convolution function $G(x)$ of these two Gaussian functions is

$$\begin{aligned}
G(x) &= \int g_1(x')g_2(x-x')dx' \\
&= \int \left[A_1 \mathrm{e}^{-\frac{(x'-b_1)^2}{2\sigma_1^2}} \times A_2 \mathrm{e}^{-\frac{(x-x'-b_2)^2}{2\sigma_2^2}} \right] dx' \\
&= A_1 A_2 \int \mathrm{e}^{-\left[\frac{(x'-b_1)^2}{2\sigma_1^2}+\frac{(x-x'-b_2)^2}{2\sigma_2^2}\right]} dx' \\
&= A_1 A_2 \mathrm{e}^{-\left(\frac{1}{2\sigma_1^2}+\frac{1}{2\sigma_2^2}\right)\frac{(x+b_1-b_2)^2\sigma_1^2\sigma_2^2}{\sigma_1^2+\sigma_2^2}} \int \mathrm{e}^{-\left(\frac{1}{2\sigma_1^2}+\frac{1}{2\sigma_2^2}\right)\left(x'-\frac{b_1\sigma_2^2+(b_2-x)\sigma_1^2}{\sigma_1^2+\sigma_2^2}\right)^2} dx' \\
&= \frac{A_1 A_2}{\sqrt{\frac{1}{2\sigma_1^2}+\frac{1}{2\sigma_2^2}}} \mathrm{e}^{-\frac{(x-(b_2-b_1))^2}{2(\sigma_1^2+\sigma_2^2)}}
\end{aligned} \tag{3.28}$$

This expression of the convoluted function is also a Gaussian function with the standard deviation

$$\sigma = \sqrt{\sigma_1^2 + \sigma_2^2} \tag{3.29}$$

Since the FWHM is proportional to the standard deviation, the final FWHM is also the root of quadratic sum of the two FWHMs.

$$FWHM = \sqrt{FWHM_1^2 + FWHM_2^2} \tag{3.30}$$

In a plasma, due to multiple broadening effects, the measured plasma broadening is the convolution of all broadening effects. Approximately, if all broadening effects can be described by

Gaussian functions, the final broadening measured by the FWHM is the root of quadratic sum of them, as

$$\Delta\lambda_{total} = \sqrt{(\Delta\lambda_{Doppler})^2 + (\Delta\lambda_{Instrumental})^2 + ...} \tag{3.31}$$

Then the Doppler broadening can be calculated as

$$\Delta\lambda_{Doppler} = \sqrt{(\Delta\lambda_{Total})^2 - (\Delta\lambda_{Instrumental})^2 - ...} \tag{3.32}$$

3.4.3 The estimated Doppler broadening

Doppler broadening can be estimated from the Equation (3.22). It is depending on the ion temperature and ion mass. For multiple impurity ions, carbon and oxygen, the Doppler broadening is estimated as shown in Table 3.1.

Impurity Type	C_{III}	C_{VI}	O_{II}	O_{III}	O_{IV}	O_{V}
Atomic Weight	12	12	16	16	16	16
Emission Line Wavelength / Å	4647.4	5290.5	4414.9	3759.9	3736.9	6500.2
Ion Temperature / eV	Doppler Broadening/Å					
10	0.33	0.37	0.27	0.23	0.23	0.40
20	0.46	0.53	0.38	0.32	0.32	0.56
30	0.57	0.64	0.47	0.40	0.39	0.69
40	0.65	0.74	0.54	0.46	0.46	0.79
50	0.73	0.83	0.60	0.51	0.51	0.89
60	0.80	0.91	0.66	0.56	0.56	0.97
70	0.86	0.98	0.71	0.61	0.60	1.05
80	0.92	1.05	0.76	0.65	0.64	1.12
90	0.98	1.12	0.81	0.69	0.68	1.19
100	1.03	1.18	0.85	0.72	0.72	1.25

Table 3.1: Estimated broadening of various emission lines from a ion temperature range from 10 to 100 eV.

For ion temperature in the range from 10 to 100 eV, the Doppler broadening of the possible carbon and oxygen emission lines are less than 1.3 Å. Considering other broadening effects, if they are comparable with Doppler broadening, it is appropriate to set the measurement range in

$1.5 \sim 3$ Å. This means the wavelength difference between neighboring channels of the 16-channel PMT is $0.1 \sim 0.2$ Å. Too large measurement range would sacrifice the resolution per channel of the PMT and finally cause large error in the velocity measurement. This is important in designing the IDS parameters especially the linear dispersion. If the wavelength range is too small, only a fraction of the spectrum can be detected, which also causes large error.

Chapter 4

Ion Doppler spectrometer structure and calibration

4.1 Introduction

The structure of the Ion Doppler Spectrometer (IDS) is shown in Figure 4.1. The light collected through the tokamak ports are conveyed to the spectrometer via optical fibers. Magnified spectra are recorded by a photomultiplier tube (PMT). The detail of each part is described in Sections 4.2, 4.3, and 4.4. Section 4.5 shows the alignment process. The calibration was performed and shown in Section 4.6. The last two sections show the methodology of data analysis and the error analysis.

4.2 The Czyner-Turner spectrometer

The IDS system is built based on a Czerny-Turner type 0.75-meter-long spectrometer with a reflection grating of 1200 grooves/mm, mounted on a motor drive with adjustable wavelength scanning speed from $0.4\ \text{Å}/\text{min}$ to $1000\ \text{Å}/\text{min}$. The width of the entrance slit is adjustable from 0 mm to 3 mm with a minimum division of 2 μm. A manual knob is also available for rotating the grating to the needed wavelength through a sinusoid bar. The wavelength display has an accuracy of ± 0.1 Å. The error of grating positioning is obviously too large for the flow measurement in the tokamak. For example, if there is $\delta\lambda = 0.1$ Å error on the $\text{C}_{\text{III}}(4647.4\ \text{Å})$ emission line, the error on the flow velocity δv would be:

$$\delta v = \frac{\delta\lambda}{\lambda_0} \times c = \frac{0.1\ \text{Å}}{4647.4\ \text{Å}} \times 3 \times 10^5\ \text{km/s} = 6.5\ \text{km/s} \tag{4.1}$$

To avoid the error caused by grating positioning, the spectrometer grating must be fixed during measurement, unlike other IDS systems [12, 13]. For flow velocity calculation, the difference between the shifted and unshifted wavelengths

$$\Delta\lambda = \lambda_{\text{shifted}} - \lambda_{\text{unshifted}} \tag{4.2}$$

should be measured. In STOR-M, the unshifted wavelength is measured from a normal port of the tokamak, and the Doppler shifted wavelength is collected from the tangential port. Therefore, there is no mechanical movement of the diffraction grating during the measurement process.

Inside the spectrometer, the light rays entering the entrance slit is collimated by a concave mirror. The collimated light is diffracted by the grating to different angles depending on the wavelength of the light. The diffracted light is focused by the second concave mirror to the exit focal plane. Different wavelength is focused on different spacial position. This effect is called dispersion, which is described by the equation

$$d(\sin\alpha + \sin\beta) = m\lambda \tag{4.3}$$

where d is the grating spacing, α and β are the angles of incidence and reflection, respectively, λ is the wavelength, and m is the diffraction order. From Equation (4.3), it can be perceived that the longer wavelength is diffracted to the larger diffraction angle. By taking differential of both sides of the Equation (4.3), the angular dispersion equation can be derived:

$$\frac{d\beta}{d\lambda} = \frac{m}{d\cos\beta} \tag{4.4}$$

Practically, a more commonly used parameter is the reciprocal linear dispersion, which is the ratio of the diffracted wavelength to the distance at the focal plane of a spectrometer,

$$\frac{d\lambda}{dl} = \frac{d\lambda}{fd\beta} = \frac{d\cos\beta}{fm} \tag{4.5}$$

where f is the focal length of the spectrometer. For the spectrometer used in this thesis, the linear dispersion is approximately $10\text{Å}/\text{mm}$ in the visible range [23].

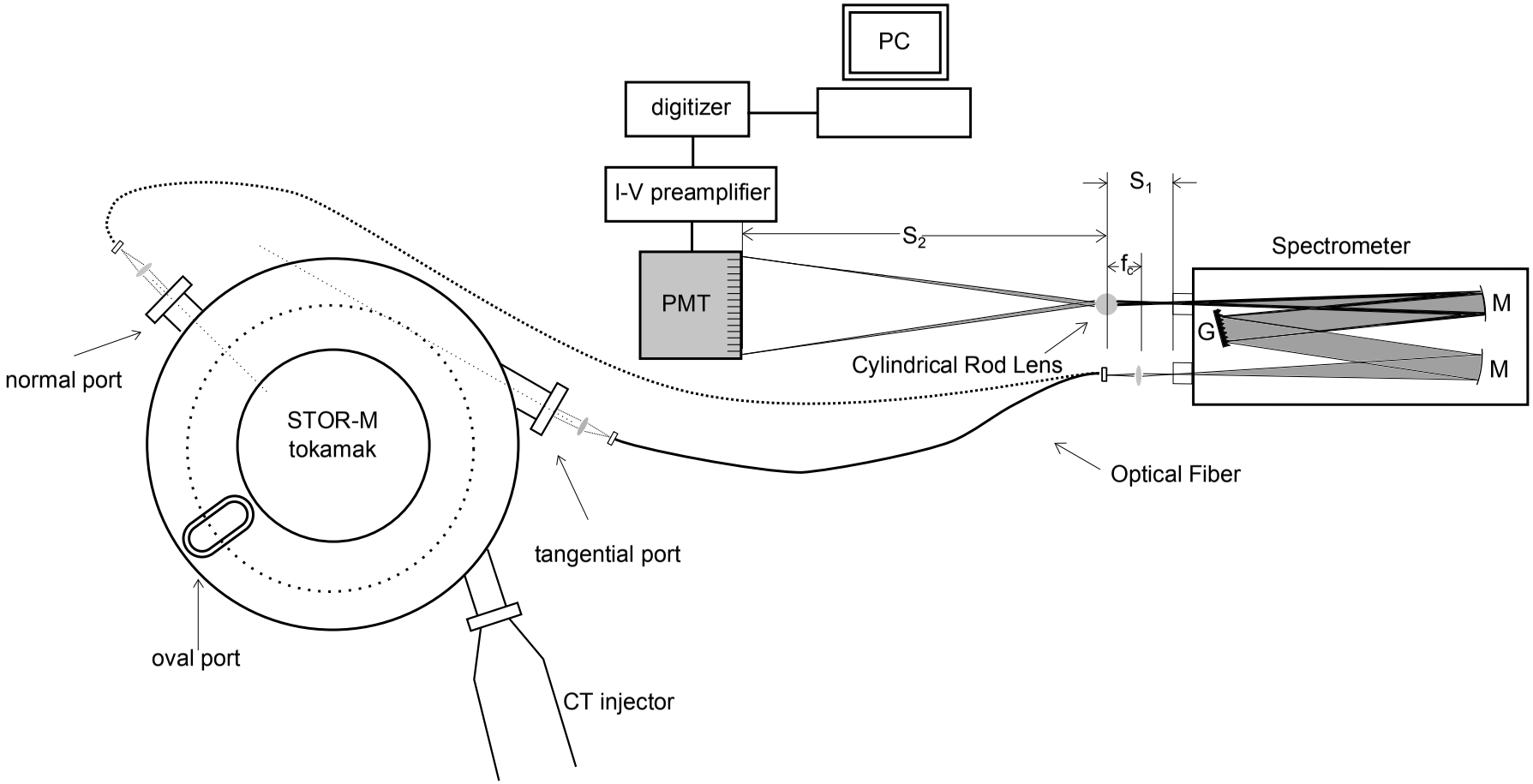

Figure 4.1: The schematic diagram of the IDS system. The light collected from the tokamak ports is conveyed by a optical fiber to the spectrometer input slit. It is collimated by a concave mirror, diffracted by a refraction grating, and focused by another concave mirror to the exit of the spectrometer. A cylindrical rod lens magnifies the spectrum to the PMT surface.

The resolution of a spectrometer is mainly limited by two factors: the diffraction limit of the grating and the effect of finite input slit width. The diffraction limit of grating can be calculated from the angular diffraction limit of an optical system:

$$\Delta\theta \equiv \frac{\Delta l}{f} = \frac{\lambda}{D} \tag{4.6}$$

where D is width of the diffraction grating, as shown in Figure 4.2. In combination with Equation (4.5), one can get

$$\begin{aligned} \Delta\lambda &= \Delta l \frac{d\cos\beta}{fm} \\ &= \frac{\lambda}{D}\frac{d\cos\beta}{m} \end{aligned} \tag{4.7}$$

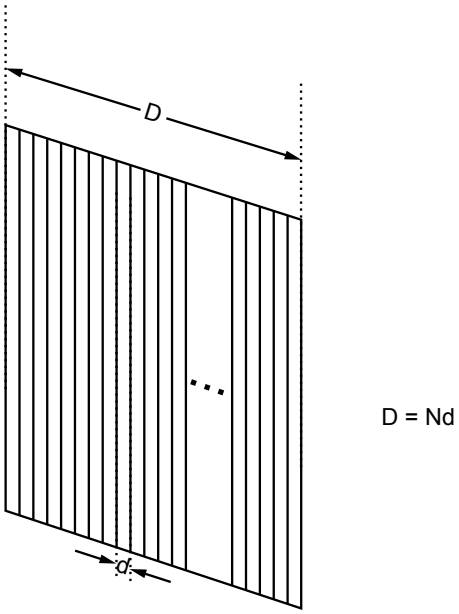

Figure 4.2: The refraction grating. It has N grooves and the distance between neighboring groove is d.

In the case of small diffraction angle $\cos\beta \approx 1$ and using the total ruling number $N = D/d$, The diffraction limit of a grating can be expressed as:

$$\Delta\lambda = \frac{\lambda}{mN} \tag{4.8}$$

For the IDS system used on STOR-M, $m = 1$ and $N = 1200\ \text{grooves/mm} \times 102\ \text{mm} = 1.22 \times 10^5\ \text{grooves}$. For a typical wavelength of 5000 Å, the resolution caused by the diffraction limit is

$$\Delta\lambda = \frac{5000\ \text{Å}}{1.22 \times 10^5} = 0.042\ \text{Å} \tag{4.9}$$

This is a very small quantity. In contrast, the effect of finite input slit width is the product of reciprocal dispersion $d\lambda/dl$ and the input slit width w:

$$\Delta\lambda = \frac{d\lambda}{dl} w \tag{4.10}$$

For a typical input slit width of $30\ \mu\text{m}$, it corresponds to a resolution of $\Delta\lambda = 0.3$ Å, which is much larger than the one caused by the diffraction limit. However, other factors can also affect the resolution of a spectrometer, such as the height of the input slit width. In practice, the resolution of the spectrometer is measured during the calibration process, which will be introduced in the Section 4.5.

4.3 The entrance optics

The light from the tokamak is conveyed to the spectrometer through an 6-meter-long optical fiber bundle consisting 12 fused silica fibers. The fibers have a diameter of 0.5 mm. A normal and a tangential port are used for observing the unshifted and shifted wavelength, respectively. Both of them can transmit U.V. and visible light, and are located at the mid-plane of the tokamak chamber. They have the same diameter of 1.75 inches. The normal port has a line of sight in the radial direction, and the line of sight of the tangential port is tangential to the central line of the tokamak chamber. (See Figure 4.1.)

The collimating light from the observation windows is focused to the optical fiber bundle by a converging lens, which is also made of fused silica. At the tokamak end of fiber bundle, the fibers are close-packed, which allows the parallel light from the tokamak to be focused on, and at another end, where the light is focused to the entrance slit of the spectrometer, the fibers are bundled linearly to match the entrance slit. (See Figure 4.3.) The hight of the entrance slit is fully open to collect abundant light. Two converging lenses are used for collimating and focusing, with

diameter of 1.0 and 0.5 inches respectively, and both of they have the $f/\#$ of 2.0. The optical fiber has the $f/\#$ of 2.4, and the spectrometer has the $f/\#$ of 7.0. The $f/\#$ is defined as

$$f/\# = \frac{\text{focal length}}{\text{diameter}} \tag{4.11}$$

Ideally, it is necessary to match the $f/\#$ number in all optical systems, which requires the $\mathrm{f_{input}}/\# > \mathrm{f_{output}}/\#$. This could ensure all of the light conveyed from the input optics can be collected by the output optics. Currently, the $f/\#$ number is not matched and some portion of light is lost.

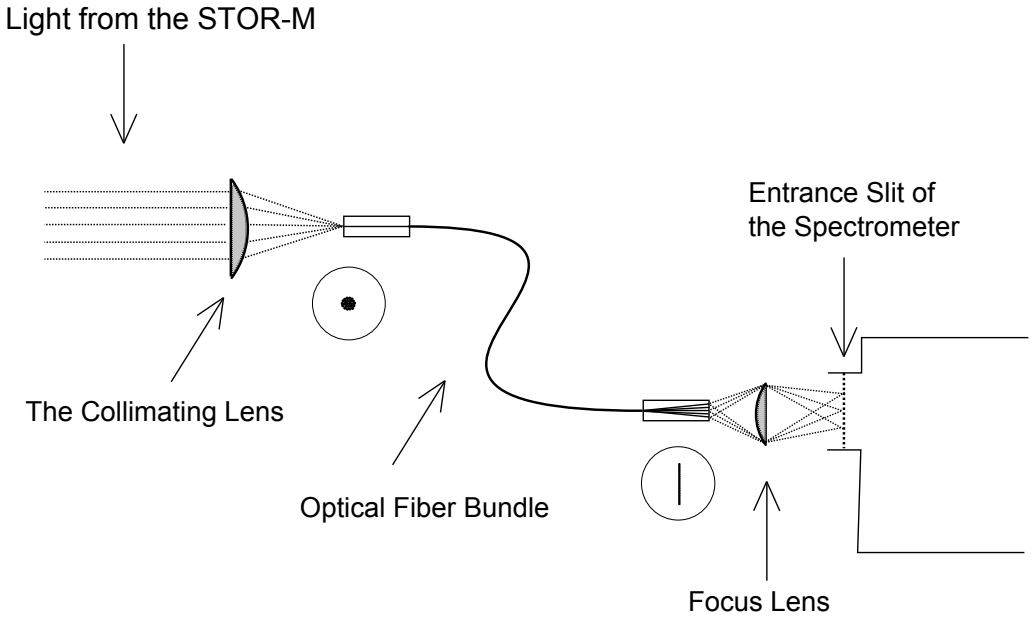

Figure 4.3: The side view of the light collection optics. Parallel light from the STOR-M tokamak is focused to the fiber optics and further focused on the entrance slit of the spectrometer.

4.4 The exit optics

At the exit of the spectrometer, a fused silica cylindrical rod lens is placed to magnify the spectrum in the dispersion direction. It has a short focal length, which results in a large magnification. The physical size of the lens is 3.14 mm in diameter and 30.0 mm in length. This lens is mounted on a stage assembly capable of translating in three dimensions and rotating around the optical axis of the spectrometer exit. The detailed information is shown in the Appendix A. The exit slit is removed

to accommodate for the cylindrical rod lens and the optical stages holding it. Since the thickness of the cylindrical rod lens is comparable to its radius, the cylindrical rod lens is considered as a thick lens and its focal length is given by the expression [34]:

$$\frac{1}{f} = (n-1)\left[\frac{1}{R_1} - \frac{1}{R_2} + \frac{(n-1)d}{nR_1R_2}\right] \tag{4.12}$$

where R_1 and R_2 are the curvature radii of the left and right surfaces of the lens, d is the lens thickness, and n is the index of refraction. For a cylindrical rod lens, the radius of both surfaces have the same magnitude as r, which is the radius of the cylinder, but they have different signs, and the lens thickness is equal the diameter of the cylinder, as

$$R_1 = r, R_2 = -r, d = 2r \tag{4.13}$$

Therefore, from Equation (4.12), one can derive the focal length of a cylindrical rod lens as

$$f = \frac{nr}{2(n-1)} \tag{4.14}$$

For the quartz lens used in the IDS system, the index of refraction is $n \approx 1.5$ in the visible range, therefore the focal length is f = 2.36 mm.

The imaging property of the lens is governed by the equation

$$\frac{1}{s_1} + \frac{1}{s_2} = \frac{1}{f} \tag{4.15}$$

where s_1 and s_2 are the object and image distances. Both of they are positive if the object and image are located in the corresponding sides. The magnification of the lens is

$$M = -\frac{s_2}{s_1} \tag{4.16}$$

If only the magnitude is considered, the magnification can be written as

$$M = \frac{s_2}{s_1} \tag{4.17}$$

Practically, during experiments, the position of the PMT is set at the beginning, then the position of the cylindrical lens is adjusted for focusing, which means, the total distance

$$s_t = s_1 + s_2 \tag{4.18}$$

is fixed before setting the objective and imaging distances s_1 and s_2.

The combination of the Equations (4.15) and (4.18) gives the expression of the objective and imaging distances, s_1 and s_2, in terms of the total distance s_t and focal length f

$$s_1 = \frac{s_t}{2} - \sqrt{\frac{s_t^2}{4} - f \cdot s_t} \tag{4.19}$$

$$s_2 = \frac{s_t}{2} + \sqrt{\frac{s_t^2}{4} - f \cdot s_t} \tag{4.20}$$

Therefore the magnification is

$$M = \frac{s_t}{2f} - 1 + \sqrt{\frac{s_t}{f}\left(\frac{s_t}{4f} - 1\right)} \tag{4.21}$$

For the spectrometer used in the STOR-M, $s_t = 150 \sim 500$ mm, $f = 2.36$ mm, and $s_t/f = 63.6 \sim 212 \gg 1$. The first order approximation gives

$$M \approx \frac{s_t}{f} = 63.6 \sim 212 \tag{4.22}$$

Thus, the linear dispersion is magnified, as

$$\left[\frac{dl}{d\lambda}\right]_{magnified} = M \cdot \left[\frac{dl}{d\lambda}\right]_{original} \tag{4.23}$$

The magnified spectrum is detected by a 16-channel photomultiplier tube array (Hamamastu Photonics, R5900U-07-L16). Photomultiplier tubes (PMT) are widely used as optical detectors attributed to its fast response and high sensitivity. It consists of photocathode, dynodes, and anode. Due to photoelectric effect, when a photon bombards the photocathode of the PMT tube, it can cause the emission of a photoelectron, which further generate secondary emission of electrons in the dynodes, and the anode captures the generated current.

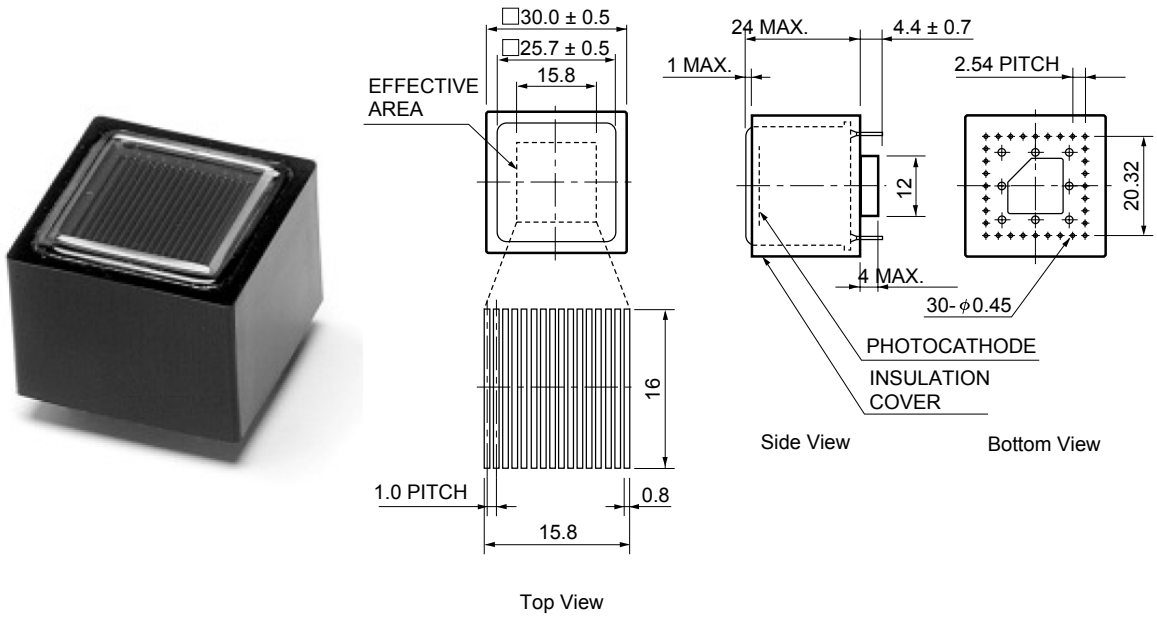

Figure 4.4: Picture and dimension parameters of the multi-anode PMT used in the IDS system (Unit: mm) [35].

The PMT array has an effective area of $15.8 \times 16\ \mathrm{mm}^2$, with the size of each channel of $0.8 \times 16\ \mathrm{mm}^2$, and the distance between channel to channel is 1mm, as shown in Figure 4.4. The PMT is able to detect the light of wavelength from 165 to 850 nm, with the peak wavelength 420 nm. The PMT is placed on a socket assembly E6736, which provides a DC voltage of -900 V and transfer the current signal. The cylindrical rod lens and the PMT are enclosed in a light-tight aluminum box, where the inner wall of the box is painted black to absorb stray light. 16 BNC feedthrough are embedded in the wall of the end side of the box. In the left side of the box, a door is built and a black sheave weaved with aluminum foil is attached to the outside of the door, to provide light shielding when adjusting the optical parts. Inside of the box, a 50 cm long triangular rail is used to mobilize the stages of both the lens and PMT. This allows the distance between the PMT surface and the imaging plane of the spectrometer s_t to be adjustable from 14.8 cm to 37.8 cm. (See Figure 4.6.)

The current signal from the PMT is converted to voltage signal by using a current-voltage preamplifier built on operational amplifiers OP467 from Analog Devices. The pick-up resistor is chosen to be $1\mathrm{M}\ \Omega$, and resistors of $50\ \Omega$ at the input and output terminals are used to match the $50\ \Omega$ impedance of the RG-174 coaxial cable. The capacitor coupled to the pick-up resistor is 100 pF, which in combination with the pick-up resistor works as a low-pass filter with the RC time

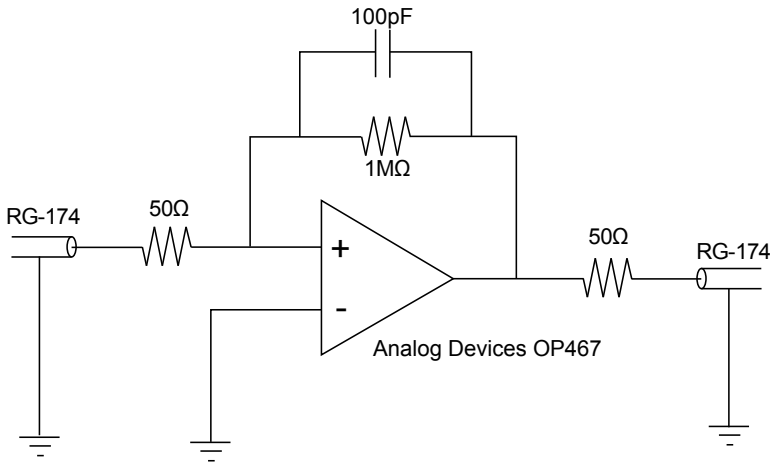

Figure 4.5: The I-V preamplifier consists of an operational amplifier, a pick-up resistor, as well as a coupling capacitor and impedance matching resistors.

resolution of $\tau_{RC} = 0.1\ \mu$s.

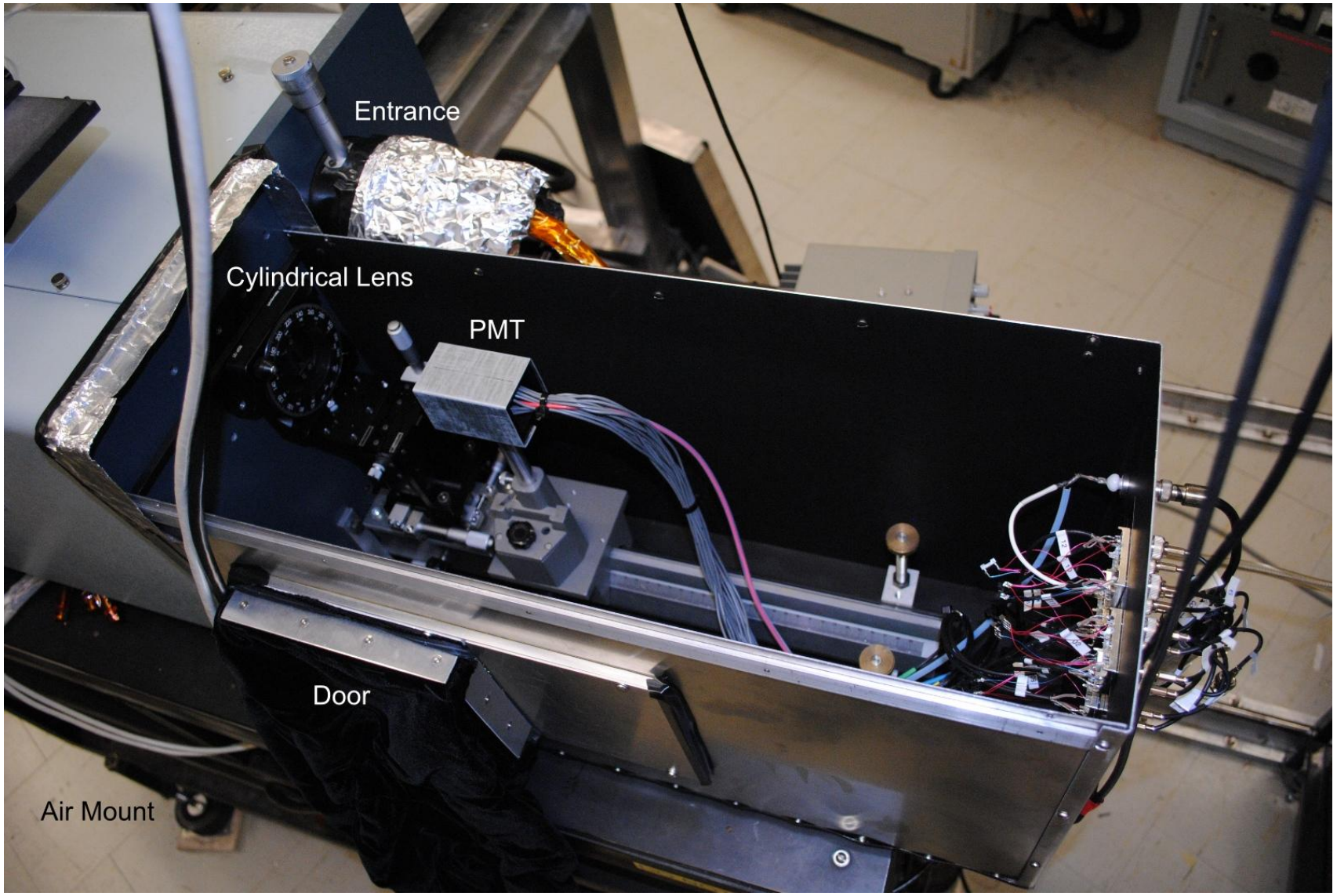

Figure 4.6: Picture of the output optics of the IDS system. The optical components are enclosed in a carefully sealed light-tight aluminum box. A door is made to the left wall for alignment and calibration. The legs of the bench is mechanically isolated by compact air mounts. (One is visible at the left bottom corner.)

4.5 System alignment

The IDS system was aligned before measurement. The first step is to level the bench and spectrometer by adjusting the height of the feet of each part. A He-Ne laser with the wavelength of 632.8 nm is used to illuminate the IDS system. The position of PMT is set by putting a white paper on its surface to enable the observation of the alignment light. The grating is turned manually to diffract the laser light on the PMT surface. At this moment, it is necessary to adjust the PMT vertically, and to further adjust the cylindrical lens along the optical axis direction as well as the angle along this axis, till a clear image appears on the PMT surface.

At this moment, a mercury calibration lamp (Oriel 6034) was used, the spectrometer grating was turned to the calibration wavelength (5460.7 Å), and the signal from Channel 9 of the PMT array was monitored. The position of the cylindrical lens was manually adjusted to maximize the light signal recorded by Channel 9 of the PMT, therefore this particular channel was centralized. The position of the input optical fiber was also adjusted, to ensure the largest incoming light.

At the initial test, fluctuation on the calibration signals was discovered during STOR-M discharges. It is corresponding to the mechanical shift of the light spot between the two channels. Compact air mounts (Newport SLM-3A and SLM-6A) are used to damp the mechanical vibration. The two SLM-3A air mounts are pumped to the pressure of 30 psi, and the SLM-6A is pumped to 60 psi. They are connected to the table feet by screws. (See Figure 4.6.)

4.6 System calibration

The IDS system is calibrated with the same mercury lamp as the one used in the alignment process. The spectrometer grating motor speed is set to 10 Å/min to scan increasingly over the wavelength of 5460.7 Å. As the spectrum of mercury lamp sweeping along the PMT surface, each channel of the PMT records a certain waveform. The peak value of each waveform corresponding to the relative sensitivity of the PMT channels, the wavelength difference of peak values is the linear dispersion at the PMT surface. The DC offset signal from each channel can also be measured during this process. Each waveform corresponding to the instrumental function of the spectrometer. At the present setup, the linear dispersion at the PMT surface is 0.20 Å/mm. (See Appendix B for linear

dispersion measurement with various wavelength.)

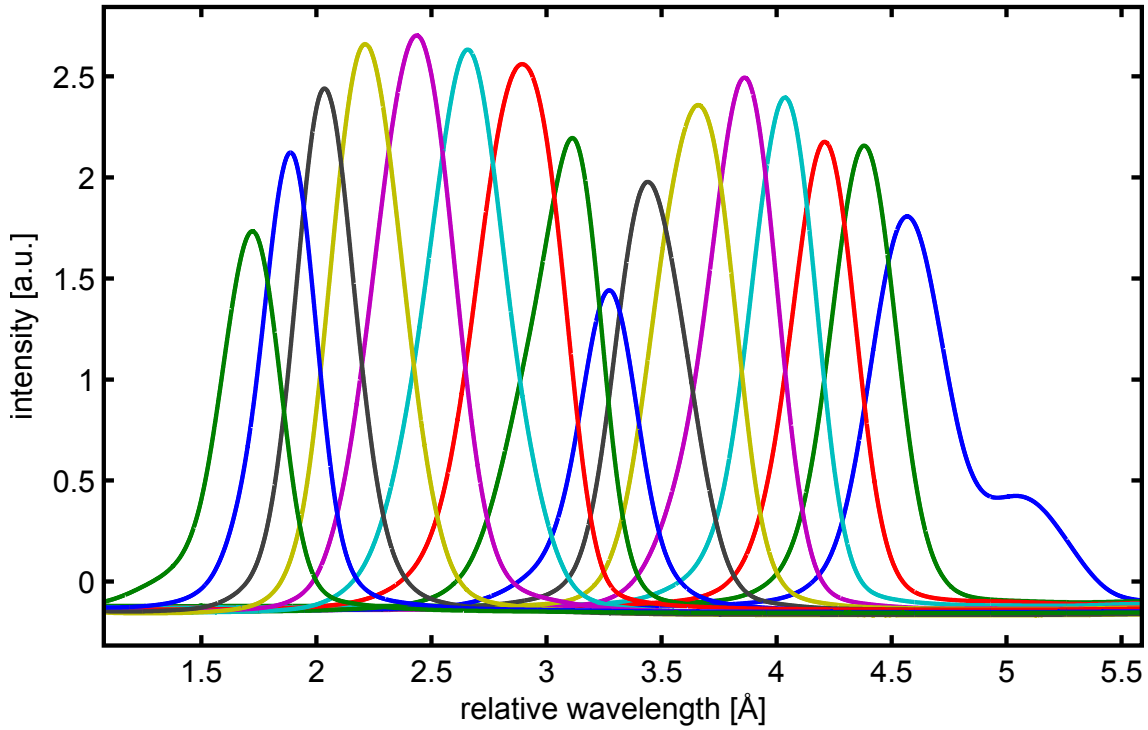

Figure 4.7: Waveform of calibration. Relative sensitivity, dispersion, instrumental width, and DC offset can be found in the waveform.

The relationship between the instrumental broadening width and the input slit width was investigated as shown in Figure 4.8. Obviously, the broadening is larger with larger input slit width. This test shows in the range of $10 \sim 100$ μm for input slit width, the instrumental broadening varies from 0.27 Å to 0.86 Å.

4.7 Data analysis methodology

The 16 channel voltage signals from the I-V preamplifier is conveyed to the data acquisition system (DAQ) by a 10-meter-long twisted-pairs with shielding. The DAQ is equipped with 14bit digitizers (National Instruments NI-6133). They have a sampling frequency up to 1 MHz. The digitizers are controlled by a LabVIEW program via a PC.

Signal from the IDS is recorded by the digitizer for 60ms and sampled at 1MHz after triggering. The original signal is binned to each 0.1 μs, which is equal to the RC time of the current amplifiers. The previous measured relative intensity and DC offset of different channels are used to correct the

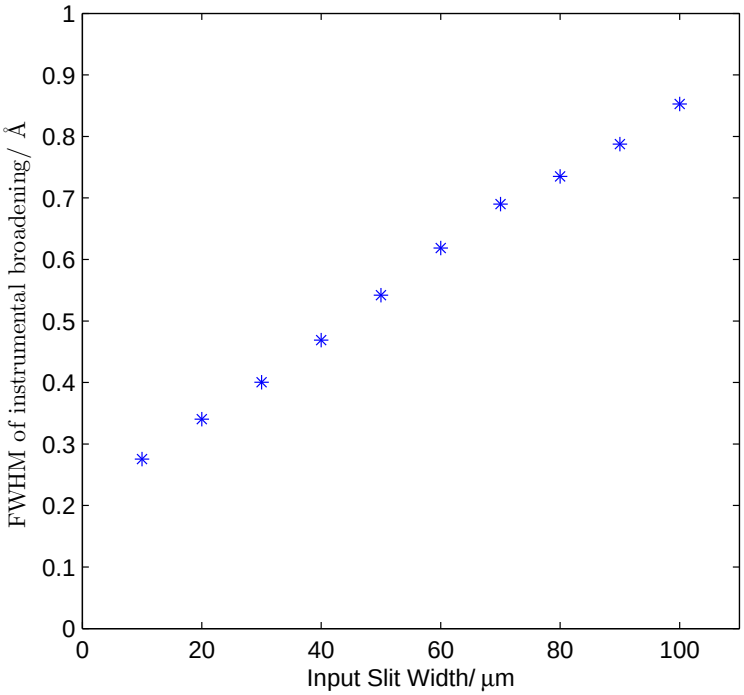

Figure 4.8: The instrumental broadening as a function of the input slit width.

signal of each channel. The processed voltage signals are fitted into Gaussian functions.

As described before, the measured signal $\{x_i, y_i, t\}$ $(i = 1 \sim 16)$ can be fitting into a Gaussian function, as

$$f(x_i) = Ae^{-\frac{(x_i-B)^2}{2C^2}} + D \tag{4.24}$$

where x_i is the wavelength of Channel i, y_i is the signal level of Channel i, $f(x_i)$ is the fitting function, and A, B, C, D are fitting parameters. The parameters A, B, C defines the amplitude, the centroid position, and the width of the Gaussian function. The last parameter D defines background signal such as hard x-ray, which can penetrate the metal shielding of the PMT.

The least square method is used to fit the function of Equation (4.24). Because of the nonlinearity of the this function, a numerical algorithm called gradient search method [36] is used for fitting. The basic principle is to minimize the quantity $\chi^2 = \Sigma(f(x_i) - y_i)^2$, which is a function of A, B,

C, and D. The initial values for calculation are listed below:

$$\begin{aligned} A_0 &= \max\{y_i\} - D_0 \\ B_0 &= i, \text{when } y_i = \max\{y_i\} \\ C_0 &= \sqrt{\frac{\Sigma y_i (x_i - B_0)^2}{\Sigma y_i}} \\ D_0 &= \text{average}\{y_1, y_2, y_{15}, y_{16}\} \end{aligned} \tag{4.25}$$

D_0 is the value averaged from the first two channels and last two channels of the PMT. A_0 is the difference between the maximum signal intensity and D_0, B_0 is the channel number which has the maximum value, and C_0 is a quantity defining the width of the curve. From the initial values, it is possible to calculate the gradient of χ^2 in the $\{A, B, C, D\}$ space. If the magnitude of the gradient is larger than zero (in the algorithm it is defined by a small number ϵ), the values of A, B, C, and D are changed to smaller ones along the gradient of each direction. The step size h is initially defined and it is reduced over time to avoid inconvergence. Figure 4.9 shows the fitting process.

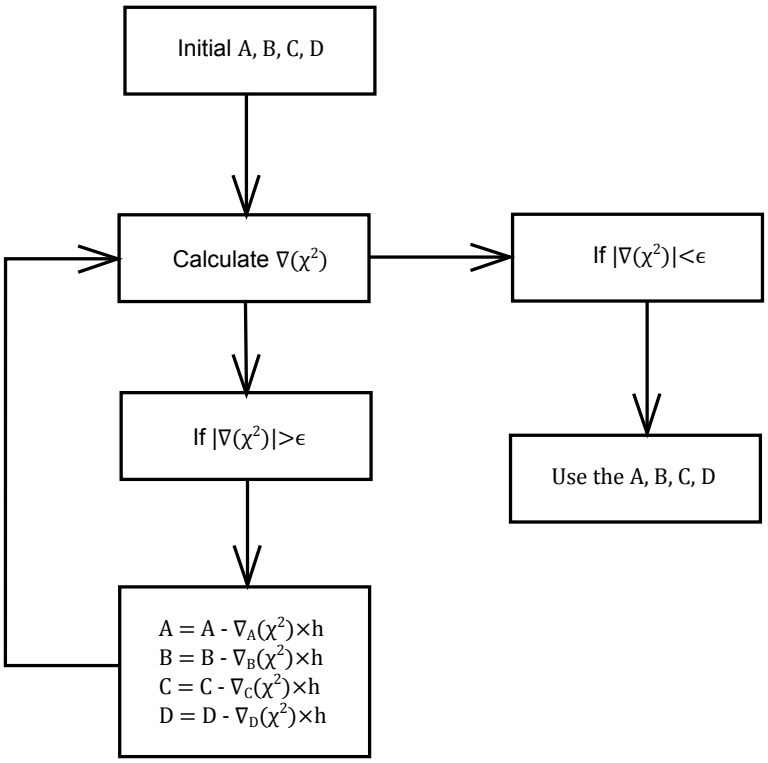

Figure 4.9: The flowchart of the Gaussian fitting algorithm.

The algorithm for data fitting is programmed in M.S. Visual C++ 2008. The main code is attached in Appendix C. A typical curve fitting is shown in the Figure 4.10. It can be seen the data is well fitted to a Gaussian function.

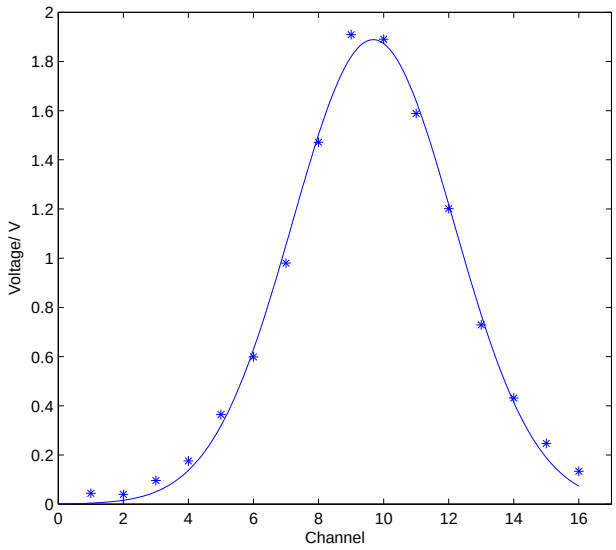

Figure 4.10: Gaussian fitting for $\mathrm{C_{III}}$ during an Ohmic heating discharge.

4.8 Error analysis

The error level of flow measurement is directly related to the uncertainty of the centroid of the Gaussian fitting peak, which depends on the s/n ratio of the spectrometer. Because of the using of a multichannel detector, the error from the fitting function is smaller than the FWHM of measured by a single channel. This phenomenon has also been reported in another spectroscopic system [37].

On the STOR-M, the error of flow measurement from the IDS system is about $\pm 1 \sim 2\mathrm{km/s}$, measured from the velocity fluctuation from the normal port. For example, the normal and tangential velocities of $\mathrm{C_{III}}$ flow are shown in Figure 4.11. The unshifted wavelength is measured by the average of multiple spectra from the normal port, and the velocity fluctuation from both a single shot and multiple shots is less than $\pm 2\mathrm{km/s}$.

Another source of error is the angle between the observation line of sight and the emission area, as shown in Figure 4.12. A factor of $1/\cos\beta$ should be multiplied on the velocity. This angle also

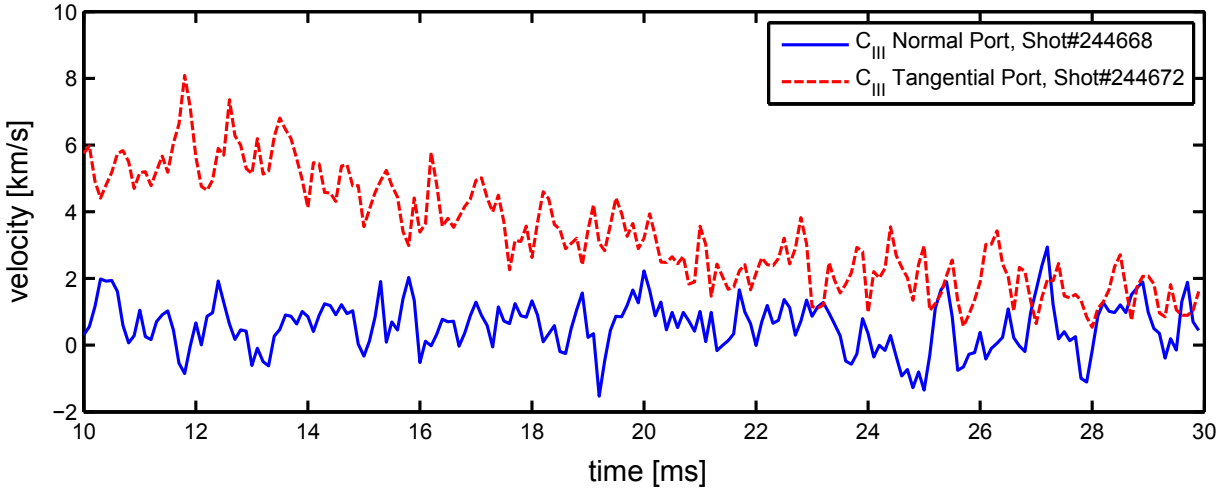

Figure 4.11: The C_{III} velocity measured from two ports.

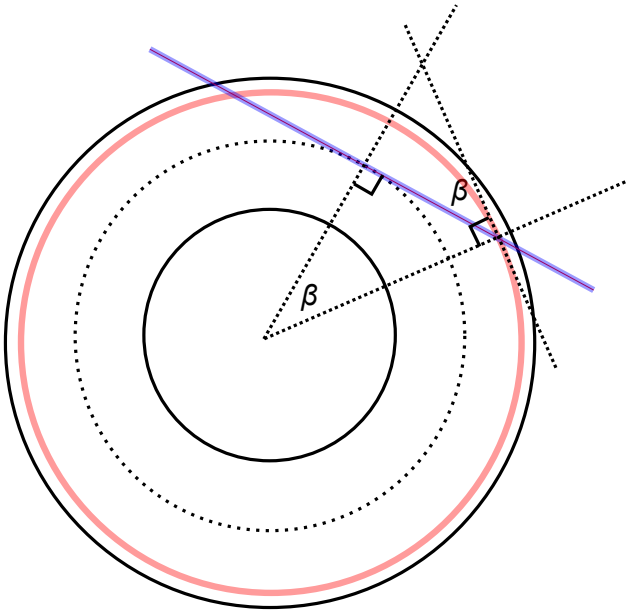

Figure 4.12: The β angle for velocity amendment.

equal to the angle between normal line and the line across the point of intersection. Therefore, β can be expressed as

$$\cos\beta = \frac{R_0}{R_0 + r} \tag{4.26}$$

In the STOR-M tokamak, $R_0 = 46\text{cm}$, the peak location r for C_{VI}, O_V, C_{III} and are found to be 0 cm, 3 cm, and 7 cm, corresponding to the $1/\cos\beta$ factor of 1.00, 1.07, and 1.15, which can be applied to the velocity results for amendment.

Chapter 5

Pre-measurement processes

5.1 Introduction

Before the flow measurement, several preparation steps are necessary. The emission lines need to be identified; the emissivity radial profile of those emission lines are also measured by placing the fiber optical head on the oval port and scanning on a shot-by-shot basis; the directions of the ion Doppler spectrometer and the tokamak are defined so that counter-clockwise (seen from top) is positive and clockwise is negative.

5.2 Emission line identification

The STOR-M tokamak utilizes hydrogen as the major gas. The strongest emission lines from hydrogen are the Balmer series, denoted as H_α, H_β, H_γ, etc. These lines are emitted through electron transition from higher energy levels to the second energy level of the hydrogen atom. Since the atoms are not subject to the magnetic and electric fields of the tokamak, the observation of these lines can not reveal the flow velocity nor temperature information of the hydrogen ions. Also, the hydrogen ion H^+ can not emit light through electron transition due to the lack of electron, and the hydrogen atoms are mostly at the edge of the tokamak, rather than the core region. Therefore, it is necessary to measure the spectra of impurity ions, rather than hydrogen atoms. Previous experiments show the existence of carbon and oxygen lines in the STOR-M tokamak [26, 38]. More lines are used in other fusion devices. To investigate the presence of impurity lines in the

STOR-M tokamak, an impurity gas puffing system was set up for additional impurity injection.

5.2.1 Previous spectroscopic measurement in the STOR-M and other fusion devices

Several carbon and oxygen spectral lines have been identified in the previous spectroscopic measurements in the STOR-M tokamak. They are $\mathrm{O_{II}}(4414.9\text{Å})$, $\mathrm{O_{III}}(3759.9\text{Å})$, $\mathrm{C_{III}}(4647.4\text{Å})$, and $\mathrm{C_{IV}}(4658.3\text{Å})$. These impurity lines were monitored in the turbulent heating [38] and electrode biasing [26] experiments. However, these lines have similar ionization levels. In order to have separate locations in the tokamak chamber, more discrete lines are needed, especially higher ionization orders are needed.

In other fusion devices, various emission lines are used for flow measurement. The most common ones are from carbon and oxygen ions, with different ionization levels. However, the emission lines from inert gases, such as helium, are also used. In the Table 5.1, an incomplete list of emission lines is presented.

Emission Lines	Sources of literatures
$\mathrm{He_I}$(3888.7Å)	[15]
$\mathrm{He_{II}}$(4685.7Å)	[15] ,[16], [39]
$\mathrm{C_{III}}$(2296.9Å)	[12], [37],[40]
$\mathrm{C_{III}}$(4647.4Å)	[11], [15]
$\mathrm{C_V}$(2270.9Å)	[37], [41], [42], [43]
$\mathrm{C_{VI}}$(3434Å)	[31]
$\mathrm{C_{VI}}$(5290.5Å)	[11], [44], [45],
$\mathrm{N_{II}}$(5680Å)	[46]
$\mathrm{O_{II}}$(4649Å)	[47]
$\mathrm{O_V}$(2781.0Å)	[48]
$\mathrm{O_V}$(6500.2Å)	[49]

Table 5.1: Incomplete list of emission lines used in fusion devices.

Besides the impurity lines in Table 5.1, the NIST database [50] also provides a reference. However, the NIST database has too many lines for the same ion species. It is impractical to check those

lines one by one. For the STOR-M tokamak, the impurity emission lines from both the literature sources and NIST database are examined, with additional impurity gas puffing system.

5.2.2 Impurity gas injection system and identified emission lines

In order to enhance the impurity emission, an additional impurity gas injection system was built and connect to the STOR-M tokamak. It consists of a 5L stainless steel gas tank, additional tubes and valves, as shown in Figure 5.1. Impurity gases such as methane, helium and argon are injected into the tokamak via this system. The system is operated as follows:

a) At the beginning, the gas tank is connected to the gas flow controller by the connector C1, and purged by a turbo-molecular pump (not shown in the diagram) to a vacuum of $\sim 5 \times 10^{-6}$ Torr connected from connector C2, with valves V1, V2, and V3 open. Then V2 is closed and the gas flow controller is set to 10$\sim$100 cc/min for 3 $\sim$ 30 minutes, and the gas tank is therefore filled with the impurity gas of ~ 5 mTorr.

b) The valves V1, V2, and V3 are closed, and the gas tank is disconnected from the gas cylinder and pump from connectors C1 and C2 respectively. Then the connector C1 is blanked in the tank side, and the tank is connected to the tokamak by connector C2. Since during the process of moving the gas tank, the tubes section between the valve V1, connector C1, and valve V3 is exposed to the atmosphere, it is necessary to pump out the residual gas before operation.

c) The pumping process is performed by opening the valves V3, V4, and V5 to pump out the residual gas through the tokamak pumping system, while the valve V1 valve is still closed to keep the impurity gas. During tokamak operation, the valve V1 is open, V4 is set to open a duration of 8 ms controlled by an electric pulse, and valves V2 and V5 are carefully adjusted to that during each pulse, the tokamak vessel can be filled to $\sim 5 \times 10^{-5}$ Torr with impurity gas before discharge.

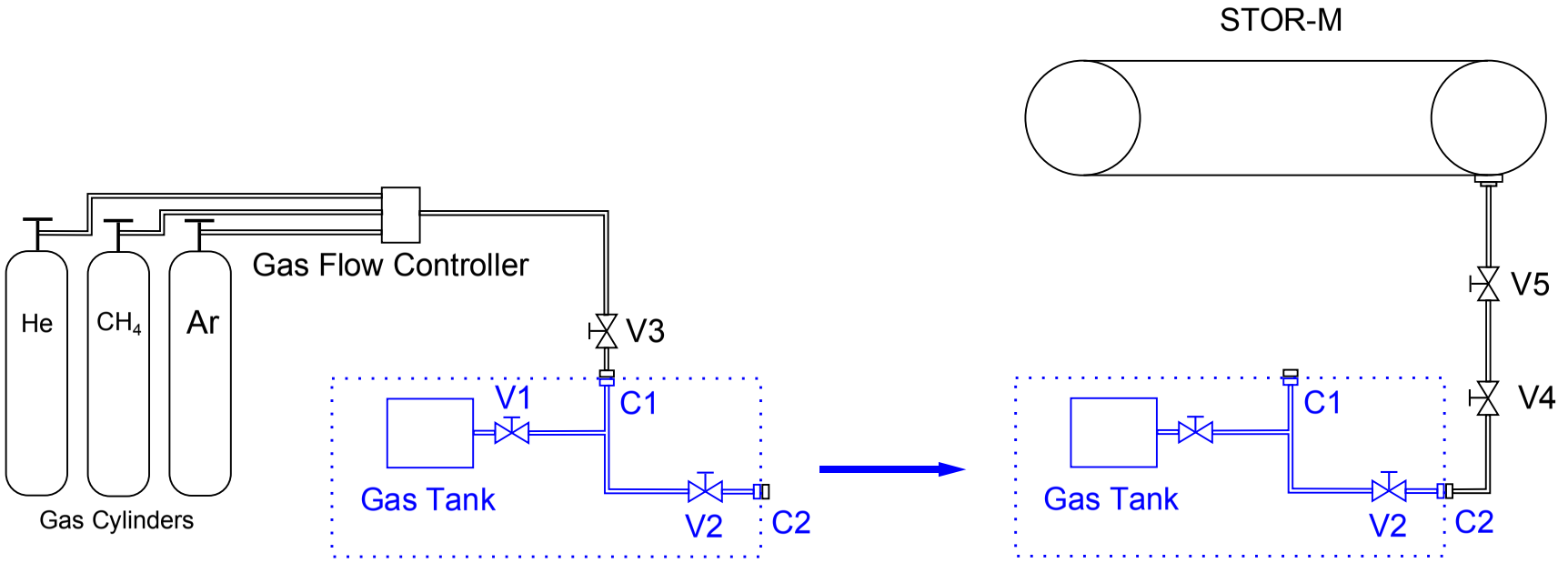

Figure 5.1: The schematic diagram of gas puffing. The V1 to V5 are gas valves, and C1 and C2 are connectors. The parts enclosed in the dashed box is movable.

At the first stage of emission line identification, a fiber optical spectrometer (Ocean Optics Spec2000) is used for full spectrum measurement ($200 \sim 960$ nm). A typical spectrum is shown in Figure 5.2. However, the resolution of this spectrometer (3 Å) is too low to identify impurity lines except the lines from hydrogen atoms.

Instead, the ion Doppler spectrometer was used for emission line identification, with a measurement range of 3.2 Å (each PMT channel covers 0.2 Å). The spectrometer is tuned to the possible emission line wavelengths listed in Table 5.1 and from the NIST database. It can only observe one line during each shot, thus the whole process took hundreds of tokamak discharges. Finally, various emission lines of hydrogen, carbon, and oxygen are identified, as shown in the Table 5.2.

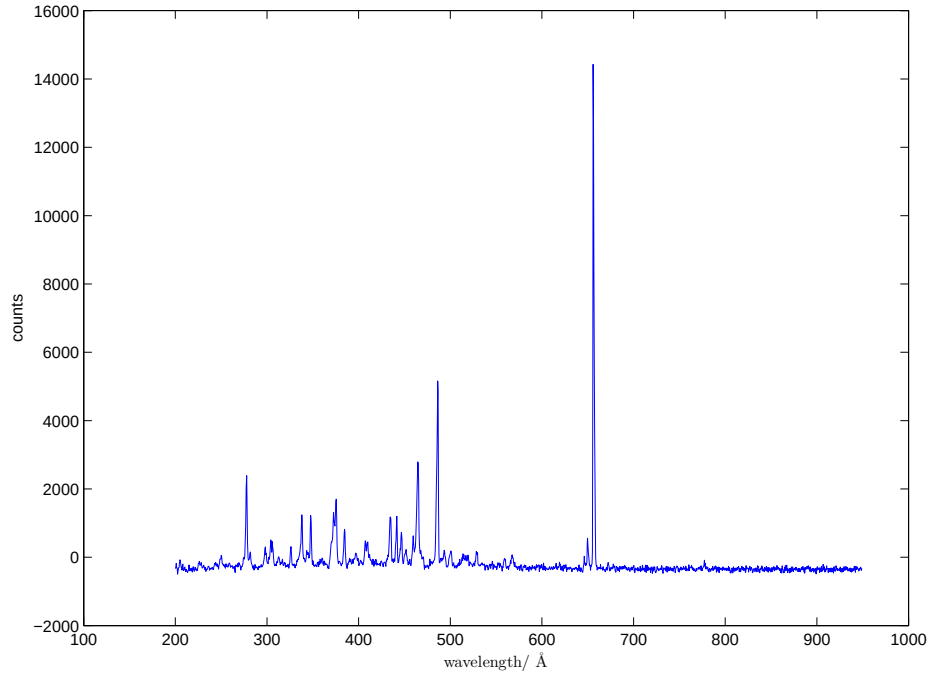

Figure 5.2: The spectrum measured from the fiber optical spectrometer (Ocean Optics Spec2000).

However, not all of these lines are suitable for measurement. Hydrogen lines, as explained earlier, can not be used for flow measurement. Even for carbon and oxygen lines, not all of them can be used for flow measurement. When the additional methane puff was turned off, some carbon lines became weak for measurement. The emission lines in the U.V. range also have weak signals, because of the spectrometer is not sensitive enough in this range. The emission lines with small wavelength difference should also be eliminated, such as $\mathrm{O_{II}}(4649.1$ Å$)$ and $\mathrm{C_{III}}(4650.3$ Å$)$, to

Emission Lines	Wavelengths	Electron Configurations
H_α	6562.8 Å	$2-3$
H_β	4861.4 Å	$2-4$
H_γ	4340.7 Å	$2-5$
C_{III}	4647.4 Å	$1s^2 2s3s - 1s^2 2s3p$
C_{III}	4650.3 Å	$1s^2 2s3s - 1s^2 2s3p$
C_{IV}	4658.3 Å	unknown
C_V	4944.6 Å	unknown
C_{VI}	5290.5 Å	unknown
O_{II}	4349.4 Å	unknown
O_{II}	4414.9 Å	$2s^2 2p^2(^3P)3s - 2s^2 2p^2(^3P)3p$
O_{II}	4649.1 Å	$2s^2 2p^2(^3P)3s - 2s^2 2p^2(^3P)3p$
O_{III}	3759.9 Å	$2s^2 2p(^2P^\circ)3s - 2s^2 2p(^2P^\circ)3p$
O_{IV}	3736.9 Å	$2s2p(^3P^\circ)3p - 2s2p(^3P^\circ)3d$
O_V	2781.0 Å	$1s^2 2s3s - 1s^2 2s3p$
O_V	6500.2 Å	$3p^3D_3 - 3d^3F_4$

Table 5.2: Major emission lines observed in the STOR-M tokamak.

avoid ambiguity.

Another concern is the impurity emission lines from iron (Fe). Since the tokamak has a stainless steel vacuum chamber and a stainless steel limiter, it is possible that the spectrum is contaminated by iron lines. However, the ion lines can be distinguished from other emission lines based on their radial location. The singly charged iron lines should appear at the very edge of the tokamak, while the carbon and oxygen lines appear at the center of the tokamak. This is confirmed in the radial profile measurement in the next section.

For the Doppler flow measurement in the STOR-M tokamak, three emission lines ($C_{III}(4647.4\,\text{Å})$, $O_V(6500.2\,\text{Å})$ and $C_{VI}(5290.5\,\text{Å})$) are selected. They are relatively stronger than other emission lines listed on Table 5.1, and also have different ionization stages. It is also found that without additional impurity injections, these emission lines possess a reasonable signal level for flow measurement.

Figure 5.3 shows the time evolution of line emission intensity of these three lines. From this graph, it can be observed that the C_{III} arrives its peak earlier than other two lines, and then reduces

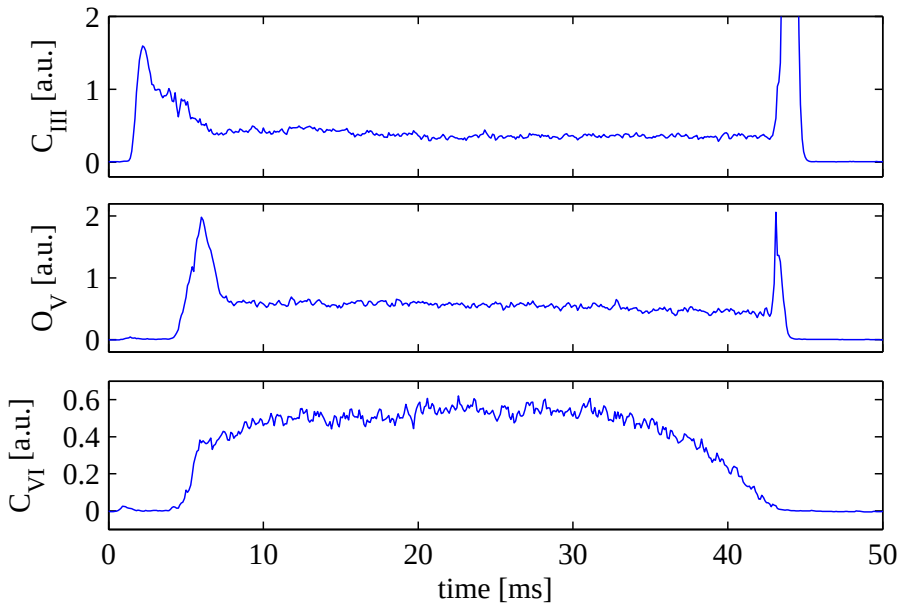

Figure 5.3: The emission lines intensity of C_{III}, O_V and C_{VI} ions during Ohmic heating discharges.

to a constant level during the current flat-top period. O_V reveals the similar property, however, its signal peak arrives later than that of C_{III}. The C_{VI} line has a very different time evolution profile comparing to other two lines. It achieves maximum during the current flat top period. These three graphs reveals that the ionization stages of the emission lines are reasonable because the lower ionization (lower electron temperature) ions shows up earlier than higher ionization (higher electron temperature) ions during discharges, corresponding to the increase of electron temperature over time during plasma discharges.

5.3 Radial profile measurement

The radial profile of certain emission lines are measured through the oval port. Its cross-section is shown in the Figure 5.4. The spectrum lines are measured shot-to-shot at different positions

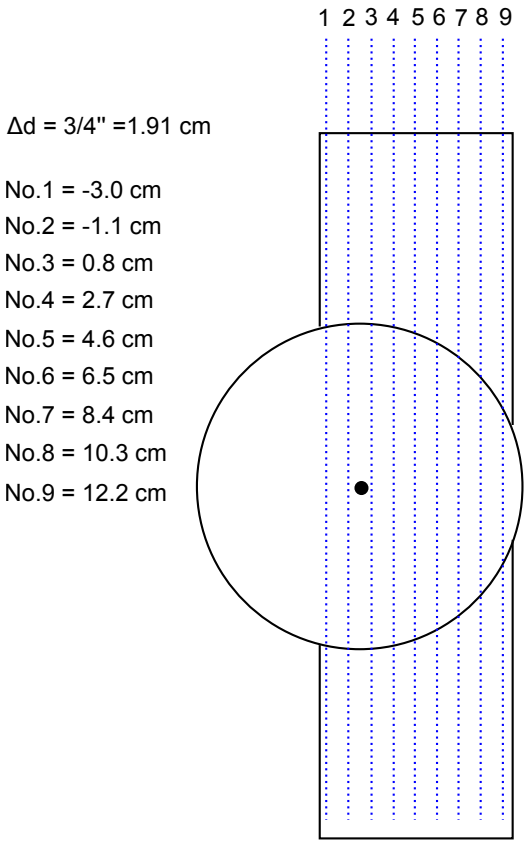

Figure 5.4: The schematic diagram of radial profile measurement in STOR-M tokamak

during a series of similar discharges. The optical fiber observes the plasma emission vertically and in parallel. The distance between neighboring observation points is 1.91cm (3/4 inch). The line integrated signals of emission lines $\mathrm{C_{III}}(4647.4\ \text{Å})$, $\mathrm{O_V}(6500.2\ \text{Å})$ and $\mathrm{C_{VI}}(5290.5\ \text{Å})$ are measured and shown in Figure 5.6.

The original profile Figure 5.6 is smoothed and inversed to produce the local emissivity versus radial distance. As shown in Figure 5.5, the whole circle is divided to several layers (seven layers are shown in the figure), and the emissivity of each layer is assumed to be a constant number. The distance of each line of sight travels can be calculated geometrically, denoted as $d_{l,m}$. Therefore, from the outermost line of sight, the emissivity of the outermost layer E_n can be calculated from the line integrated signal S_n, as

$$E_n = \frac{S_n}{d_{n,1}} \tag{5.1}$$

The second outermost line of sight goes through two layers (the outermost and second outermost). Since the outermost layer emissivity is already calculated by the outermost line of sight signal

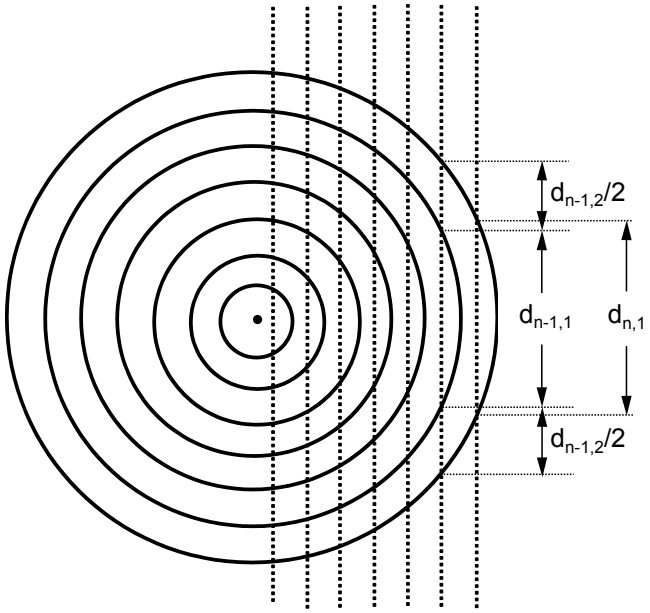

Figure 5.5: Inversion method

strength, it can be subtracted from the second outermost line integrated signal, and the second outermost layer emissivity can be calculated.

$$E_{n-1} = \frac{S_{n-1} - d_{n-1,2} \times E_n}{d_{n,1}} \tag{5.2}$$

Therefore, layer by layer, the local emissivity of each layer can be calculated. The local emissivity profile is shown in Figure 5.7.

From this profile, it can be seen that, the $\mathrm{C_{III}}$ emission line is peaked at $r = 7\ \mathrm{cm}$, $\mathrm{O_V}$ is peaked at $r = 3\ \mathrm{cm}$, while $\mathrm{C_{VI}}$ is peaked at the chamber center. The $\mathrm{C_{III}}$ line is at the edge region, $\mathrm{C_{VI}}$ at the core region, and $\mathrm{O_V}$ is located between them. This is understandable because usually tokamak has higher electron temperature in the center than the edge, thus higher electron temperature can ionize the impurity ions to higher stages.

5.4 Definition of plasma flow direction

It is important to have a consistent definition of plasma flow through all measurements. In this thesis, counter-clockwise direction is defined as positive flow direction, while clockwise direction is negative.

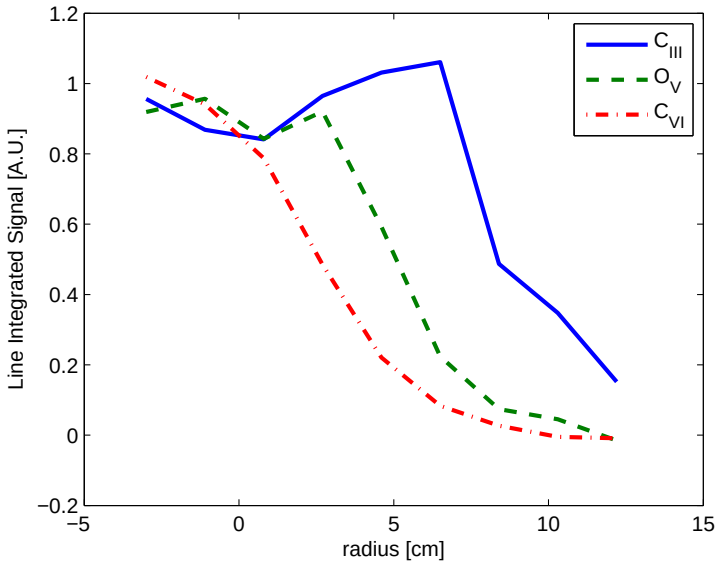

Figure 5.6: Line integrated signals of C_{III}, O_V and C_{VI} emission lines.

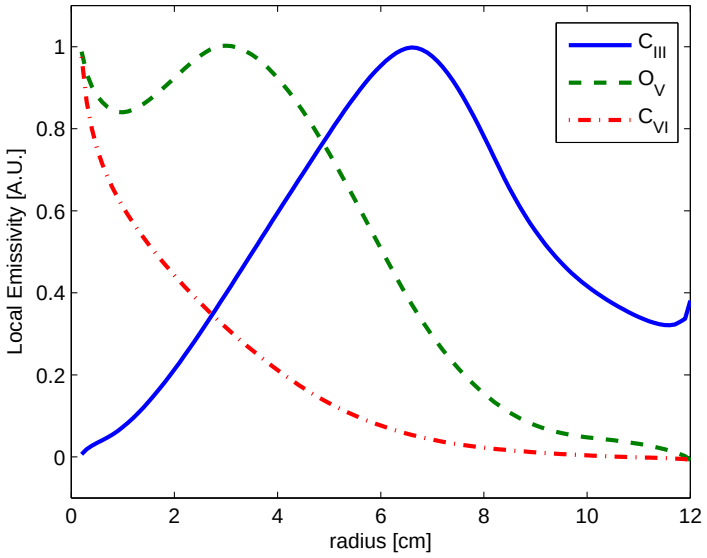

Figure 5.7: Profile of C_{III}, O_V and C_{VI} emission lines.

Figure 5.8 shows the top-view of the tokamak: in the normal operation, the plasma current I_p is in the counter-clockwise direction, while the toroidal magnetic field B_T is in the clockwise direction; in the reversed current operation mode, the plasma current is in the clockwise direction, same as the toroidal magnetic filed B_T direction.

The configuration of the spectrometer is also shown here. The grating is tilted to the left-side, which results that both the incident and diffraction light in the right-side of the grating normal.

The shorter wavelength is diffracted to smaller angle (left) while longer wavelength to larger angle (right). The cylindrical rod lens reverses the relative positions of spectrum the shorter and longer wavelength, and the PMT is arranged that the left side has higher channel numbers. Therefore, the higher channel numbers of the PMT records longer wavelengths of the spectrum. Since the longer wavelength shift - redshift - is caused by the ions moving away from the observer, which is also the plasma current direction, the increase of the PMT channel number shift corresponds to the counter-clockwise direction.

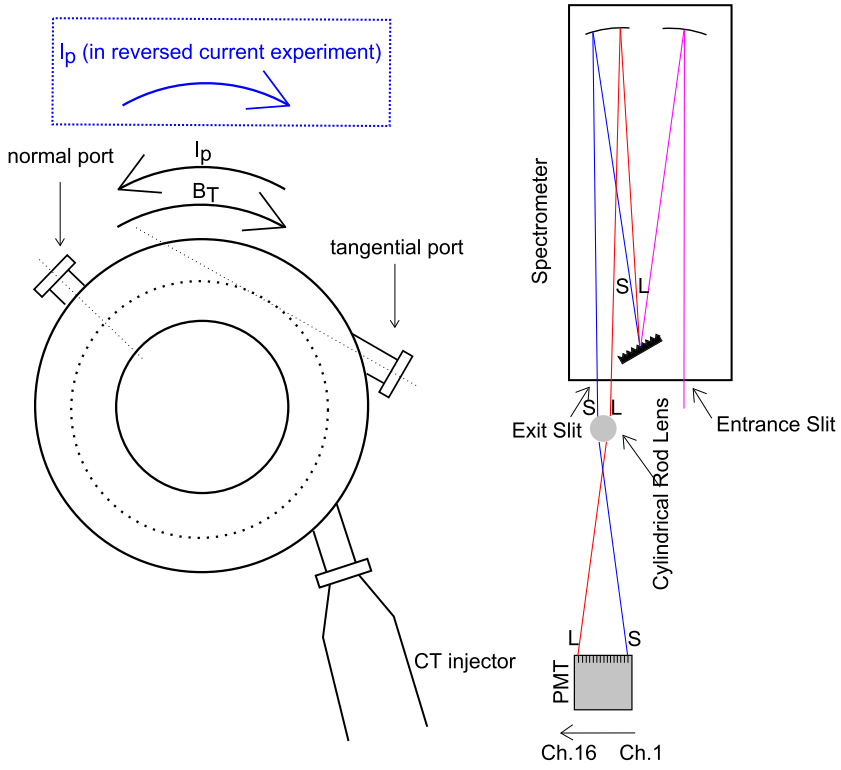

Figure 5.8: The directions of the STOR-M tokamak. The plasma current I_p is in the counter-clockwise direction, and the toroidal magnetic field B_T is in the clockwise direction. For the IDS system, the larger channel number records the longer wavelength.

Chapter 6

Toroidal flow measurement in various operation modes

6.1 Normal Ohmic discharges

In STOR-M, hydrogen plasma is initiated and maintained by applying a toroidal electric field which drives a toroidal plasma current. Ohmic heating discharges without manipulation can only generate low confinement mode (L-mode). It is usually used for machine conditioning and equipment testing. Such discharges are denoted as normal Ohmic discharges in this thesis.

The plasma parameters of a typical normal Ohmic discharge are shown in Figure 6.1. The plasma current can exceed 20 kA, and the loop voltage is lower than 3 V in the current flat-top period. Higher plasma current and lower loop voltage indicates a lower resistivity and higher electron temperature. During operation, hydrogen gas at the pressure of $0.5 \sim 1 \times 10^{-4}$ Torr is constantly fed to the tokamak chamber. The quality of plasma is highly sensitive to the base pressure. Lower pressure can induce easier break down, but also produce excessive run-away electrons. They can cause damage to the chamber wall, and also generate unwanted hard x-ray. Higher base pressure can reduce the run-away electrons but degrade the plasma quality. So, there is a balance between plasma operation and hard x-ray reduction.

The plasma flow velocity is measured from the Doppler shifted wavelength of optical lines emitted by ions. Before measurement, the tokamak is usually operated for a few hours for the purpose of discharge cleaning. Once the plasma becomes stable, the IDS system is set to the wavelength of target emission line. The light emitted through the normal port is observed for a few

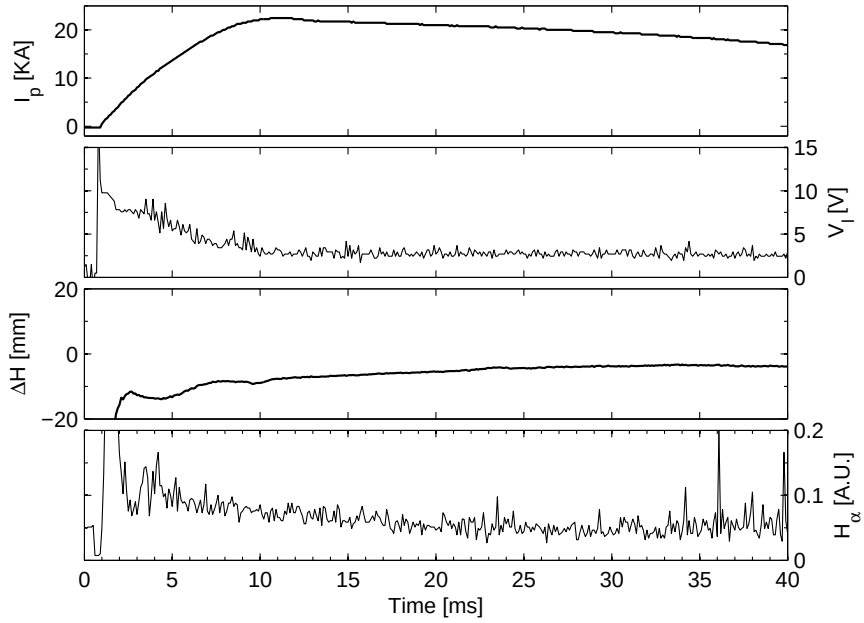

Figure 6.1: Plasma Parameters (Plasma Current, Loop Voltage, Plasma Position, and H_α emission) of a typical shot #244672.

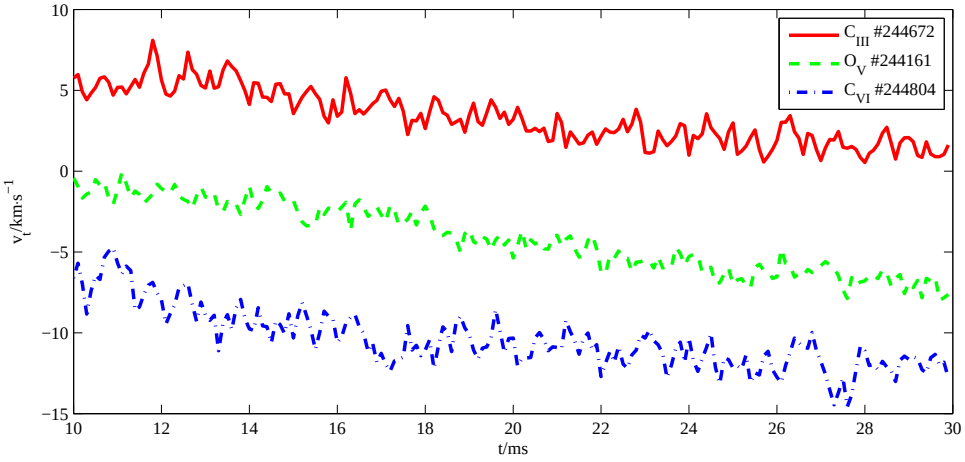

Figure 6.2: Ohmic heating discharge flow results. Positive value on the flow indicates counter-clockwise (co-current) direction, while the negative is clockwise (anti-current) direction.

shots as the reference wavelength, and the one through the tangential port is used for toroidal flow measurement. The velocity error level is found to be about $\pm 1 \sim 2$ km/s, with the time resolution of 0.1 ms.

The toroidal flow velocities of C_{III}, O_V and C_{VI} ions are shown in the Figure 6.2. They exhibit a difference on the magnitude and also direction. C_{III} flow velocity at the periphery is in the

counter-clockwise direction (co-current), while the O_V and C_{VI} flow velocities are in the clockwise (anti-current) direction. During the current flat-top period (10 - 30 ms), all of the three ion species exhibit flow velocity change towards to the clockwise direction at the similar rate. The C_{III} flow decreases from $+6$ km/s to 1 km/s, the O_V flow decreases from -1 km/s to -8 km/s, and C_{VI} flow decreases from -6 km/s to -12 km/s. Since the previous profile measurement in Chapter 5 shows C_{III} ions are concentrated at $r = 7$ cm, O_V ions are near the position $r = 3$ cm, and C_{VI} ions are mainly from the plasma core region, the flow shear of impurity ions is also position-dependent.

The phenomenon of flow velocity change from the periphery to the core has also been observed on other tokamaks [10, 51]. In those experiments, the ions in the edge regions flow in same direction as plasma current, and the central ions flow opposite to the plasma current.

Previous flow measurement on STOR-M with G-probe shows the plasma is rotating at a constant co-current speed approximately 15km/s in the region from r = 10.0 cm to r = 13.5 cm, which is in the same direction of C_{III} flow velocity, but they have different magnitudes [27]. The G-probe flow is three times larger than the C_{III} flow. It may be because of different locations, but also may caused by the difference between major ion H^+ and C_{III}, since they have different mass and electric charge.

The toroidal plasma flow measured by a four-sided Mach probe is similar to the G-probe results, indicating a Mach number of 0.5 (1 Mach corresponding to 30km/s) in the toroidal direction, in the region between r = 10 cm to r = 15 cm [26].

6.2 Reversed current operation

The toroidal plasma current in the tokamak not only provides Ohmic heating, it also creates the poloidal magnetic field, and the reversal of plasma current direction leads to the reversal of poloidal magnetic field. According to Equation (3.9), the toroidal flow is inversely proportional to the poloidal magnetic field. Therefore, it is expected that the toroidal flow will be reversed when the plasma current is reversed.

In the STOR-M tokamak, the direction of the plasma current can be reversed by interchanging the connectors of the ohmic heating coils. However, the plasma position detection and feedback control systems are intimately related to the plasma current direction. With reversed current, the

"set point", defining the zero plasma position, and the feedback control signals should be readjusted. The complete process took a few days with more than 500 discharges before the plasma became stable. The plasma parameters of the reversed current experiment is similar to the Normal Ohmic discharges, except the current direction is opposite, as shown in Figure 6.3.

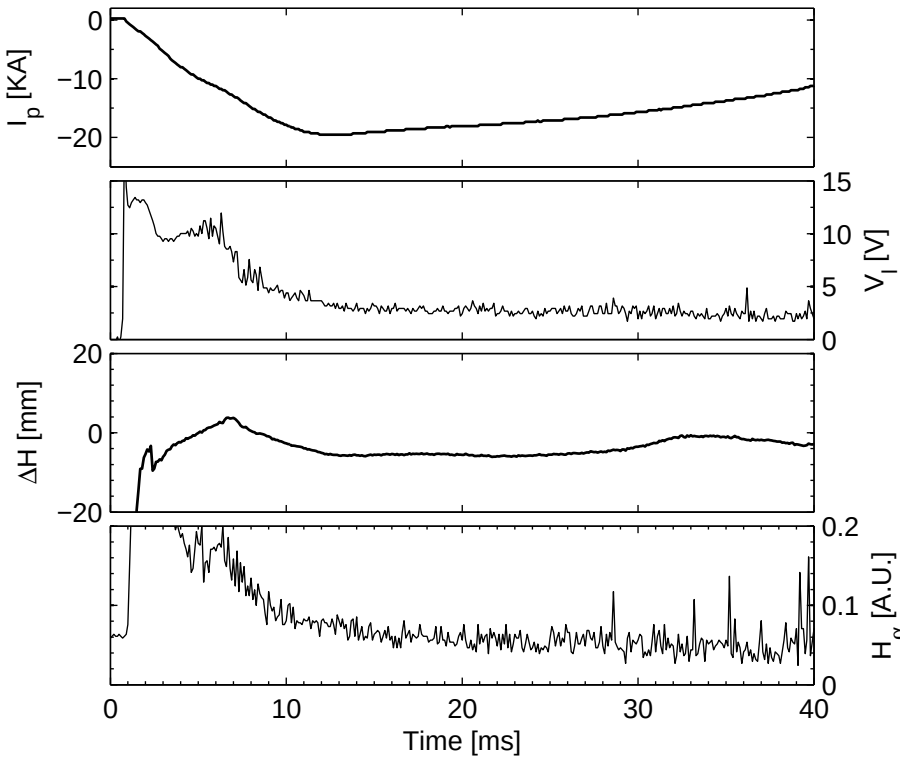

Figure 6.3: Plasma Parameters (Plasma Current, Loop Voltage, Plasma Position, and H_α emission) of a typical shot $\#245742$ with reversed current experiment.

The impurity flows are measured in the same procedures of normal Ohmic discharges. Toroidal velocities of $\mathrm{C_{III}}$, $\mathrm{O_V}$ and $\mathrm{C_{VI}}$ ions are displayed in Figure 6.4. As expected, with reversed plasma current, the flow directions are also reversed, but the magnitude of these velocities are different from those in the normal discharges. During the current flat-top time between 10 and 30 ms, the velocity of $\mathrm{C_{III}}$ decreases from 0 km/s to -2 km/s, $\mathrm{O_V}$ velocity remains at the level of 5 km/s, and the flow velocity of $\mathrm{C_{VI}}$ increases from 8 km/s to 13 km/s at 18 ms, and then drops back to 10 km/s at 30 ms. The absolute values of the toroidal flow velocities are not exactly the same as the normal Ohmic discharges. Flow shear was observed and the relative flow differences (between $\mathrm{C_{III}}$ and $\mathrm{O_V}$, and between $\mathrm{O_V}$ and $\mathrm{C_{VI}}$) are similar to the ones with normal discharge current direction

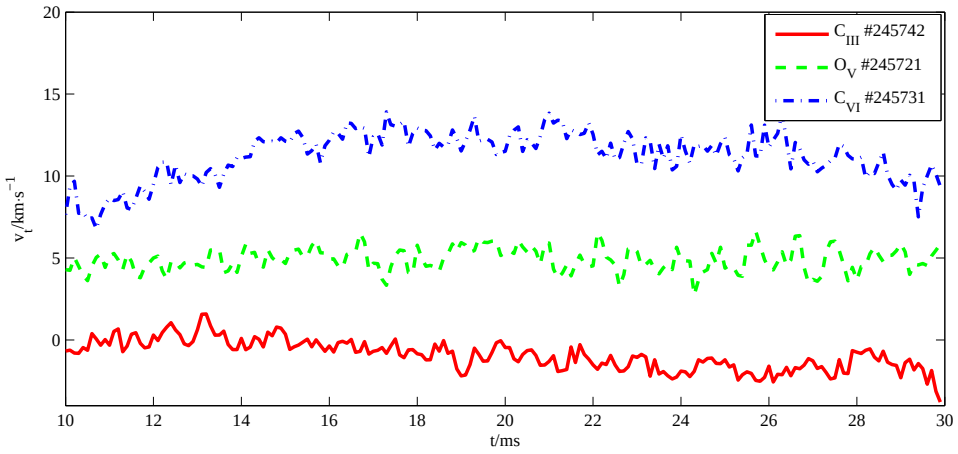

Figure 6.4: Reversed current flow results. Positive value on the flow indicates counter-clockwise direction, while the negative is clockwise direction.

($\sim 5\ \mathrm{km/s}$). However, the flow velocities of the impurity ions in the reversed current discharges do not show a consistent increase or decrease over time, which is different from the flow velocities in the normal Ohmic discharges.

6.3 Compact torus injection experiment

Compact torus (CT) is an advanced fuelling technology for tokamaks and other types of fusion devices. It was originally proposed by Perkins $et\ al.$ [52] and Parks [53]. Currently the STOR-M is the only tokamak equipped with a such device in the world.

The STOR-M tokamak is equipped with the University of Saskatchewan compact torus injector (USCTI) to inject compact torus (CT), a doughnut-shaped high density plasmoid. Previous CT injection experiments on the STOR-M tokamak shows it has a velocity of $\sim 150\mathrm{km/s}$ in the injector (Figure 6.5) when it was horizontally and tangentially injected [54]. Vertical CT injection was also achieved with the velocity of $\sim\ 130\ \mathrm{km/s}$, and when attaching a copper inner electrode to the USCTI, the velocity can be increased to 270 km/s [55].

Currently, the USCTI device is attached to the tokamak horizontally through a port at the mid-plane of the tokamak chamber, as shown in Figure 6.6. The CT is not perfectly aiming tangentially to the chamber. The angle between the CT and the normal of the chamber is $27°$, and the angle between CT injection direction and the tangential central line is $41°$. In the right top side of the

Figure 6.6, the magnetic signal of the CT is displayed. From the time-of-flight method, it can be seen the CT moves from z = 22 cm to z = 65 cm in less than 2.5 ms, which corresponds to an average velocity of 172 km/s.

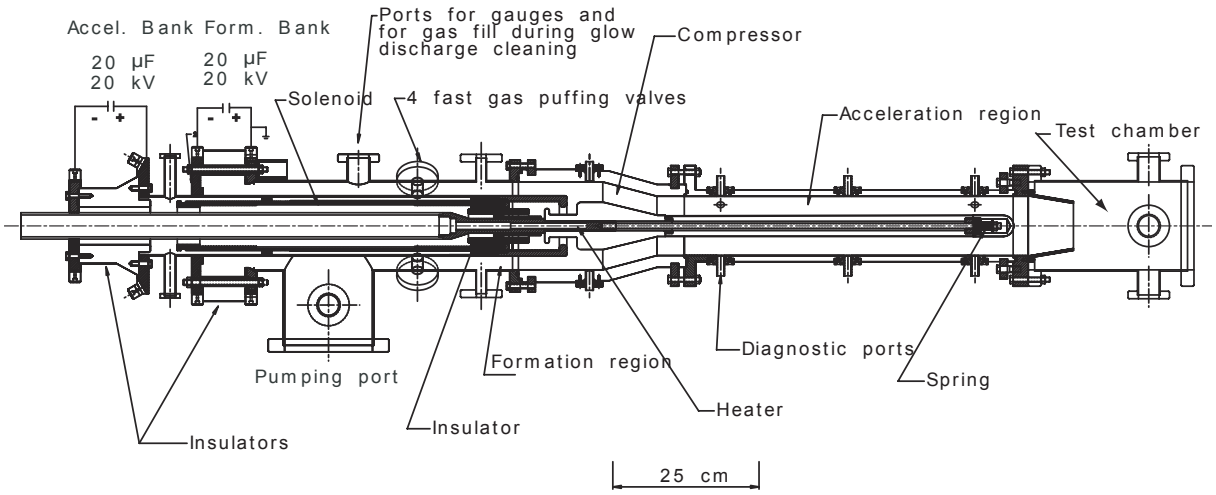

Figure 6.5: Schematic diagram of USCTI [55].

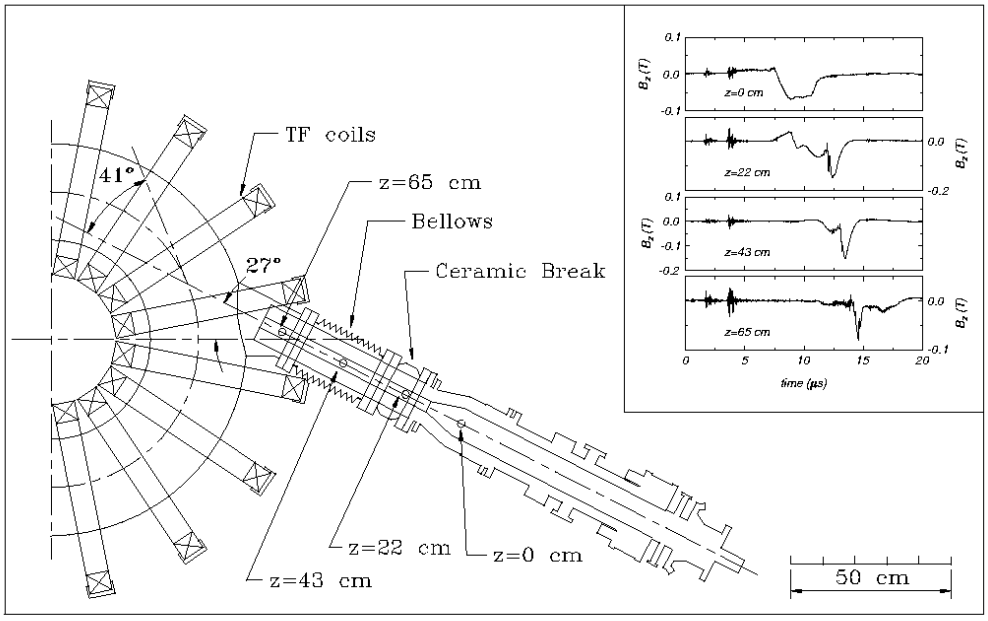

Figure 6.6: Diagram of the STOR-M tokamak and the USCTI injector for tangential CT injection experiments [18].

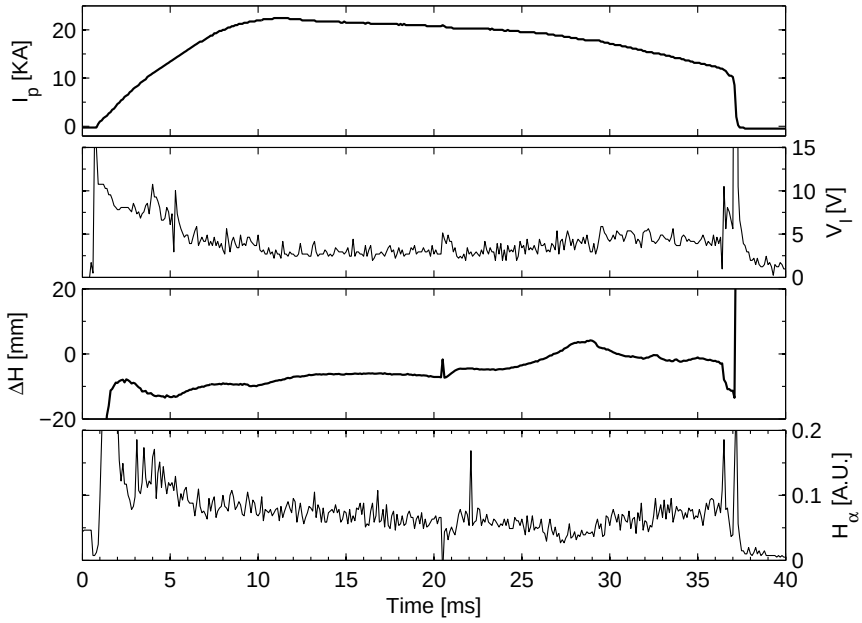

Figure 6.7: Plasma parameters of a typical shot #244715.

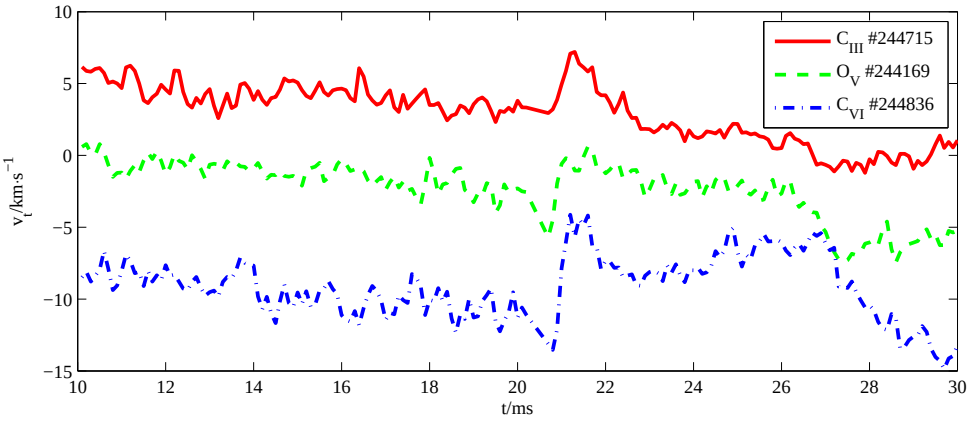

Figure 6.8: Toroidal flow velocity change induced by CT injection.

The effects of CT injection on impurity flows are displayed in Figure 6.8. The velocities measured for C_{III}, O_V and C_{VI} increase in less than one microsecond after CT formation and injection. The C_{III} increased its velocity of 5 km/s for 1ms, the O_V increased 6 km/s for 6 ms, and the C_{VI} increased about 10 km/s for the period of 8 ms. Thus the CT has larger effects on inner impurities than outer impurities.

The CT injects momentum to the tokamak plasma. For example, with a velocity of 150 km/s, considering CT has 50% of inventory of the tokamak plasma, the CT is able to induce a velocity

change of

$$150\ \mathrm{km/s} \times \cos 41^\circ \times \frac{50\%}{1+50\%} = 37\ \mathrm{km/s} \tag{6.1}$$

However, the experimentally measured velocity is much less than this value. A possible reason is that the energy of the CT particles is dissipated through collision with the chamber wall.

6.4 Resonant magnetic perturbation experiment

The toroidal plasma flow was also measured by the impurity lines during the resonant magnetic perturbation (RMP) experiment. RMP uses external magnetic field to suppress the magnetohydrodynamics (MHD) instability. Since MHD instability degrades plasma confinement, the RMP aims to improve the plasma conditions.

In the STOR-M tokamak, the RMP is induced by two sets of helical coils as shown in Figure 6.9. The coils are helically wound with poloidal and toroidal mode numbers m = 2, n = 1. The two sets of coils are connected in series. The RMP current pulse in the coils is generated by two capacitor banks: fast bank has 50 mF, 450 V; slow bank has 420 mF, 100 V. The current is gated by an IGBT rating at 1200 A and 1700 V.

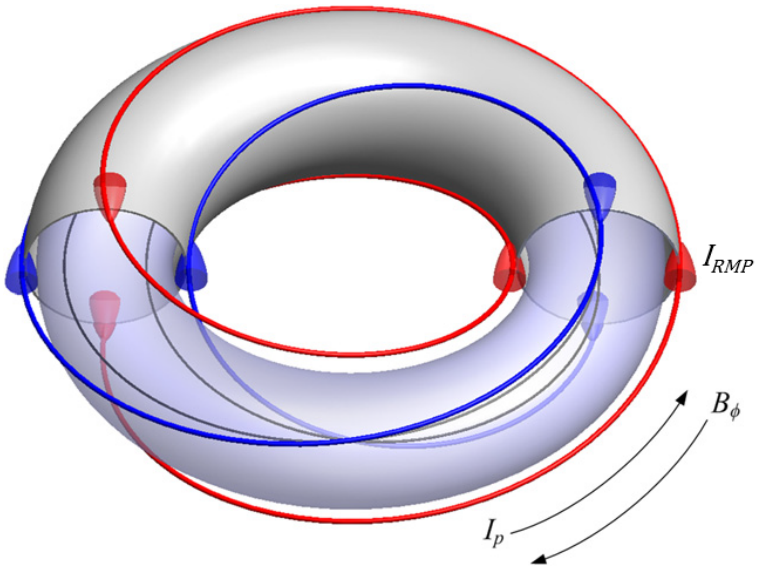

Figure 6.9: The coloured arrows indicate the direction of $\mathrm{I_{RMP}}$. The two sets of coils are connected in series and the RMP current is supplied by a capacitor bank discharge [56].

The major effect of RMP field is the suppression of MHD fluctuation, as measured by Mirnov

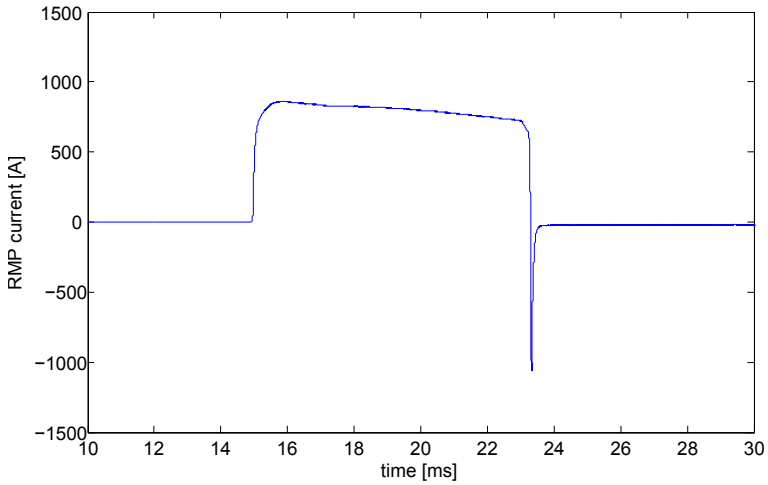

Figure 6.10: Waveform of single RMP pulse.

coils. Improved plasma confinement was also observed as reduction in H_α, reduction in loop voltage, and increase in the soft x-ray.

The $\mathrm{O_V}$ and $\mathrm{C_{VI}}$ flows are measured during different RMP currents and different plasma current. Higher RMP current can induce larger change on the $\mathrm{O_V}$ and $\mathrm{C_{VI}}$ flow velocities, as well as higher plasma current do. The results of flow measurement was shown in Figure 6.11 and Figure 6.13. The flow velocity result was smoothed for 1ms for easier comparison.

In Figure 6.11, a single RMP current pulse is used. It can been that the $\mathrm{O_V}$ velocity has increased $6 \sim 8\ \mathrm{km/s}$ towards to the counter-clockwise direction, and the $\mathrm{C_{VI}}$ velocity has increased $8 \sim 10\ \mathrm{km/s}$ towards to the counter-clockwise direction. The flow was measured in different plasma current and different RMP current. It can been seen that the higher RMP current can induce larger change on the flow, and the RMP has larger flow change effect on higher plasma current discharges. In Figure 6.13, double RMP current pulses are used. The same effect on plasma flow change was observed. The plasma flow was changed towards to the counter-clockwise direction twice, and it recovers when the RMP current pulse was terminated.

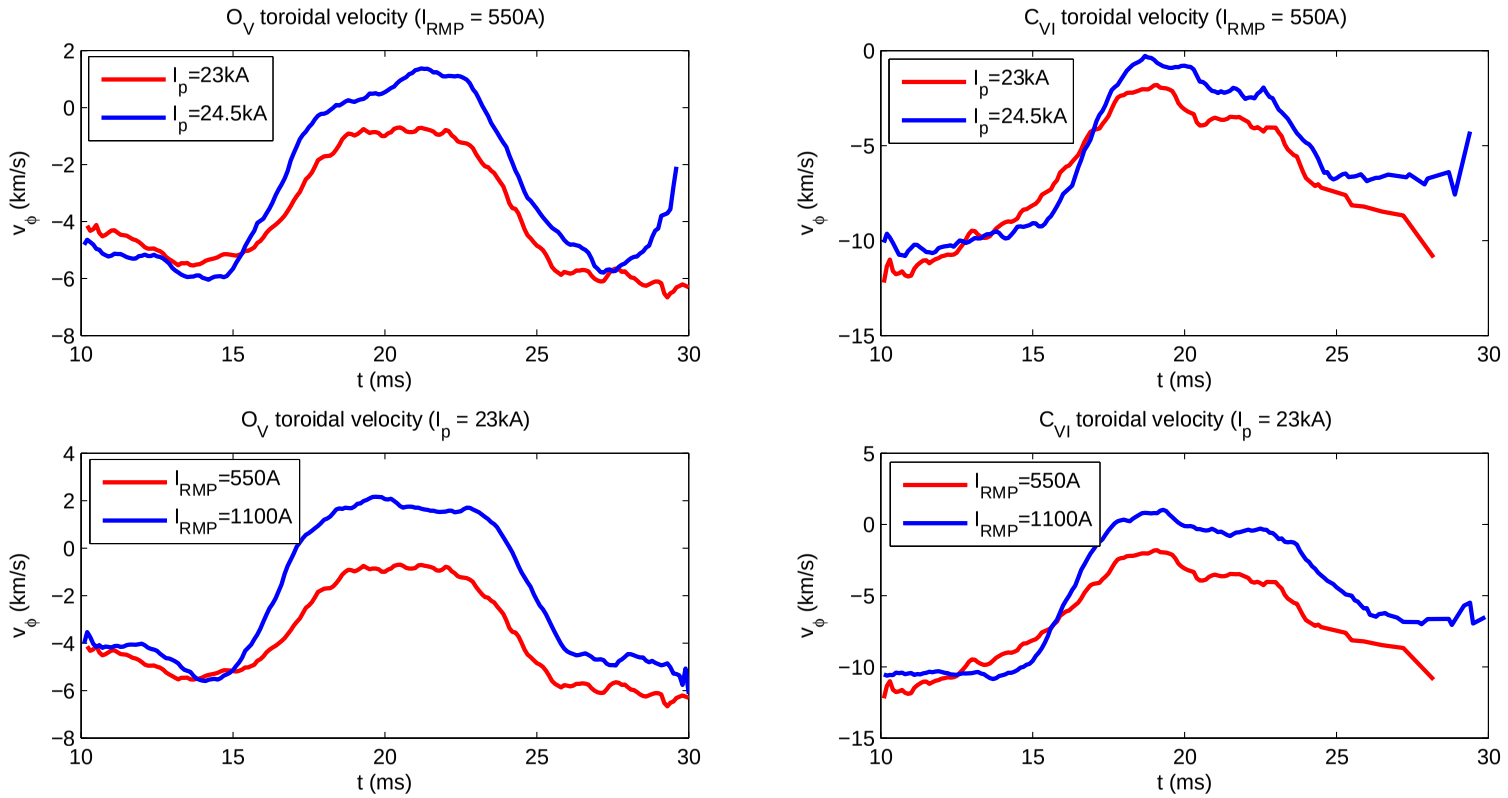

Figure 6.11: O_V and C_{VI} flow velocities measured during RMP experiment. Two sets of RMP current and two sets of plasma current are used.

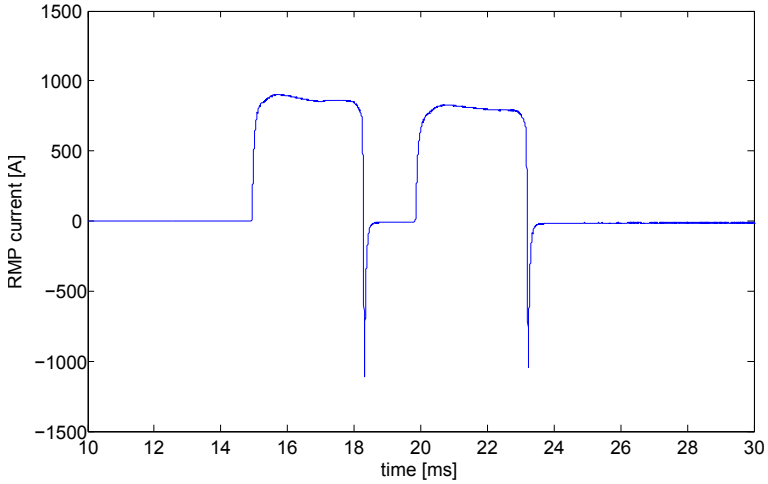

Figure 6.12: Waveform of double RMP pulses.

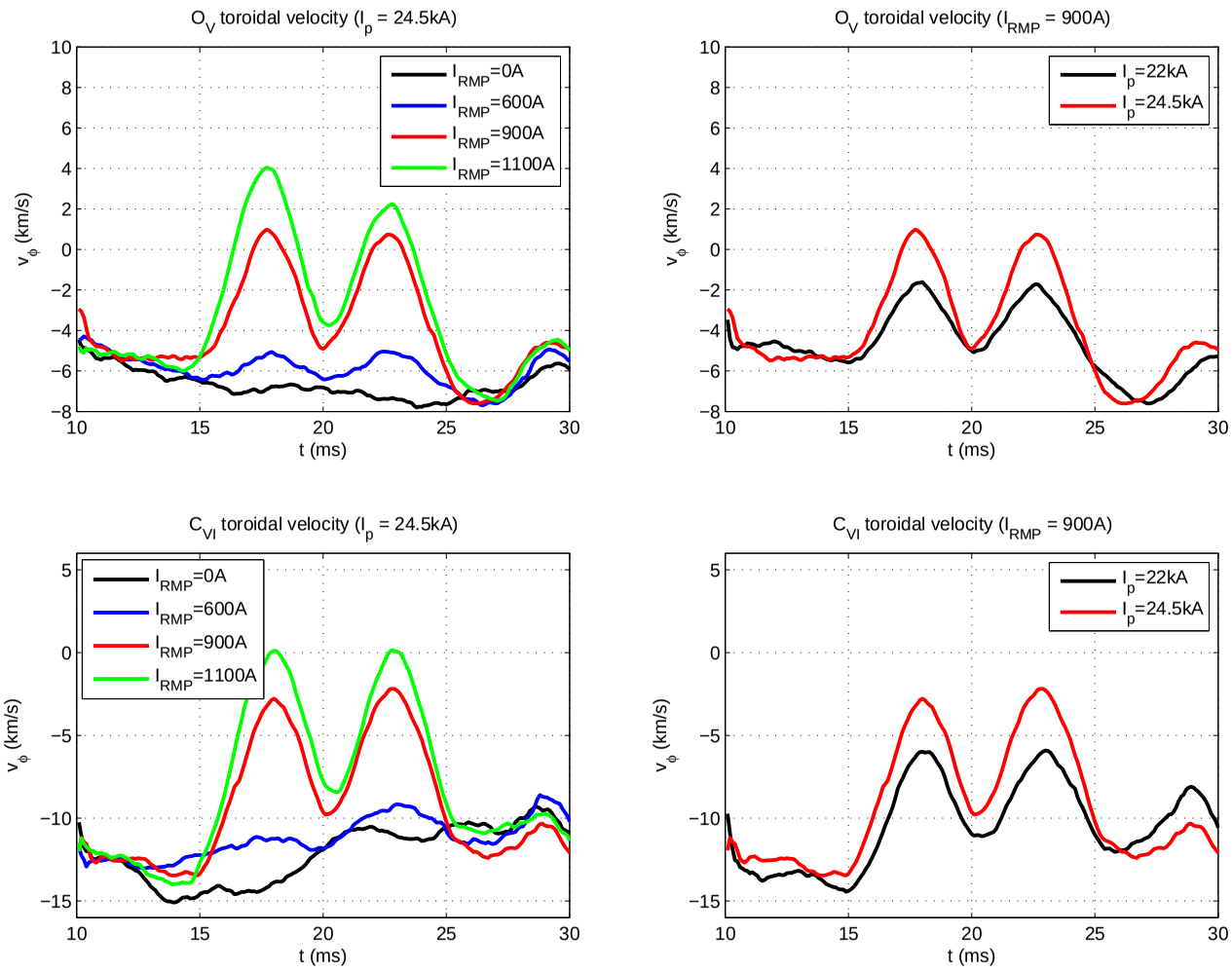

Figure 6.13: O_V and C_{VI} flow velocities measured with double RMP current pulses. Two sets of plasma current were also used.

6.5 Ohmic H-mode like transition experiment

Plasma condition can be influenced by additional gas puffing. In the STOR-M tokamak, Ohmic H-mode like transition was induced by rapid gas puffing (GP) pulses, and GP was achieved by using three Veeco RG-83 gauges controlled by the common controlling signal. The GP control pulse signal is shown in Figure 6.14, the first pulse is exerted from 5 to 10 ms, and the second is exerted from 17 to 20 ms. The pressure was increased to 1.3×10^{-4} Torr from 1.1×10^{-4} Torr.

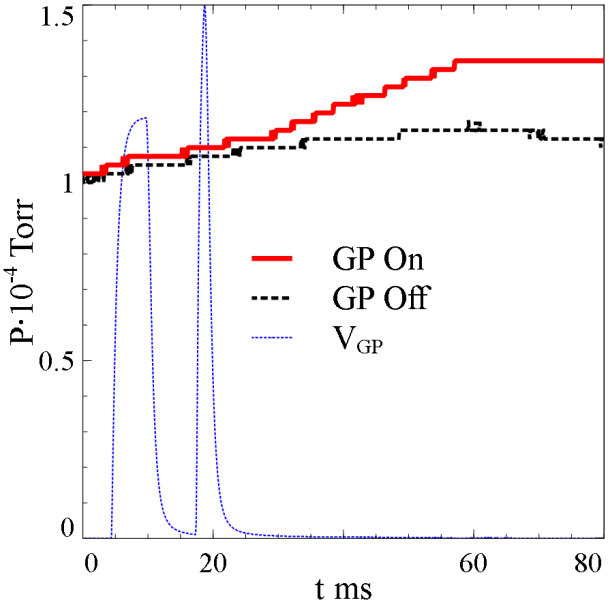

Figure 6.14: Waveforms of GP control pulse and pressure in the tokamak chamber.

The toroidal flow velocities of impurity lines C_{III}, O_V, and C_{VI} are shown in Figure 6.16. The impurity flows are affected by the GP in two stages. The first stage is from 20 to 22 ms, when the flow increased toward to the counter-clockwise direction about 5 km/s for C_{VI}, and smaller amount for other impurities. The second stage is from 22 to 30 ms. During this period, the C_{VI} flow increased in clockwise direction by 10 km/s and other impurities increased smaller amount. It shows that the GP is more effective on changing the flow of central impurities.

The toroidal flow velocity was also measured by the G-probe during the gas puffing Ohmic H-like experiment shown in Figure 6.17, in comparison with the C_{III} flow velocity. It shows both of they decrease to negative after the transition. But with an assumption of $T_e = T_i = 20\text{eV}$ in the SOL region [57, 58], the toroidal plasma rotation measured by G-probe in the SOL region is 25 km/s, which is 5 times larger than the C_{III} flow velocity. There are a few reasons for the

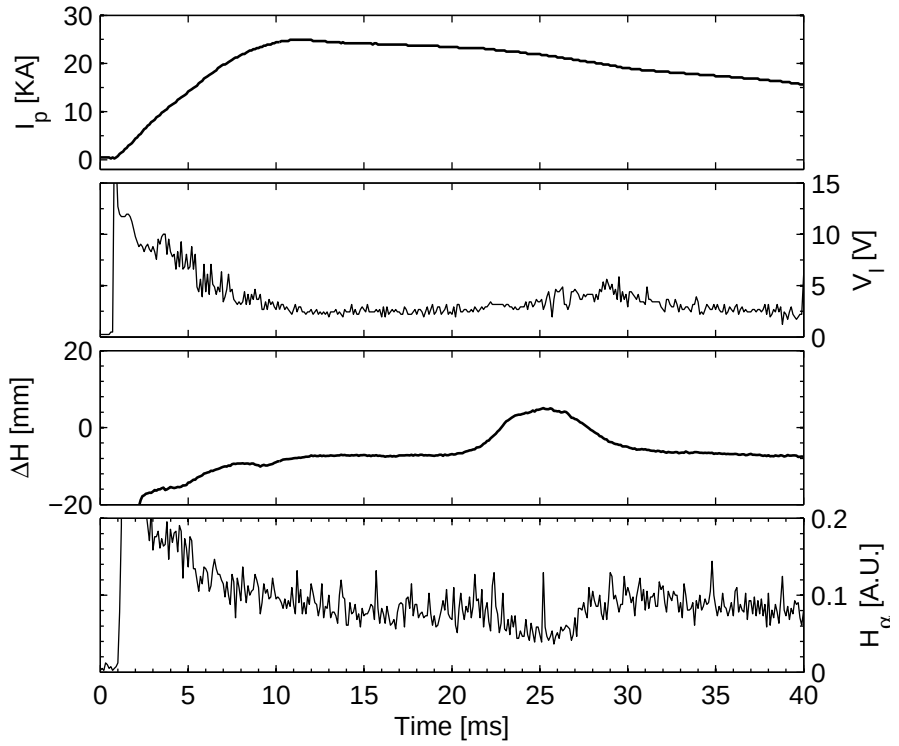

Figure 6.15: Plasma parameters of a typical shot #241271.

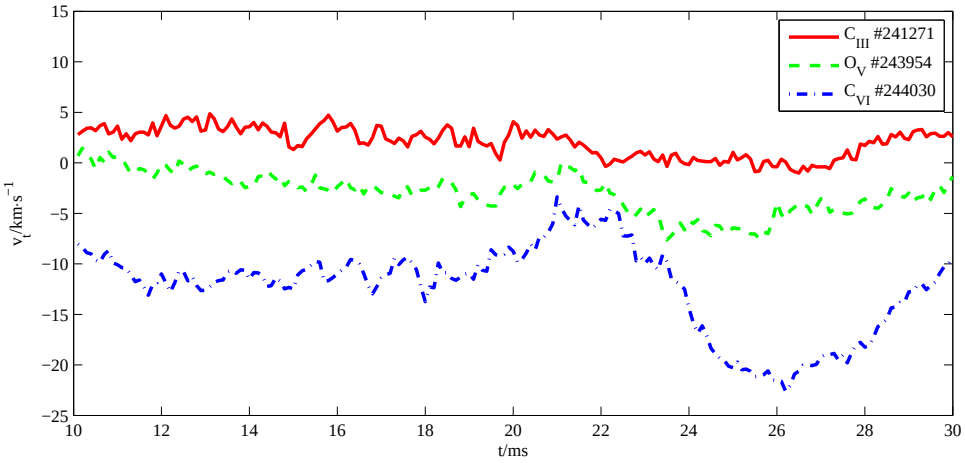

Figure 6.16: Impurity flow measured during the gas puffing induced transition experiment.

difference on the velocity measurement: the G-probe and the C_{III} impurity line are measuring the ion velocities at different location; also the G-probe measures the velocities of the major ion - hydrogen, while the C_{III} may have different velocity than the hydrogen ion.

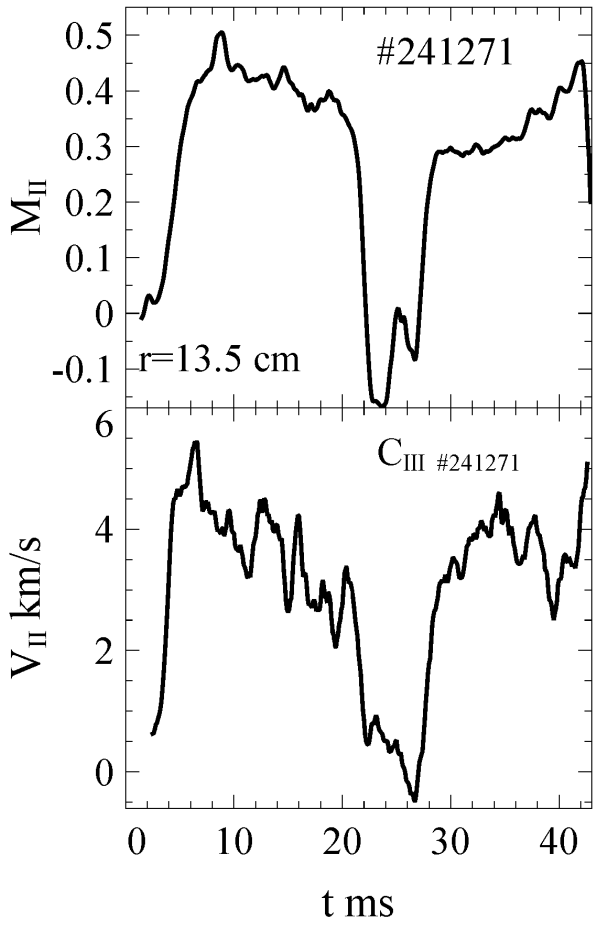

Figure 6.17: Toroidal flow velocity measured by G-probe during Ohmic H-mode like transition experiment.

Chapter 7

Conclusions and future work

7.1 Conclusions

The IDS system built for the STOR-M tokamak is based on a Czerny-Turner spectrometer and uses a multi-channel PMT array as the detector, which records the spectrum magnified by a cylindrical rod lens. Carbon and oxygen emission lines $\mathrm{C_{III}}$, $\mathrm{O_V}$ and $\mathrm{C_{VI}}$ are used for toroidal velocity measurement. It achieved a time resolution of 0.1 ms and velocity resolution of $1 \sim 2\,\mathrm{km/s}$.

Various impurity emission lines have been identified in the STOR-M tokamak. $\mathrm{C_{III}}$, $\mathrm{O_V}$ and $\mathrm{C_{VI}}$ are selected for flow measurement because of the difference on their ionization states. Radial profile measurement of emissivity shows lower ionization state ions are populated at the periphery of the plasma, while the higher ones are concentrated in deeper regions.

The toroidal flow velocities of the impurity ions are measured on a shot-by-shot basis. The wavelength measured through the normal port is used for reference, while the tangential wavelength corresponding to the toroidal flow velocity. It shows that the ions in the plasma edge region flow in the co-current direction, while the ions in the core regions flow in the opposite way (anti-current). The reversal of plasma current direction causes the reversal of impurity flow directions, which is predicted in theory.

The impurity flow was also measured in different operation modes. It is confirmed that compact torus (CT) can inject momentum to the tokamak plasma, and the central ion flow is more affected. Resonant Magnetic Perturbation (RMP) changes the plasma flow in the same direction as CT. It also shows higher RMP current can induces larger change on the plasma flow, and it is more effective

on discharges with higher plasma current. Rapid gas puffing is able to change the impurity flow as well. However, the mechanism of RMP and rapid gas puffing on flow change is not clear yet.

7.2 Future work

7.2.1 Ion temperature measurement

The impurity ion temperature can be measured by the same IDS system. The Doppler broadening due to ion temperature is expressed in Equation (3.24). In the tokamak, it is crucial to determine the effects of other broadening mechanisms. The instrumental broadening can be quantitatively measured by calibration lamp. The effects of other broadening mechanisms such as Zeeman splitting and Stark effect can be theoretically calculated.

7.2.2 Simultaneous measurement of the normal and tangential ports in the tokamak.

In the present system, emissions through the normal and tangential ports are measured separately. It requires additional time for normal port measurement. By using two optical fibers collecting the light from two sources, the reference and shifted wavelengths can be measured simultaneously. At the spectrometer side, the two fiber ends can set vertically with one on top of another. Correspondingly, the image of the two fiber ends would appear at the exit of the spectrometer with one on top of another. Two identical PMT arrays can be used to record these spacially separated spectra. Thus, the two spectra can be measured simultaneously. Similar design has been reported in the literature [48].

7.2.3 Relationship between the impurity ion flow velocity and bulk plasma flow velocity

In the present measurement, only the flow of impurity species are measured. However, the major species (hydrogen) flow velocity may be different from the impurity flow velocities. The main-impurity ions energy exchange time and the impurity ion life time can be calculated and compared.

If the energy exchange time is short enough, the impurities have the same flow velocity and temperature as the main ion.

Bibliography

[1] E. I. Moses, *Nucl. Fusion*, **49**, 104022, (2009).

[2] K. Ikeda, *Nucl. Fusion*, **50**, 014002, (2010).

[3] International Fusion Research Council (IFRC), *Nucl. Fusion*, **45**, A1 (2005).

[4] F. F. Chen, *Plasma Physics and Controlled Fusion - Volume 1: Plasma physics, 2nd ed.*, Springer, New York, (2004).

[5] J. Wesson, *Tokamaks,* 3^{rd} *ed.*, Oxford Science Publications, Oxford, (2004).

[6] T. Fujita, T. Hatae, T. Oikawa, S. Takeji, H. Shirai, Y. Koide, S. Ishida, S. Ide, Y. Ishii, T. Ozeki, S. Higashijima, R. Yoshino, Y. Kamada, and Y. Neyatani, *Nucl. Fusion*, **38**, 207, (1998).

[7] A. M. Garofalo, E. J. Strait, L. C. Johnson, R. J. La Haye, E. A. Lazarus, G. A. Navratil, M. Okabayashi, J. T. Scoville, T. S. Taylor, and A. D. Turnbull, Phys. Rev. Lett. **89**, 235001 (2002).

[8] M Okabayashi, J Bialek, M S Chance, M S Chu, E D Fredrickson, A M Garofalo, R Hatcher, T H Jensen, L C Johnson, R J La Haye, G A Navratil, H Reimerdes, J T Scoville, E J Strait, A D Turnbull, M L Walker and the DIIID Team, Plasma Phys. Control. Fusion **44** B339 (2002).

[9] A. Eden, *The search for Christian Doppler*, Springer-Verlag, Wien, (1992).

[10] J. H. F. Severo, I. C. Nascimento, Yu. K. Kuznetsov, V. S. Tsypin, R. M. O. Galvão, and M. Tendler, *Rev. Sci. Instrum.*, **78**, 043509 (2007).

[11] J. H. F. Severo, I. C. Nascimento, Yu. K. Kuznetsov, R. M. O. Galvão, Z. O. Guimarães-Filho, F. O. Borges, O. C. Usuriaga, J. I. Elizondo, W. P. de Sá, E. K. Sanada, and M. Tendler, *Nucl. Fusion*, **49** 115026 (2009).

[12] C. D. Cothran, J. Fung, M. R. Brown, and M. J. Schaffer, *Rev. Sci. Instrum.*, **77**, 063504 (2006).

[13] W. S. Harris III, *Ion Flow Measurements and Plasma Current Analysis in the Irvine Field Reversed Configuration*, Ph.D. thesis, University of California, University of California, Irvine, (2009).

[14] P. Gu, M. Nagata, K. J. McCollam, T. R. Jarboe, Brian A. Nelson, and A. J. Redd, *Rev. Sci. Inst.*, **75**, 5, (2004).

[15] J. D. King, H. S. McLean, R. D. Wood, C. A. Romero-Talamás, J. M. Moller, and E. C. Morse, *Rev. Sci. Instrum.*, **79**, 10F535, (2008).

[16] E. Gazza and M. Valisa, *Rev. Sci. Instrum.*, **80**, 033501 (2009).

[17] *Precision Leak Valve PV-10 Operation and Maintenance*, Veeco Instruments Inc., 287.

[18] A. Hirose, C. Xiao, O. Mitarai, J. Morelli, and H. M. Skarsgard, *Physics in Canada*, Hiro1, March/April (2006).

[19] M. Enaami-Khonsaari, *Modelling and Control of Plasma Position in the STOR-M tokamak*, Ph.D. Thesis, University of Saskatchewan, (1990).

[20] J. E. Morelli, *Plasma Position Control in The STOR-M tokamak: A Fuzzy Logic Approach*, Ph.D. Thesis, University of Saskatchewan, Saskatoon, (2003).

[21] HEATH Company, *The HEATH Scanning Monochromator EU-700 Series User Manual*.

[22] Ocean Optics Inc., *USB2000 Fiber Optic Spectrometer Installation and Operation Manual*.

[23] SPEX 1702/1704 instructions.

[24] I. H. Hutchinson, *Phys. Fluids*, **30**, 3777 (1987).

[25] I. H. Hutchinson, *Phys. Rev. A.*, **37**, 4358 (1988).

[26] C. Xiao, K. K. Jain, W. Zhang, and A. Hirose, *Phys. Plasmas*, **1** (7), July (1994).

[27] G. M. R. St. Germaine, *Plasma Flow Velocity Measurements with a Gundestrup Probe in the STOR-M Tokamak*, M.Sc. Thesis, University of Saskatchewan, (2006).

[28] I. H. Hutchinson, *Principles of Plasma Diagnositics, 2nd Ed.*, Cambridge University Press, Cambridge, (2002).

[29] P. G. Carolan and V. A. Piotrowicz, *Plasma Physics*, **10**, 1065-1086, (1983).

[30] S. Suckewer, H. P. Eubank, R. J. Goldston, E. Hinnov, and N. R. Sauthoff, *Phys. Rev. Lett.*, **43**, 3, (1979).

[31] D. Craig, D. J. Den Hartog, D. A. Ennis, S. Gangadhara, and D. Holly, *Rev. Sci. Instrum.*, **78**, 013103, (2007).

[32] M. De Bock, *Understanding and controlling plasma rotation in tokamaks*, Ph.D. Thesis, Technische Universiteit Eindhoven, Belgie, (2007).

[33] C. Palmer and E. Loewen, *Diffraction Grating Handbook, 6th Ed.*, Newport Corporation, New York (2005).

[34] S.J. Frank L. Pedrotti, Leno S. Pedrotti, and Leno M. Pedrotti, *Introduction to optics, 3rd ed.*, Pearson Education, INC., (2007).

[35] Hamamatsu Photonics Inc., *Linear Array Multi Anode PMT and Assembly R5900U-L16 Series, H7260 Series*, Instruction Manual.

[36] P. R. Bevington, and D. K. Robinson, *Data Reduction and Error Analysis for the Physical Sciences, 3rd ed.*, McGraw Hill, New York, (2003).

[37] D. Rapisarda, B. Zurro, A. Baciero, and V. Tribaldos, *Rev. Sci. Instrum.*, **77**, 033506, (2006).

[38] W. Zhang, *Improved Ohmic Confinement Induced by Turbulent Heating and Electrode Biasing in the STOR-M Tokamak*, Ph.D. Thesis, University of Saskatchewan, (1993).

[39] Y. Hasebe, M. Okamoto, S. Kajita, N. Ohno, and S. Takamura, *Plasma and Fusion Research: Regular Articles*, **3**, S1015, (2008).

[40] R. P. Golingo and U. Shumlak, *Rev. Sci. Instrum.*, **74**, 4, (2003).

[41] D. J. Den Hartog and R. J. Fonck, *Rev. Sci. Instrum.*, **65**, 10, (1994).

[42] J. Gafert, K. Behringer, D. Coster, C. Dorn, K. Hirsch, M. Niethammer, U. Schumacher, and the ASDEX Upgrade Team *Plasma Phys. Control. Fusion*, **39**, 1981-1995, (1997).

[43] T. Asai, T. Matsuzawa, N. Yamamoto, K. Sakuraba, T. Kiguchi, K. Kishi, T. Takahashi, S. Hiromori, T. Ikeyama, Y. Nogi, and T. Takahashi, *Proceedings of ITC/ISHW 2007*.

[44] G. R. McKee, D. J. Schlossberg, and M. W. Shafer, *Rev. Sci. Inst.*, **79**, 10F528, (2008).

[45] J. Sallander, *Time- and space-resolved spectroscopy at the EXTRAP-T2 reversed-field pinch*, Ph.D. thesis, Royal Institute of Technology, Stockholm, (1998).

[46] D. Gupta, N. Bolte, H. Gota, R. Hayashi, V. Kiyashko, P. Marsili, M. Morehouse, S. Primavera, T. Roche, and F. Wessel *Rev. Sci. Instrum.*, **81**, 10D730, (2010).

[47] A. T. Graf, *Doppler Measuremens in the Edge of the Alcator C-Mod Tokamak using a High-Resolution Visible Spectrometer*, Ph.D. Thesis, University of Canifornia, Davis, (2008).

[48] H. Sakakita, S. Kiyama, Y. Hirano, Y. Yagi, H. Koguchi, S. Sekine, T. Shimada, I. Hirota, and Y. Maejima, *Rev. Sci. Instrum.*, **74**, 3 (2003).

[49] S. Banerjee, V. Kumar, M.B. Chowdhuri, J. Ghosh, R. Manchanda, K.M. Patel and P. Vasu, *Meas. Sci. Technol.*, **19**, 045603, (2008).

[50] NIST Atomic Spectra Database: http://www.nist.gov/pml/data/asd.cfm.

[51] V. I. Bugaraya et al., *Nucl. Fussion*, **25**, 1707 (1985).

[52] L. J. Perkins, J. H. Ho, and J. H. Hammer, *Nucl. Fusion*, **28**, 1365 (1988).

[53] P. B. Parks, *Phys. Rev. Lett.*, **61**, 1364 (1988).

[54] C. Xiao, A. Hirose, and S. Sen, *Phys. Plasmas*, **11**, 8 (2004).

[55] D. Liu, *Vertical Compact Torus Injection into the STOR-M Tokamak*, Ph.D. Thesis, University of Saskatchewan, (2006).

[56] S. Elgriw, D. Liu, T. Asai, A. Hirose and C. Xiao, *Nucl. Fussion*, **51**, 113008 (2011).

[57] W. Zhang, C. Xiao and A. Hirose, *Phys. Fluids B*, **5**, 3961-8 (1993).

[58] M. Dreval, D. Rohraff, C. Xiao and A. Hirose, *Rev. Sci. Instrum.*, **80**, 103505 (2009).

Appendix A - optical components

In this section, the design of optical components of the modified exit optics is presented. Various stations are used for translation and rotation movement of the cylindrical rod lens, which is a crucial part of the precise adjustment.

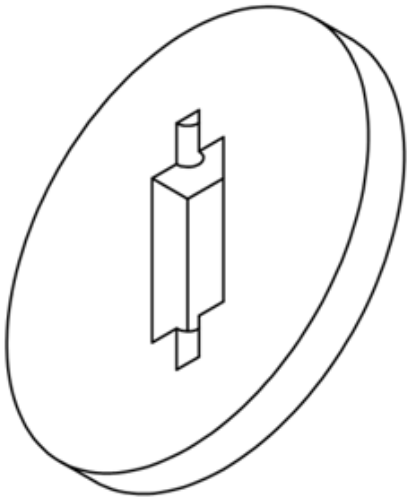

Figure 7.1: The drawing of the lens holder.

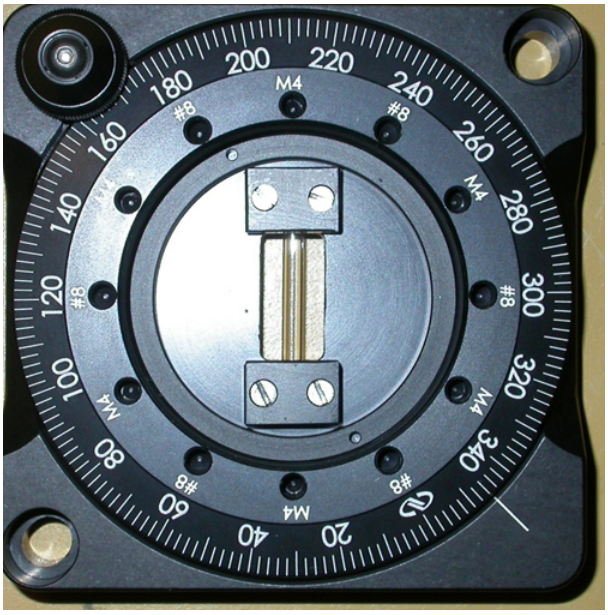

Figure 7.2: The picture of the rotational stage (Newport RSP-2T).

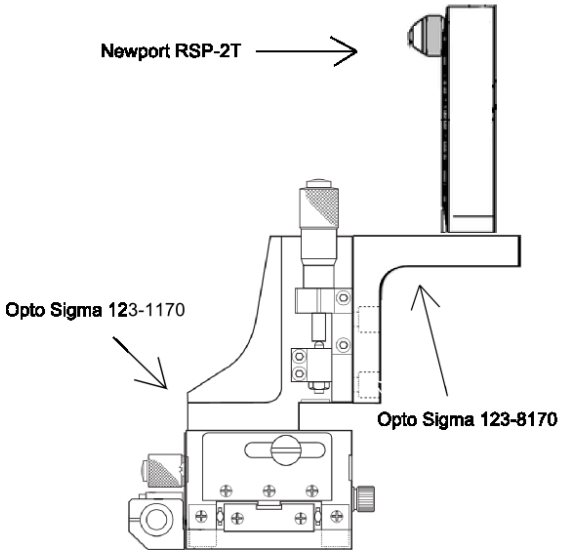

Figure 7.3: The side view of the optical components of the lens stage combination.

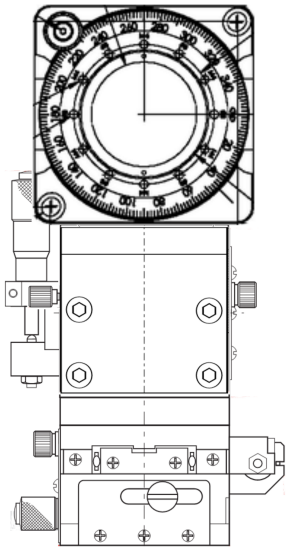

Figure 7.4: The front view of the optical components of the lens stage combination.

Appendix B - Linear dispersion measurement.

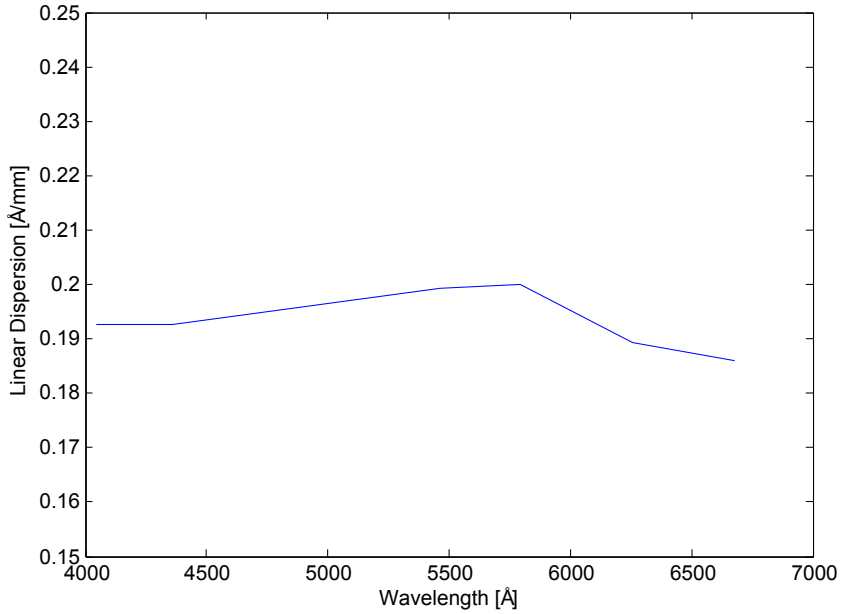

Figure 7.5: Linear dispersion measurement with various wavelength.

Appendix C - Nonlinear Gaussian fitting code

The nonlinear Gaussian fitting routine programmed in MS Visual C++ is presented here.

```
1
2  # include <iostream>
3  # include <fstream>
4  # include <math.h>
5  # include <time.h>
6
7  using namespace std;
8
9  # define n 16 // number of channels
10 # define m 600
11
12 double chisq(double a, double b, double c2, double d2, double d[n], double e[n]);
13
14 void main()
15 {
16     double x[n], y[n], a[4], parchisq[4], gammar[4], Data[m][n], Data2[m/10][n];
17     double time1, time2, R1, R2, Delta, D0, tol, sumxy, sumy, sumyxb, parchisqsum, chisq1, chisq2, FWHM, R
       , y_ave, y_sum, SStot, k2, k3, k_d, k_u, lambda;
18     int i, j, k, l, h, ten_ave, normal;
19     char N_shot[7];
20     char filename1[15]="133C000000.txt";
21     char filename2[15]="Para000000.txt";
22     char filename3[15]="Flow000000.txt";
23
24     D0 = 1e-2; // the iteration step to find the minimum square sum
25     tol = 1e-6;
26
27     ten_ave = 0;
28
29     ifstream ifile1;
30     ifstream ifile2;
31     ofstream ofile1;
32     ofstream ofile2;
33
34     ifile2.open("Data.txt");
35
36 for (h=1; h<=80; h++)
37 {
38
39     ifile2>>N_shot>>lambda>>normal>>k_d>>k_u;
40
41     for(i=0;i<6;i++)
42     {
43         filename1[i+4]=N_shot[i];
44         filename2[i+4]=N_shot[i];
45         filename3[i+4]=N_shot[i];
46     }
47
48
49     ifile1.open(filename1);
50     ofile1.open(filename2);
51     ofile2.open(filename3);
52
53
54     l = 0;
55
56     for (j=0;j<m;j++)
57     {
58         for (i=0; i<n; i++)
59         {
60             ifile1 >> Data[j][i];
61         }
62     }
63
```

```
64      for(i=0; i<m/10; i++)
65      {
66          for (j=0; j<n; j++)
67          {
68              Data2[i][j] = 0;
69
70              for (k=0; k<10; k++)
71              {
72                  Data2[i][j] += Data[i*10+k][j];
73              }
74
75              Data2[i][j] = Data2[i][j]/10;
76
77          }
78      }
79
80      for(i=0;i<n;i++)
81      {
82          x[i] = i+1;
83      }
84
85      cout<<"Calculating #"<<N_shot<<"..."<<endl<<endl;
86
87  for (k=k_d;k<k_u;k++)
88  {
89
90  // Clear old Data
91          Delta = 0;
92          sumxy = 0;
93          sumy = 0;
94          sumyxb = 0;
95          parchisqsum = 0;
96          chisq1 = 0;
97          chisq2 = 0;
98          FWHM = 0;
99          R = 0;
100         y_ave = 0;
101         y_sum = 0;
102         SStot = 0;
103         R1 = 0.0;
104         R2 = 1.0;
105
106
107     for (i=0; i<n; i++)
108     {
109         if(ten_ave)
110             y[i] = Data2[k][i];
111         else
112             y[i] = Data[k][i];
113     }
114
115 // Curve fitting
116
117     for (i=0;i<n;i++)
118     {
119         y_sum += y[i];
120     }
121
122     y_ave = y_sum/n;
123
124     for (i=0; i<n; i++)
125     {
126         SStot += pow((y[i]-y_ave),2);
127     }
```

```
128
129     // Find the initial values of a[3].
130
131
132     a[3] = (y[0]+y[1]+y[14]+y[15])/4.0;
133
134     a[0] = y[0]-a[3];
135
136     a[1] = x[0];
137
138     for (i=0;i<n;i++)
139     {
140         if ((y[i]-a[3])>a[0])
141         {
142             a[0] = (y[i]-a[3]);
143             a[1] = x[i];
144         }
145     }
146
147     for (i=0;i<n;i++)
148     {
149         sumxy += x[i]*(y[i]-a[3]);
150         sumy += (y[i]-a[3]);
151     }
152
153
154     for (i=0; i<n; i++)
155     {
156         sumyxb += (y[i]-a[3]) * pow((x[i]-a[1]), 2);
157     }
158
159     a[2] = sqrt(abs(sumyxb/sumy));
160
161     if (a[2]>3.4)
162         a[2] = 3.4;
163
164 //  cout<<a[0]<<"   "<<a[1]<<"    "<<a[2]<<"    "<<a[3]<<endl;
165
166
167     chisq2 = chisq(a[0], a[1], a[2], a[3], x, y);
168     chisq1 = 100;
169
170     // Start iteration for finding the best fit curve.
171     Delta = D0;
172     j = 0;
173
174     time1 = clock();
175
176     while ((fabs(R1-R2)>tol)||(R<0.95))
177     {
178
179     parchisq[0] = (chisq(a[0]+Delta, a[1], a[2], a[3], x, y) - chisq(a[0], a[1], a[2], a[3], x, y))/Delta;
180     parchisq[1] = (chisq(a[0], a[1]+Delta, a[2], a[3], x, y) - chisq(a[0], a[1], a[2], a[3], x, y))/Delta;
181     parchisq[2] = (chisq(a[0], a[1], a[2]+Delta, a[3], x, y) - chisq(a[0], a[1], a[2], a[3], x, y))/Delta;
182     parchisq[3] = (chisq(a[0], a[1], a[2], a[3]+Delta, x, y) - chisq(a[0], a[1], a[2], a[3], x, y))/Delta;
183     parchisqsum = sqrt(pow(parchisq[0],2) + pow(parchisq[1],2) + pow(parchisq[2],2) + pow(parchisq[3],2));
184
185     time2 = clock() - time1;
186
187     if((j<1)&&(time2>50))
188     {
189         Delta *= 0.1;
190         j++;
191     }
```

```
192
193
194     if((j<2)&&(time2>130))
195     {
196         Delta *= 0.1;
197         j++;
198     }
199
200
201     if((j<3)&&(time2>340))
202     {
203         Delta *= 0.1;
204         j++;
205     }
206
207     if((j<4)&&(time2>914))
208     {
209         Delta *= 0.1;
210         j++;
211     }
212
213     if((j<5)&&(time2>2000))
214     {
215         Delta *= 0.1;
216         j++;
217     }
218
219
220     for (i=0;i<4;i++)
221         {
222             gammar[i] = parchisq[i]/parchisqsum;
223             a[i] += -gammar[i]*Delta;
224         }
225
226     chisq1 = chisq2;
227     chisq2 = chisq(a[0], a[1], a[2], a[3], x, y);
228
229     FWHM = 2*sqrt(2*log(2.0))*a[2];
230
231     R = 1 - (chisq2)/(SStot);
232
233     R1 = R2;
234     R2 = R;
235
236     if (time2>5000) // the calculation of each fitting should be done within 5 seconds.
237     {
238         break;
239     }
240
241
242 //  cout<<endl<<R<<endl;
243
244     }
245
246     k2 = double(k+1)/10.0;
247
248     if(ten_ave)
249     {
250         k2 = double(k+1);
251     }
252
253     k3 = a[1]*0.196/lambda*3e5;
254
255     if(R>0.9)
```

```
256     {
257
258     ofile1<<(k+1)<<"    "<<R<<"    "<<a[1]<<"    "<<FWHM<<"    "<<a[0]<<"    "<<a[1]<<"    "<<a[2]<<"    "<<a[3]<<"    "<<time2<<endl;
259
260 //  cout<<(k+1)<<"    "<<R<<"    "<<a[0]<<"    "<<a[1]<<"    "<<a[2]<<"    "<<a[3]<<"    "<<time2<<endl;
261
262     ofile2<<(k2-17.0)<<"    "<<k3<<endl;
263
264     }
265
266     }
267
268     cout<<"Calculation Completed!  Time eclapsed= "<<(clock()/1000)<<" Seconds"<<endl<<endl;
269
270     ifile1.close();
271     ofile1.close();
272     ofile2.close();
273
274 }
275
276     ifile2.close();
277
278 }
279
280 double chisq (double a, double b, double c2, double d2, double d[n], double e[n])
281 {
282     double f, F[n];
283     f = 0;
284
285         for (int i=0; i<n; i++)
286     {
287         F[i] = a*exp(-pow((d[i]-b),2)/(2*pow(c2,2))) + d2;
288         f += pow((F[i]-e[i]),2);
289     }
290         return f;
291 }
```